

Measurements of the Radiation Hardness of CsI(Tl) Scintillation Crystals and
Comparison Studies with Pure CsI for the Belle II Electromagnetic Calorimeter

by

Savino Longo

B.Eng., McMaster University, 2013

A Thesis Submitted in Partial Fulfillment of the
Requirements for the Degree of

MASTER OF SCIENCE

in the Department of Physics and Astronomy

© Savino Longo, 2015
University of Victoria

All rights reserved. This thesis may not be reproduced in whole or in part, by
photocopying or other means, without the permission of the author.

Measurements of the Radiation Hardness of CsI(Tl) Scintillation Crystals and
Comparison Studies with Pure CsI for the Belle II Electromagnetic Calorimeter

by

Savino Longo

B.Eng., McMaster University, 2013

Supervisory Committee

Dr. John Michael Roney, Supervisor

(Department of Physics and Astronomy, University of Victoria)

Dr. Robert Kowalewski, Departmental Member

(Department of Physics and Astronomy, University of Victoria)

Supervisory Committee

Dr. John Michael Roney, Supervisor
(Department of Physics and Astronomy, University of Victoria)

Dr. Robert Kowalewski, Departmental Member
(Department of Physics and Astronomy, University of Victoria)

ABSTRACT

In preparation for the large backgrounds expected to be present in the Belle II detector from the SuperKEKB e^+e^- collider, the radiation hardness of several large ($5 \times 5 \times 30 \text{ cm}^3$) thallium doped cesium iodide (CsI(Tl)) scintillation crystals are studied. The crystal samples studied consist of 2 spare crystals from the Belle experiment using PIN diode readout and 7 spare crystals from the *BABAR* experiment using photomultiplier tube readout. The radiation hardness of the scintillation properties of the CsI(Tl) crystals was studied at accumulated $\sim 1 \text{ MeV}$ photon doses of 2, 10 and 35 Gy. At each dose, the longitudinal uniformity of the crystals light yield, scintillation decay times, time resolution and energy resolution was measured. As the Belle II collaboration is considering an upgrade to pure CsI crystals if CsI(Tl) does not satisfy radiation hardness requirements, the scintillation properties of a pure CsI scintillation crystal were also measured and compared to the CsI(Tl) crystal measurements. In addition to experimental work, Monte Carlo simulations using GEANT4 were written to compare ideal pure CsI and CsI(Tl) crystals and to study the effects of radiation damage on the performance of the Belle II electromagnetic calorimeter.

Contents

Supervisory Committee	ii
Abstract	iii
Table of Contents	iv
List of Tables	vii
List of Figures	viii
Acknowledgements	xii
Dedication	xiii
1 Introduction	1
2 The Belle II Experiment and Motivations	3
2.1 The Belle II Experiment	3
2.2 The Belle II Detector	4
2.3 Belle II Backgrounds and Effect on ECL Performance	10
3 Electromagnetic Calorimeter Theory	13
3.1 Particle Interactions in Matter	13
3.1.1 Charged Particle Processes	13
3.1.2 Photon processes	16
3.1.3 Electromagnetic Showers	19
3.1.4 Energy Resolution and Time Resolution	20
3.2 Scintillator Theory and Effects of Radiation Damage	21
3.2.1 Pure CsI vs CsI(Tl)	22
3.2.2 Radiation Damage in CsI(Tl)	24

3.3	Scintillation Light Detection	25
3.3.1	Photomultiplier Tubes (PMT)	26
3.3.2	Photodiodes	26
4	Experimental Apparatus	28
4.1	Crystal Samples Studied	28
4.2	Pure CsI and <i>BABAR</i> CsI(Tl) Crystal Measurements	30
4.2.1	Light Yield Measurements	30
4.2.2	Scintillation Decay Time Measurements	33
4.3	Belle Crystal Measurements	34
4.3.1	Belle Crystal Readout	34
4.4	Belle CsI(Tl) Light Yield Measurements	37
4.4.1	Time Resolution	38
4.4.2	LED Measurements	38
4.5	CsI(Tl) Dosing Methods	38
5	Simulations	42
5.1	Simulation of Pure CsI and CsI(Tl) Scintillation	42
5.1.1	Effect of Wrapping	46
5.1.2	Simulating Radiation Damage	48
5.2	Cosmic Apparatus Simulation	50
5.3	Resolution as a Function of Uniformity	53
6	Analysis Techniques	56
6.1	Light Yield Analysis	56
6.1.1	<i>BABAR</i> CsI(Tl) and pure CsI Light Yields	56
6.1.2	Belle Crystal Light Yields	64
6.2	Scintillation Decay Time and Time Resolution	68
7	Results and Discussion	73
7.1	Comparison of Pure CsI and CsI(Tl)	73
7.2	Radiation Hardness Results	74
7.2.1	Discussion of Mechanism for Radiation Damage in CsI(Tl) and Comparisons	87
8	Conclusions	91

A Appendix	93
A.1 Cosmic Ray Apparatus Trigger Logic	93
A.2 Circuit Diagrams for Belle Crystal Readout	95
A.2.1 Derivation of Model to Describe Light Yield Plateau	100
A.3 Radiation Hardness Light Yield Results	102
A.4 Radiation Hardness Decay Time Results	103
Bibliography	104

List of Tables

Table 3.1	Comparison of pure CsI and CsI(Tl) scintillation properties. . . .	22
Table 4.1	Crystal samples studied indicating detector origin and manufacture.	29
Table 4.2	Readout electronics settings for pure CsI and <i>BABAR</i> CsI(Tl) crystals.	32
Table 4.3	Comparison of Out-E and Out-C light yield parameters.	36
Table 4.4	Contributions to dose errors calculated by NRC.	40
Table 5.1	Pure CsI and CsI(Tl) scintillation parameters used for Uniformity Apparatus simulation.	43
Table 7.1	Measured scintillation properties of CsI(Tl) and pure CsI at 0 Gy.	73
Table 7.2	Nominal values for the accumulated doses where scintillation properties of CsI(Tl) were measured. 1 Gy = 100 rad.	74
Table A.1	Dose values and percent light yields (LY) for CsI(Tl) crystals at all dose stages.	102
Table A.2	Dose values and fitted scintillation times for CsI(Tl) crystals at all dose stages.	103

List of Figures

2.1	Comparison of Belle and Belle II detectors with various sub-detectors labelled.	5
2.2	Transverse plane cutaway view of PXD and SVD layers showing radial positions of beam pipe (thin inner green), PXD layers (black), SVD layers (blue and pink) and CDC (thick outer green).	7
2.3	Illustrations of operating principles for Belle II PID detectors	8
2.4	RPC schematic.	10
2.5	Average light loss observed in crystal rings from 10 years of Belle operation.	11
3.1	Muon interactions in copper over a large energy range.	14
3.2	Feynman diagrams for main charged particle interactions in matter.	14
3.3	Photon total interaction cross-section in lead as function of energy.	17
3.4	Feynman diagrams for main photon interactions in matter.	17
3.5	Schematic of an electromagnetic shower.	20
3.6	Pure CsI band structure.	23
3.7	Pure CsI band structure.	24
3.8	PMT schematic.	26
3.9	PIN diode schematic.	27
4.1	Photographs of typical CsI(Tl) crystals studied showing taper geometry and outer wrapping.	30
4.2	Uniformity Apparatus for measurements of <i>BABAR</i> CsI(Tl) and pure CsI crystals (CsI(Tl) crystal shown in image)	31
4.3	Readout signal chain used for source measurements with pure CsI and <i>BABAR</i> CsI(Tl) crystals.	32
4.4	Typical ^{207}Bi energy spectra measured with CsI(Tl) and pure CsI at 0 Gy dose.	33

4.5	Signal chain for recording cosmic pulses using <i>BABAR</i> CsI(Tl) and pure CsI.	33
4.6	Typical Cosmic Pulses from <i>BABAR</i> CsI(Tl) and pure CsI.	34
4.7	Preamp assembly at back of Belle crystals.	34
4.8	Comparison of Out-E and Out-C readout using UVic Readout Board 1.	35
4.9	Both UVic readout boards. See Appendix A.2 for circuit schematics.	36
4.10	Readout signal chain for Belle CsI(Tl) summed configuration.	37
4.11	Cosmic Test Stand.	37
4.12	Readout signal chain for Belle CsI(Tl) individual diode configuration.	38
4.13	Dosing Setups at NRC Irridation Facility.	39
4.14	Dose non-uniformity across width of crystals calculated from NRC MC simulation. 1 scoring region is equal to 0.5 cm along width of Crystal.	40
4.15	Dose non-uniformity across length of crystals in Group B calculated from NRC MC simulation. 1 scoring region is equal to 6 cm in length along crystal. Note bar face-on corresponds to crystal BCAL3334.	41
5.1	GEANT4 simulation of uniformity apparatus.	43
5.2	GEANT4 ^{207}Bi Spectrum	44
5.3	GEANT4 ^{207}Bi Energy deposition as a function of depth.	45
5.4	Simulated spectra of number of scintillation photons detected from a ^{207}Bi source for pure CsI and CsI(Tl) for absorption length of 40 cm.	46
5.5	Visual comparison of unwrapped vs wrapped events.	47
5.6	Simulated results comparing spectra from wrapped and unwrapped crystals.	47
5.7	Geant4 simulated response longitudinally along crystal for different absorption lengths.	48
5.8	Simulated results of change in average light yield as a function of absorption length of crystal (pure CsI).	49
5.9	Simulated results of change in light yield uniformity as a function of absorption length of crystal.	50
5.10	GEANT4 simulation of cosmic apparatus with many sample muon events (red tracks) passing through paddles and crystals.	50
5.11	GEANT4 simulation comparing longitudinal energy deposits for tapered and non-tapered crystals.	52
5.12	Simulated 500 MeV photon event in CsI.	53

5.13	Weighting functions simulating non-uniform crystal response.	53
5.14	Energy resolution (R plotted with color scale) dependence on crystal non-uniformity.	55
6.1	Fits used to calculate ^{207}Bi peak parameters for CsI(Tl) measurements.	57
6.2	Fits used to calculate ^{207}Bi peak parameters for pure CsI measurements.	58
6.3	Sample calibrations plots for CsI(Tl) and pure CsI	59
6.4	Sample uniformity plot.	61
6.5	Stability of reference crystal throughout study. Statistical error bars are smaller than the points.	62
6.6	Crystal 3348 $\text{LY}_{\text{peak}}^{\text{avg}}$ measurements	63
6.7	Crystal 2234 $\text{LY}_{\text{peak}}^{\text{avg}}$ measurements.	63
6.8	Crystal 5881 $\text{LY}_{\text{peak}}^{\text{avg}}$ measurements.	64
6.9	Measured Pulse Height Histogram with Belle Crystal. Crystal Ball Function fit is also shown.	65
6.10	GEANT4 simulation of muon energy deposits using Cosmic Ray Apparatus.	66
6.11	Belle Crystal non-uniformities at all dosing stages.	67
6.12	Comparison of measured and simulated energy spectrum for self-triggered cosmics.	68
6.13	Fits to scintillation pulses used to measured scintillation decay time components. Note the time scales are different for the two pulses.	70
6.14	Belle Crystal 320017 time resolution histogram at 0 Gy. Note ΔT was calculated at 25 % of the pulse rise time.	71
6.15	Pure CsI time resolution histogram.	72
7.1	Light yields at each dosing stage for all CsI(Tl) crystals studied. Points are connected to help guide the eye.	76
7.2	^{207}Bi spectra measured with crystal 5881 at each dosing stage. Degradation in energy resolution is observed.	77
7.3	<i>BABAR</i> Crystal energy resolution degradation as function of dose.	78
7.4	Correlation between <i>BABAR</i> Crystal resolution at 1 MeV and light yield.	78
7.5	Pink discolouration observed in <i>BABAR</i> CsI(Tl) crystals.	79
7.6	Summary of changes in non-uniformity for <i>BABAR</i> crystals.	80
7.7	Change in Belle crystals light yield from radiation damage.	81
7.8	Uniformity plots for <i>BABAR</i> crystals at 0 Gy and 35 Gy.	82

7.9	Correlation plot for <i>BABAR</i> crystals.	83
7.10	GEANT4 correlation plot for different crystal sizes.	84
7.11	Fast time constants of <i>BABAR</i> CsI(Tl) crystals as function of dose.	85
7.12	Time resolution of Belle crystals as function of radiation dose.	86
7.13	Light yield of diodes on Belle crystals as function of radiation dose.	87
7.14	Sample model fits to data.	89
7.15	Sample modified model fits to data.	90
A.1	Global Trigger logic for Cosmic Ray Apparatus.	93
A.2	Triggering delay logic to differentiate between position triggers.	94
A.3	UVic Readout Board Rev1 used for OUT-C and OUT-E comparison diagram 1/2.	95
A.4	UVic Readout Board Rev1 used for OUT-C and OUT-E comparison diagram 2/2.	96
A.5	UVic Readout Board Rev2 used Belle CsI(Tl) radiation hardness mea- surements diagram 1/3.	97
A.6	UVic Readout Board Rev2 used Belle CsI(Tl) radiation hardness mea- surements diagram 2/3.	98
A.7	UVic Readout Board Rev2 used Belle CsI(Tl) radiation hardness mea- surements diagram 3/3.	99

ACKNOWLEDGEMENTS:

I would like to thank:

My supervisor, Dr. J. Michael Roney for his advice, expertise and support throughout my research and for giving me the opportunity to do research with Belle II.

My co-supervisor, Dr. Robert Kowalewski for his advice and support during my graduate studies.

Dr. Paul Poffenberger for all his advice and assistance in the lab.

The UVic Machine Shop and Electronics Shop for help with apparatus construction.

My fellow officemates and labmates for all the helpful discussions and good company.

My mom and dad for their never ending support and encouragement.

DEDICATION

To mom and dad for all their love and support.

Chapter 1

Introduction

The Belle II experiment will consist of the Belle II detector operating at the world's highest luminosity particle collider, SuperKEKB [1, 2]. The high luminosity of SuperKEKB will come at the cost of high beam backgrounds in the Belle II detector. The higher beam backgrounds will result in radiation damage to the components of the Belle II detector and larger pile-up noise from the low energy background particles continually entering the active material of the detector components. In order to compensate for the higher backgrounds, nearly all Belle sub-detectors are being upgraded for Belle II and new detectors are being added [2].

The electromagnetic calorimeter (ECL) is the sub-detector in Belle II responsible for measuring the energies of particles. The Belle II calorimeter will use scintillators to perform energy measurements. Scintillators are materials that absorb radiation and re-emit the absorbed energy as scintillation light in the visible or near ultra-violet spectrum. The original Belle calorimeter used thallium doped cesium iodide (CsI(Tl)) scintillator crystals. CsI(Tl) demonstrated good performance in Belle however, due to its relatively slow response time and susceptibility to radiation damage, an upgrade to a faster crystal such as pure CsI is being considered for Belle II [2]. A pure CsI upgrade would be a major and expensive undertaking and as a result good justification has to be made before proceeding with the upgrade. The objective of this work is to measure the radiation hardness of large ($5 \times 5 \times 30 \text{ cm}^3$) CsI(Tl) crystals and compare the performance of CsI(Tl) to pure CsI.

The outline for this thesis is as follows. Chapter 2 discusses the Belle II experiment and expands on the motivations of the thesis. Chapter 3 gives an overview of the operating principles of the Belle II ECL, describing how particles interact with the calorimeter and how the deposited energy is measured. In Chapter 4, the ex-

perimental apparatus's constructed and used to study CsI(Tl) and pure CsI crystals are described. Chapter 5 presents the results of Monte Carlo simulations written using the software package GEANT4 [3]. The simulations were used to study ideal pure CsI and CsI(Tl) crystals and effects of radiation damage on crystal performance. Techniques used to analyse measured data are described in Chapter 6 and the results of the study are presented and discussed in Chapter 7. Chapter 8 summarizes the findings of the work and presents the conclusions of the study.

Chapter 2

The Belle II Experiment and Motivations

2.1 The Belle II Experiment

Belle II is a particle detector that will operate at the asymmetric e^+e^- collider, SuperKEKB. Following the successful operation of the Belle detector from 1999 to 2010 at the KEKB collider and the *BABAR* experiment at SLAC, Belle II will be the highest luminosity B-factory ever to operate [1,2]. The main objectives for Belle II are to study Charge-Parity (CP) violation in nature and perform precision measurements mainly in the flavour sector of the Standard Model of Particle Physics. Belle II aims to answer fundamental questions such as, why is the observed baryon asymmetry in the universe so large and what is dark matter?

In order to accelerate and collide e^+e^- particles in the interaction region of Belle II, the SuperKEKB particle accelerator will be used. The centre-of-mass (CM) energy of the collisions will be 10.58 GeV [2]. This energy is selected as it is the mass of a particle resonance called the $\Upsilon(4S)$. The $\Upsilon(4S)$ is a $b\bar{b}$ quark bound state that decays via the strong interaction to $B\bar{B}$ mesons with a 96% branching fraction [4]. The $B\bar{B}$ system created from this decay is an entangled quantum system, that can be used to study matter/antimatter asymmetries. A major triumph of the Belle and *BABAR* experiments was being the first to measure CP-violation in the $B\bar{B}$ system. SuperKEKB will create $\Upsilon(4S)$ particles by colliding e^+ and e^- beams of energies 4 GeV and 7 GeV respectively [2]. Although an energy-asymmetric collider is not the most efficient method to achieve a desired CM energy, the asymmetric collisions result

in the $B\bar{B}$ pair to have a Lorentz boost in the lab frame [2, 5]. The Lorentz boost results in the B-mesons to not be at rest and will increase their decay length, in the lab frame. This allows for the time separation between the two B-meson decays to be measured [2].

The luminosity describes the intensity of the collisions occurring at a particle collider. When the luminosity is multiplied by a production cross section this gives the number of events produced per unit time [5]. A high luminosity is desirable as this leads to high physics event rates. SuperKEKB aims to have a luminosity of $8 \times 10^{35} \text{cm}^{-2}\text{s}^{-1}$ which is about 40 times the luminosity of the KEKB collider [1, 2]. Although a high luminosity is desirable for physics studies, it will result in higher beam backgrounds that will place great strain on the Belle II detector. For this reason, the design goal for the Belle II detector is to achieve the same performance as the Belle detector while operating at the increased luminosity of SuperKEKB [2].

2.2 The Belle II Detector

The main objectives of the Belle II detector are to measure the tracks, momentum, energy and identification of particles leaving the interaction region located in the centre of the detector. Belle II is divided into several concentric layers of sub-detectors that perform these tasks. Figure 2.1 shows a cutaway of the Belle II detector with the various sub-detectors labelled [2]. Each sub-detector is briefly described below.

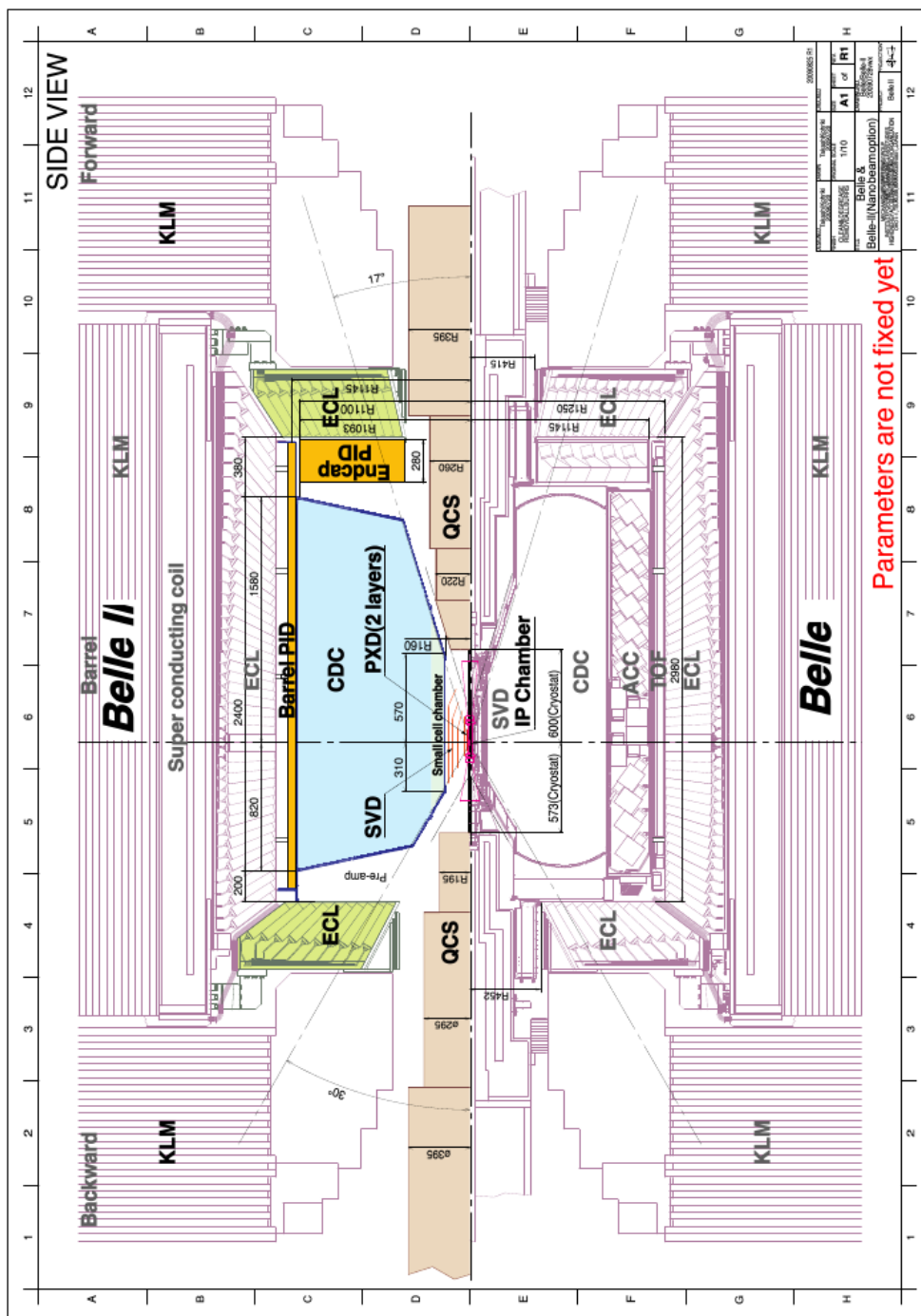


Figure 2.1: Comparison of Belle and Belle II detectors with various sub-detectors labelled [2].

Pixel Detector

The Pixel Detector (PXD) is the first cylindrically shaped sub-detector surrounding the beam pipe and is located 14 mm from the interaction point (IP). The purpose of the PXD is to measure the position of $B\bar{B}$'s decay products leaving the IP. The PXD has two concentric layers of Depleted Field Effect Transistor (DEPFET) semiconductor sensors that are used to make the position measurements. The active material of the DEPFET is a depleted silicon region that is placed under a voltage bias. When a charged particle passes through the silicon it creates electron-hole pairs by ionization. Due to the applied voltage bias, the electron-hole pairs create a current that activates a transistor switch on the sensor signalling that a particle has passed through the pixel area. The first layer of the PXD is divided into 16 sensor areas, $15 \times 90 \text{ mm}^2$ in area, with pixel sizes of $50 \times 50 \mu\text{m}^2$ and the second layer is divided into 24 sensor areas, $15 \times 123 \text{ mm}^2$ in area with pixel sizes of $50 \times 75 \mu\text{m}^2$. The position resolution of the PXD for 0.5 GeV muons will be $2 - 5 \mu\text{m}$ depending on the location of the track in ϕ [2].

Silicon Vertex Detector

The Silicon Vertex Detector (SVD) is located after the PXD and is also used to perform position measurements. The SVD is made from double-sided silicon strip detectors and is divided into four concentric layers. Figure 2.2 shows a schematic cutaway of the inner tracking detectors showing the position of the 4 SVD layers [2]. The operating principle of the SVD is similar to the PXD. As charged particles pass through a silicon strip they ionize creating electron-hole pairs that generate a current in the strip and activate a transistor switch. Unlike the PXD however, each SVD strip does not have good longitudinal position resolution. The area of the pixels on the strip's will be $50 \times 75 \mu\text{m}^2$ or $240 \times 160 \mu\text{m}^2$ depending on location. The position resolution of the SVD for 0.5 GeV muons will be $10 - 30 \mu\text{m}$ depending on the location of the track in ϕ [2].

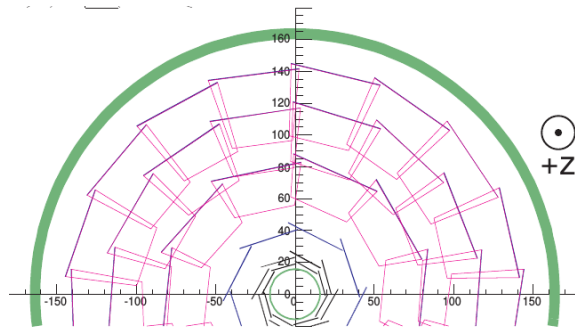


Figure 2.2: Transverse plane cutaway view of PXD and SVD layers showing radial positions of beam pipe (thin inner green), PXD layers (black), SVD layers (blue and pink) and CDC (thick outer green) [2].

Central Drift Chamber

Surrounding the SVD is the cylindrically shaped Central Drift Chamber (CDC) with inner radius 160 mm and outer radius 1130 mm. The CDC operates as a magnetic spectrometer, measuring the tracks of charged particles to determine their momentum and type. The CDC consists of a sealed cylindrical chamber filled with He-C₂H₆ gas which is the active detector material. When charged particles pass through the CDC, they ionize in the He-C₂H₆ gas. In order to measure the magnitude and location of the ionization in the gas, the CDC has 14 336 sensing wires arranged in 56 layers. The wires are divided into two groups, anode and cathode. The cathode wires are grounded and the anode wires are connected to positive high voltage bias. The voltage bias creates an electric field around the wires causing them to attract the ionization electrons. A 1.5 T axial magnetic field permeates the Belle II detector and is used to bend the trajectory of charged particles as they pass through the CDC. By measuring the magnitude of ionization per unit length and the trajectory through the magnetic field, a particle's momentum, charge and type can be determined. The energy loss per unit length, dE/dx , resolution for the Belle II CDC is expected to be 8.5-12 % depending on the incident angle of the particle. [2].

Particle Identification

At high energies, the signals from pion and kaon particles are difficult to differentiate using the CDC. In order to improve the identification of kaons and pions special Particle IDentification (PID) detectors are placed after the drift chamber in the barrel and forward endcap of the detector. The PID detectors perform particle ID by measuring

the speed of the particles leaving the CDC. For low momentum particles, the time difference between beam crossing and interaction with the PID detector is used. For high momentum particles this method is not optimal and instead both PID systems utilize Cherenkov radiation to make measurements. Cherenkov radiation is generated by a particle traversing a material and exceeding the speed of light of that material. When created, Cherenkov light propagates outward in a cone from the particle and the opening angle of the cone is determined by the speed of the particle [2, 4, 6, 7].

For Barrel PID, the detector is a Time-Of-Propagation (TOP) counter. The TOP counter consists of 16 quartz radiator bars with photomultiplier tubes's (PMT) mounted on one end. The TOP counter is located 1243 mm from the IP in-between the CDC and calorimeter. Figure 2.3a shows a schematic of a single TOP counter illustrating its operating principle [2]. Kaons and pions passing through the quartz generate Cherenkov radiation that projects outward and totally internally reflects in the quartz bar. Using timing information and the spatial distribution of light detected at the PMT array, the TOP counter is able to reconstruct the Cherenkov opening angle and measure the speed of the original particle [2].

The PID detector on the endcap is called the Aerogel Ring-Imaging Cherenkov (ARICH) detector and its principle of operation is very similar to the TOP counter. Figure 2.3b illustrates the operating principle of ARICH [2]. Aerogel is used as a medium to generate Cherenkov light from kaons and pions passing through it. The Cherenkov cone is detected by an array of PMTs and the angle of propagation is reconstructed [2].

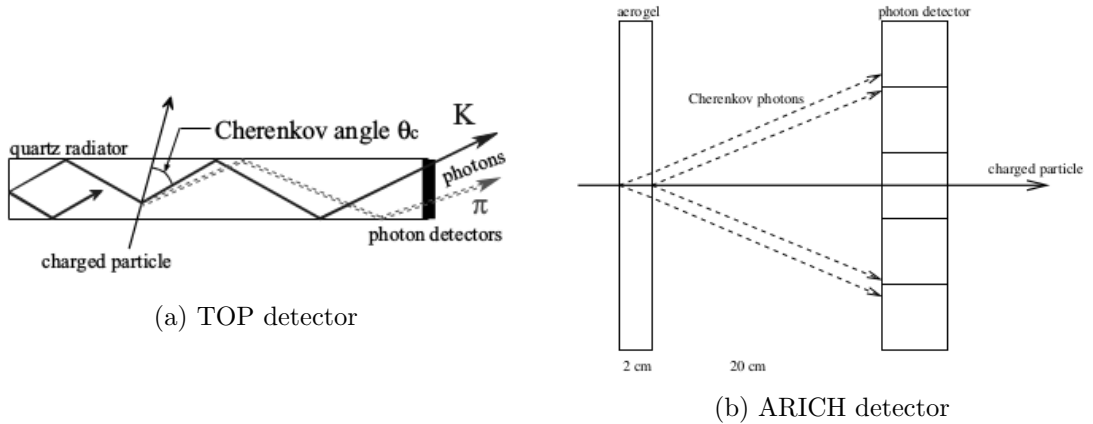


Figure 2.3: Illustrations of operating principles for Belle II PID detectors [2].

Electromagnetic Calorimeter

The Electromagnetic Calorimeter is used to measure the energies of particles that interact through the electromagnetic force. It is also the only detector layer where high energy photons are detected. The Belle II ECL is divided into three regions, the barrel and backward/forward end-caps. The ECL uses CsI(Tl) scintillator crystals as the active material. Particles entering the ECL are attenuated by the CsI(Tl) crystals and their energy is converted to scintillation light. The scintillation light is read out by photodiodes glued to the rear of the crystals. The amount of scintillation light produced by the CsI(Tl) crystals is proportional to the amount of energy deposited in the crystal. Thus by measuring the intensity of scintillation light produced for a given event, the energy of the particle can be determined. Due to concerns of the radiation hardness of CsI(Tl), a possible upgrade to pure CsI scintillation crystals is under consideration by the collaboration and motivates the studies in this thesis [2].

KLM

The KLM is the final sub-detector in Belle II and its purpose is to detect muons and long lived neutral kaons. Muons are long lived and do not lose a significant amount of energy while traversing the tracking detectors and calorimeters and thus will leave the detector. To measure the trajectories of these particles, the KLM detector uses Resistive Plate Chambers (RPCs). As shown in Figure 2.4 RPCs contain multiple layers of electrodes, gas regions and insulators. When a charged particle passes through an RPC they ionize in the gas regions. The large electric field in the gas region accelerates the ionization electrons producing an ionization stream. When the stream reaches the positive plate a fast electrical pulse is generated and is read out using the cathode plane. Using the hit location in KLM and the track in the CDC, muons can be identified. For neutral kaon identification, the kaon must decay in the ECL to charged particles that register hits in the KLM [2].

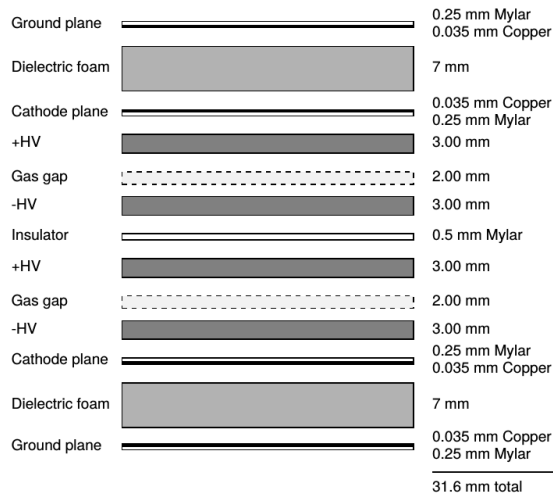


Figure 2.4: RPC schematic [2].

2.3 Belle II Backgrounds and Effect on ECL Performance

The background particles originating from the high luminosity operation of SuperKEKB are expected to impose harsh operating conditions for the ECL. The main beam backgrounds in the Belle II electromagnetic calorimeter will originate from the Touschek Effect, beam gas scattering, Bremsstrahlung and Radiative Bhabhas [2, 8]. The Touschek Effect occurs from Coulomb scattering inside the individual beam bunches. Dipole and quadrupole magnets in the accelerator ring are used to contain the beam particles in bunches as they are accelerated. Internal bunch scattering occurs however and if a significant amount of the longitudinal momentum of the bunch is transferred to the direction perpendicular to the bunch momentum, particles will escape the containment of the accelerator magnets and could enter the detector. Beam gas scattering occurs from the bunch particles scattering off gas particles in the beam pipe due to imperfect vacuum. Discussed in detail in Chapter 3, Bremsstrahlung describes when a charged particles radiates a photon when passing near an atomic nucleus. Radiative Bahabhas occur from electron-positron scattering and will also be a large source of background in the Belle II ECL [2, 8].

The high beam backgrounds will lead to degradation of the energy and time resolution of the calorimeter. The energy resolution of the ECL will degrade due to radiation damage in the CsI(Tl) scintillator crystals. Figure 2.5 shows the signal loss

observed in the Belle ECL crystals after 10 years of operation [2]. It is observed that there was about an 8% drop in light yield for crystals in the ECL due to radiation damage. Without additional radiation shielding in front of the ECL, the radiation dose to the crystals in Belle II is expected to be up to 10 times higher than in Belle [2, 9]. This results in the radiation hardness of CsI(Tl) to be an important crystal property that needs to be well understood.

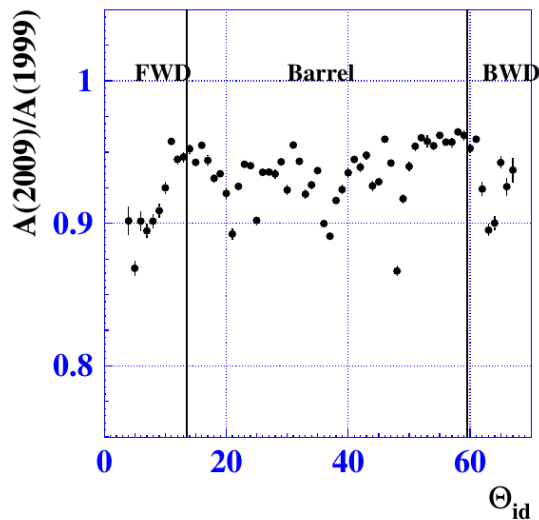


Figure 2.5: Average light loss observed in crystal rings from 10 years of Belle operation [2].

Another major concern for the ECL is degradation of the timing resolution due to pile up noise in the crystals. Pile up noise occurs from beam background particles continually depositing energy in the ECL crystals. The amount of pile up noise in Belle II is expected to be 3 times higher compared to Belle [2]. In order to maintain ECL performance with higher pile-up noise, the readout electronics of the CsI(Tl) crystals are being upgraded to use shorter shaping times [2]. The electronics readout time, however, is limited by the scintillation decay time of CsI(Tl) which is about $1 \mu\text{s}$ [10]. Discussed in Chapter 3, the scintillation time for pure CsI is much shorter (16 ns) and motivates a pure CsI crystal upgrade. The pure CsI upgrade would result in the CsI(Tl) crystals in the ECL forward end-cap to be replaced by pure CsI crystals as this is where the backgrounds are expected to be the highest [2, 11].

The research objectives for this thesis are:

1. Investigate the radiation hardness of large ($5 \times 5 \times 30 \text{ cm}^3$) CsI(Tl) crystals at

absorbed ~ 1 MeV photon doses expected to be reached over the planned 10 year lifetime of the Belle II electromagnetic calorimeter.

2. Measure and compare the energy resolution and timing resolution of CsI(Tl) and pure CsI crystals.

Chapter 3

Electromagnetic Calorimeter Theory

Chapter 3 discusses how the Belle II calorimeter will make energy measurements of particles created from collisions. First particle interactions in matter are reviewed. Then the potential scintillator materials for the Belle II ECL, CsI(Tl) and pure CsI, are discussed. Finally methods of scintillation light detection are described.

3.1 Particle Interactions in Matter

3.1.1 Charged Particle Processes

When traversing a material, charged particles will mainly lose energy by bremsstrahlung at high energies and ionization at low energies. The most probable interaction for a charged particle to undergo depends on the particle type, energy and the material the particle is traversing [4, 7]. To illustrate the dependence on energy, Figure 3.1 shows the stopping power for a muon in copper as a function of the muon energy [4]. The areas where bremsstrahlung (radiative) and ionization (Bethe) dominate energy loss are labelled.

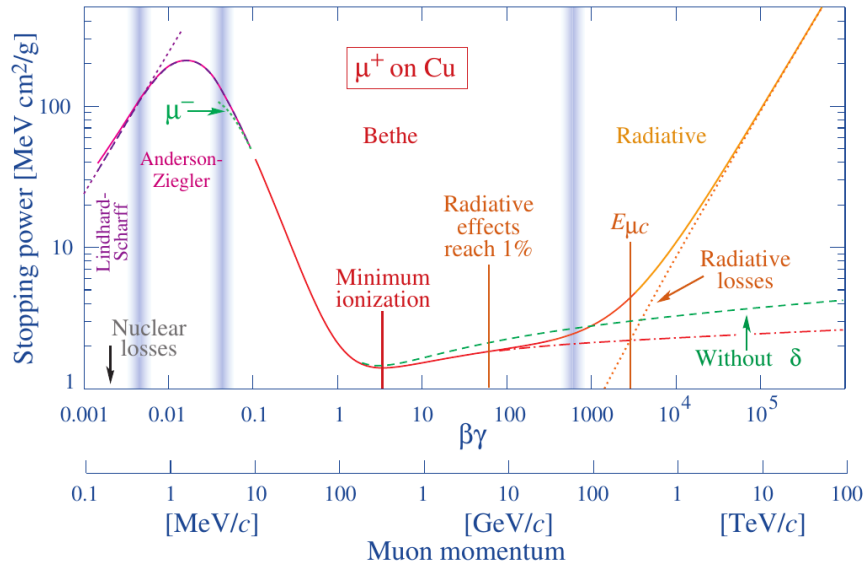


Figure 3.1: Muon interactions in copper over a large energy range [4].

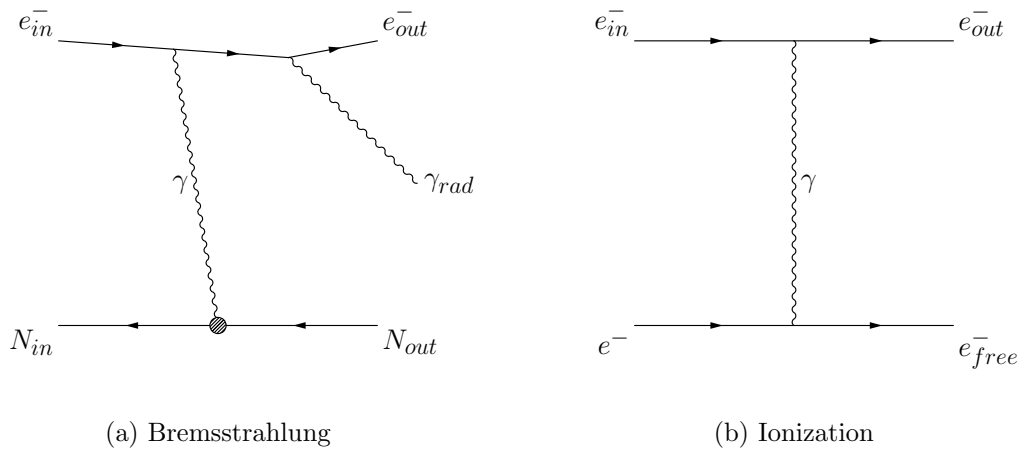


Figure 3.2: Feynman diagrams for main charged particle interactions in matter.

Bremsstrahlung occurs when a charged particle emits a photon when passing near an atomic nucleus. The lowest order Feynman diagram¹ for this process is shown in Figure 3.2a. In bremsstrahlung, a virtual photon γ is exchanged between the incident charged particle and atomic nucleus resulting in a photon to be radiated by outgoing the charged particle. Equation (3.1) gives the energy loss per unit length

¹Feynman diagrams are used to calculate the probability for an interaction to occur. They can also be interpreted from left to right to visualize the interactions between incoming, virtual and outgoing particles for a given process. The charge is indicated by the direction of the arrow on each line.

due to bremsstrahlung at high energies [7]. From equation 3.1, it is seen that the amount of energy loss by bremsstrahlung is dependent on the particles energy and inversely proportional to the particles mass squared. Due to the inverse mass squared dependence, light particles such as electrons will undergo bremsstrahlung much more easily than heavier particles such as protons [6, 7].

$$\left(-\frac{dE}{dx}\right)_{\text{brem}} = 4\alpha N_A \frac{Z^2}{A} z^2 \left(\frac{1}{4\pi\epsilon_0} \frac{e^2}{mc^2}\right)^2 E \ln\left(\frac{183}{Z^{1/3}}\right) \quad (3.1)$$

Where:

Z = atomic number of material

A = atomic weight of material

z = incident particle charge

m = incident particle mass

E = incident particle energy

c = speed of light

N_A = Avogadro constant

The radiation length, X_0 , is a material property that gives the mean free path for bremsstrahlung in a material for a specific particle. For electrons, X_0 is given by equation 3.2 [7].

$$X_0 = \left(4\alpha N_A \frac{Z^2}{A} r_e^2 \ln\left(\frac{183}{Z^{1/3}}\right)\right)^{-1} \quad (3.2)$$

Where:

$$r_e = \text{classical electron radius} = \frac{1}{4\pi\epsilon_0} \frac{e^2}{m_e c^2}$$

Using the definition of the radiation length, the energy loss from bremsstrahlung by electrons can be rewritten as in equation 3.3 [6, 7]. This separates the material dependence (X_0) from the energy dependence showing that $\left(\frac{dE}{dx}\right)_{\text{brem}}$ scales linearly with energy.

$$\left(\frac{dE}{dx}\right)_{\text{brem}} = \frac{E}{X_0} \quad (3.3)$$

At low energies, ionization becomes the dominant process for energy loss. The energy where $\left(\frac{dE}{dx}\right)_{\text{brem}} = \left(\frac{dE}{dx}\right)_{\text{ionization}}$ is defined as the critical energy, E_c [4, 6]. E_c is dependent on the particle type and material type. Illustrated by the first order

Feynman diagram in Figure 3.2b, ionization occurs when a charged particle transfers energy to an atomic electron freeing it in the process. The Bethe-Bloch equation is used to describe energy loss from ionization and is given by equation 3.4 [4, 7].

$$\left(-\frac{dE}{dx}\right)_{\text{ionization}} = Kz^2 \frac{Z}{A} \frac{1}{\beta^2} \left[\frac{1}{2} \ln \frac{2m_e c^2 (\beta\gamma)^2 W_{max}}{I^2} - \beta^2 - \frac{\delta(\beta\gamma)}{2} \right] \quad (3.4)$$

Where:

$$K = 4\pi N_A r_e^2 m_e c^2$$

e = electron charge

$$\beta = \frac{v}{c}$$

$$\gamma = (1 - \beta^2)^{-1/2}$$

m_e = electron mass

I = ionization potential of medium

$\delta(\beta\gamma)$ = relativistic correction

W_{max} = maximum energy transfer from single collision

The magnitude of energy loss from ionization is dependent on the mass and energy of the particle. Particles at the energy to minimally ionize are called minimally ionizing particles (MIPs). Figure 3.1 above labels the minimum ionization energy for muons in copper [4]. As a result of their definition, a MIP will traverse many radiation lengths of material before losing a significant amount of energy.

3.1.2 Photon processes

Analogous to Figure 3.1 for charged particles, Figure 3.3 gives the total interaction cross-section for photons in lead as a function of photon energy [4]. There are three dominant interactions for photons in materials: pair production (κ_{nuc}), Compton scattering and the photoelectric effect. The lowest order Feynman diagram for each of these processes is shown in Figure 3.4. The likelihood for a photon to undergo each of these reactions is dependent on the photons energy [4, 7].

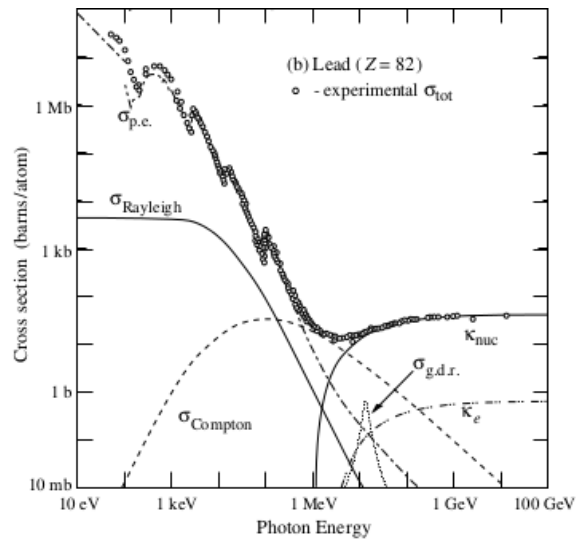


Figure 3.3: Photon total interaction cross-section in lead as function of energy [4].

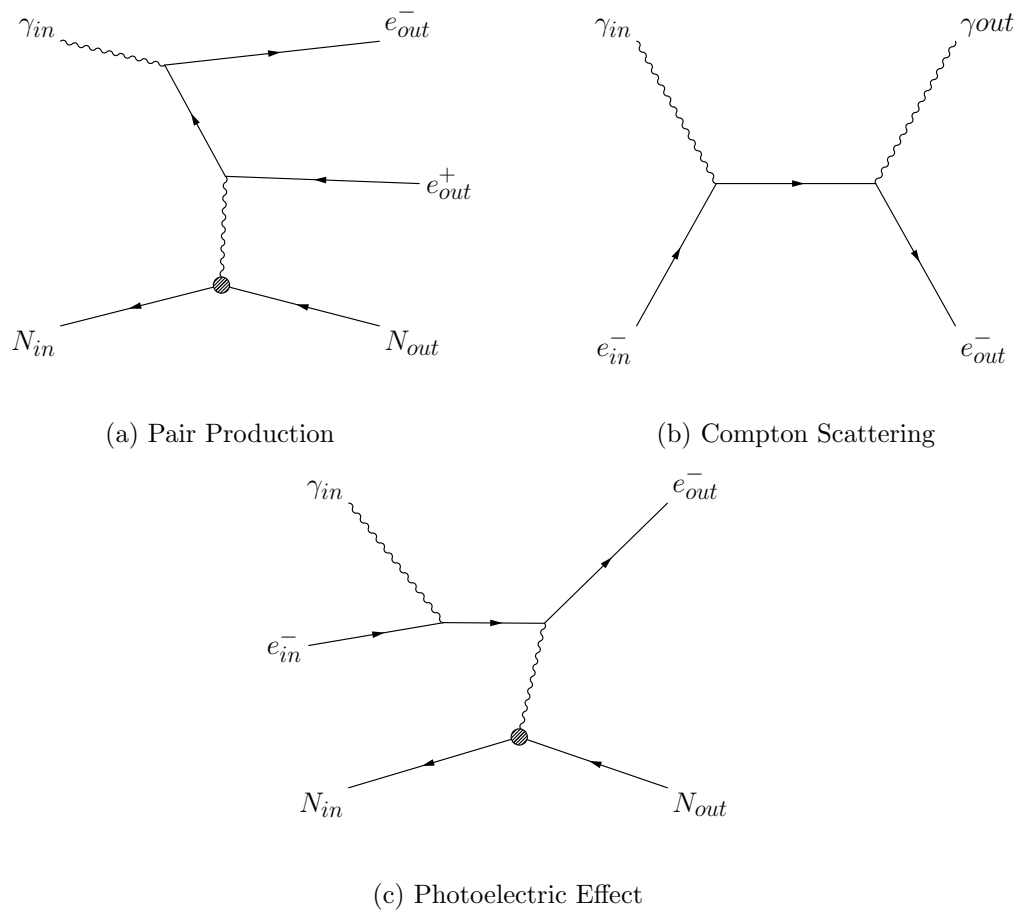


Figure 3.4: Feynman diagrams for main photon interactions in matter.

At high energies, pair production is the dominant photon process in materials. Pair production describes when a photon creates an electron and positron pair through the exchange of a virtual photon with an atomic nucleus. The energy threshold for e^+e^- pair production is given by equation 3.5² [7].

$$E_\gamma \geq 2m_e c^2 + 2 \frac{(m_e c)^2}{m_{\text{nucleus}}} \quad (3.5)$$

Below this threshold Compton scattering dominates photon interactions over a small energy range. Compton scattering occurs when a photon interacts with an atomic electron by transferring some of its momentum [4, 6].

For $O(1 \text{ MeV})$ gamma sources, Compton scattering will be the dominant photon interaction. From four-momentum conservation of a Compton scattering event, it can be shown that the energy of the outgoing photon is only dependent on the scattering angle and is given by equation 3.6 [5].

$$\frac{1}{E_\gamma^{\text{out}}} = \frac{1}{E_\gamma^{\text{in}}} + \frac{(1 - \cos(\theta))}{m_e c^2} \quad (3.6)$$

where

$\theta =$ angle between incoming and outgoing photon

E_{out} is always less than the initial energy of the photon and thus a photon cannot deposit all of its energy by a single Compton scatter. This results in the Compton edge observed when measuring the energy spectrum of gamma sources using intermediate sized radiation detectors³ [12]. The Compton edge arises from the incoming photons undergoing a single Compton scattering event in the detector material and then escaping the detector. As $E_{\text{out}} < E_{\text{in}}$ there is always a gap between the main gamma peak and the Compton edge. Below the Compton edge there is the Compton continuum from scattering events where $\theta < 180$ [12].

At low energies, the photoelectric effect dominates photon processes. The photoelectric effect describes when low energy photons are absorbed by atomic electrons and free them from their bound state. The energy of the outgoing electron is given by equation 3.7 where W is the work function and is a material property related to the binding energy of the atomic electron [12].

²This limit is usually approximated by $E_\gamma \geq 2m_e c^2$ as $m_{\text{nucleus}} \gg m_e$ [7]

³See Figure 4.4a channel number 600 for an example of a Compton edge

$$E_o = hf - W \quad (3.7)$$

where

h = Planck constant

f = photon frequency

E_o = energy of outgoing electron

3.1.3 Electromagnetic Showers

When a high energy electron or photon ($E \gg 10$ MeV) begins traversing a material an electromagnetic (EM) shower will form. EM showers are the result of successive bremsstrahlung and pair production interactions that convert the original high energy particle into many low energy particles. This is illustrated in Figure 3.5 where a photon incident on a material undergoes pair production after one radiation length creating an e^+ and e^- , each with half the energy of the initial photon. Then the e^+/e^- will undergo bremsstrahlung after another radiation length. At each successive stage of the shower the number of particles doubles while the energy of the individual particles decreases. An EM shower will propagate in the material until the energy of the particles reaches the critical energy of the material. Once these particles reach the critical energy, ionization will dominate the energy loss [4, 6, 7].

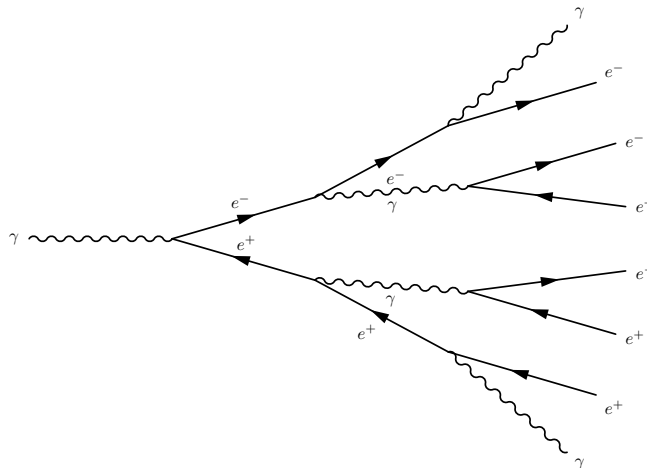


Figure 3.5: Schematic of an electromagnetic shower.

The development of an electromagnetic shower in a material is governed by its radiation length and Moliere radius. As described above, the radiation length is the mean-free-path for bremsstrahlung and $7/9$ the mean-free-path for pair production. The Moliere radius describes the propagation of the shower in the transverse direction due to small angle scattering. When designing a calorimeter it is optimal for the active material to have a small radiation length and Moliere radius so the shower is contained in a small volume. This will optimize the position resolution of the calorimeter [4, 6].

3.1.4 Energy Resolution and Time Resolution

The energy resolution gives a measurement for how accurate a detector can measure energy deposits [7]. A small value of R is desirable in order to have a good signal to background when analysing physics events. For an electromagnetic calorimeter, the energy resolution can be parametrized by equation 3.8 [7, 13].

$$R = \frac{\sigma_E}{E} = \frac{a}{\sqrt{E}} \oplus \frac{b}{E} \oplus c \quad (3.8)$$

where \oplus indicates to sum in quadrature.

The a term in this equation is called the stochastic term and accounts for statistical fluctuations in the number of secondary particles in the shower. The b term is called

the noise term and comes from electronic noise and pile-up. The c term is called the constant term and accounts for imperfections in the calorimeter, leakage, calibration errors and non-uniformities. At high energies, the constant term will dominate the error for a given measurement as it is the only term that is energy independent [6,13].

The time resolution for a detector describes how well it can differentiate between two different events separated in time. The time resolution has units of seconds and is a critical parameter for detectors operating in environments with large background such as Belle II.

3.2 Scintillator Theory and Effects of Radiation Damage

Scintillators are materials that convert energy from ionizing radiation into luminescence. There are many materials that can scintillate and each are characterized by their light yield, linearity and scintillation decay times. The light yield of a scintillator describes how many scintillation photons it can produce per unit of energy deposited. The linearity describes how linear the relationship between light yield and energy deposited is for a scintillator. The scintillation decay time describes how long it takes the scintillator to emit 63% of its scintillation light after an energy deposit. Scintillators are divided into two classes, organic and inorganic [12, 14].

Organic scintillators generally have very fast scintillation decay times and have good light yields, however their linearity when converting light yield to energy is poor. The typical application of an organic scintillator is a trigger used to get accurate timing measurements for when a particle has passed through the scintillator. Inorganic scintillators are generally slower than organic scintillators and can vary in light yield however, they have excellent linearity and are very dense. The typical application of inorganic scintillators is to measure energy deposits from particles [12, 14].

The Belle II Electromagnetic Calorimeter will use inorganic scintillators as the active medium. As with the original Belle ECL, CsI(Tl) will be used in the barrel and backward endcap. Due to concerns arising from the increased luminosity of SuperKEKB, pure CsI in place of CsI(Tl) is being considered for the forward endcap of the calorimeter [2].

3.2.1 Pure CsI vs CsI(Tl)

In terms of composition, CsI(Tl) differs from pure CsI by the doping of thallium that has been found to change the scintillation properties of the crystal. A comparison of the scintillation properties of pure CsI and CsI(Tl) is shown in Table 3.1 [10, 11, 14]. As the concentration of thallium in CsI(Tl) is very small, CsI(Tl) and pure CsI have the same radiation length and Moliere radius. The main differences between the two materials are the scintillation properties. Pure CsI has been found to have a relatively low light yield with a peak emission at 315 nm. Pure CsI also has multiple fast scintillation decay times on the order of 2 – 40 ns each and a slow component on the order of 1 μ s [11, 15, 16]. CsI(Tl) has a very high light yield with the peak emission at 550 nm. In CsI(Tl) there are two scintillation decay components at about 0.8 μ s and 3-5 μ s [10, 14, 15, 17]. The decay times of CsI(Tl) have also been found to vary depending on the particle type [14]. The nominal values for τ_{CsI} and $\tau_{\text{CsI(Tl)}}$ are often quoted as 16 ns and 1 μ s respectively [10, 11]. To understand the origin of these differences, the scintillation mechanism for pure CsI and CsI(Tl) will be discussed.

Table 3.1: Comparison of pure CsI and CsI(Tl) scintillation properties.

Scintillator	X_0 (cm)	Moliere Radius (cm)	Light Yield (γ/keV)	Peak Emission (nm)	τ (ns)
Pure CsI	1.8	3.8	2	315	16
CsI(Tl)			54	550	1000

Pure CsI

In the ideal pure CsI crystal lattice where no impurities or imperfections present, there are three main energy bands. The lowest energy band is occupied by inner atomic electrons. These electrons have high binding energies as they are close to the positively charged nucleus. The outer shell atomic electrons however are screened by the inner electrons and are not as strongly bound. The outer electrons occupy an energy band called the valence band. The highest energy state is in the conduction band. In the conduction band electrons are free to move in the crystal lattice. In pure CsI the valence band and conduction band are separated by a forbidden energy band gap which no electrons can occupy. For an electron to transition from the valence band to the conduction band, enough energy has to be absorbed to overcome the forbidden energy gap. Figure 3.6 shows an illustration of the band gap structure in

pure CsI [14].

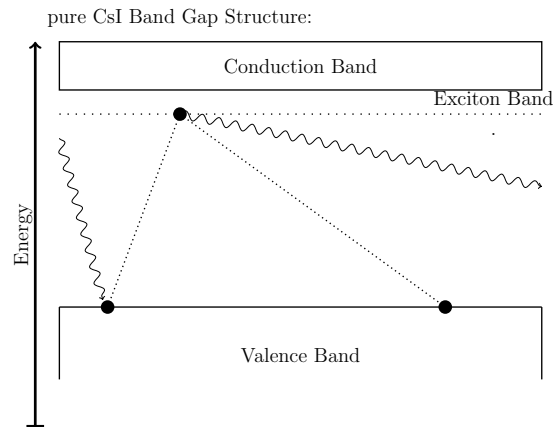


Figure 3.6: Pure CsI band structure.

In its lowest energy state, the valence band of the crystal is fully occupied by atomic electrons in their ground state. When radiation enters the crystal, it transfers energy to the valence electrons. Excitations to the conduction band occur only if sufficient energy to overcome the forbidden energy gap is absorbed. As the energy gap of the forbidden region is on the order of a few eV, energy deposits from high energy particles where $E \gg 1eV$ will typically excite a large number of electrons in the crystal to the conduction band [14].

When enough energy is applied to an electron to overcome the band gap, there are two main processes that can result in pure CsI. The most common process is for the electron to be excited into the conduction band and leave a positively charged hole in the valence band. Once in the conduction band, the electron can migrate throughout the crystal lattice until it finds another hole and then it will de-excite. During this de-excitation the excess energy of the electron will disperse through lattice vibrations (phonons) or by the emission of a photon of energy equal to the band gap. Photon emission through this process is not the primary source of scintillation light in pure CsI because the emitted photon has an energy equal to the band gap separation between the valence and conduction band. Thus there is a high probability that the emitted photon will be reabsorbed by other valence electrons in the pure CsI before exiting the crystal [14].

In order to overcome self-absorption an exciton must form. An exciton is a bound state that can form when the valence electron is excited across the band gap but still remains electrically bound to the hole it leaves in the valence band. Now the electron

will occupy an energy state just below the conduction band called the exciton band. The exciton will eventually recombine and photon emission will take place. As the energy of the exciton band is less than the band gap, the probability of re-absorption is significantly reduced [14].

CsI(Tl)

In CsI(Tl), thallium is doped in pure CsI during crystal growth. Doping pure CsI with thallium results in a significantly higher light yield (Table 3.1). Figure 3.7 illustrates the CsI(Tl) energy gap structure showing the new energy bands locally at the thallium atomic sites [14].

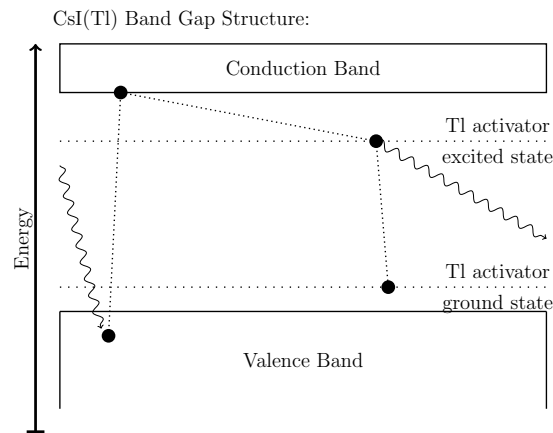


Figure 3.7: CsI(Tl) band structure near Tl impurity.

As with pure CsI, energy from radiation is absorbed by the valence electrons causing them to excite to the conduction band or form an exciton. In CsI(Tl) however, the electrons in the conduction band have the option to first de-excite to a thallium activator site then de-excite again to the valence band or the ground state of the thallium site. In both processes, photon emission occurs such that the photon has an energy smaller than the band gap of the crystal [14]. As the thallium concentration in the crystal increases, the thallium activator scintillation process will dominate over the intrinsic pure CsI scintillation component in CsI(Tl) [18].

3.2.2 Radiation Damage in CsI(Tl)

Absorbed radiation dose describes the amount of energy absorbed by a material per unit mass. The SI unit to measure absorbed dose is the Gray (Gy) and is equivalent

to one joule per kilogram. The electromagnetic calorimeter in Belle II is expected to reach doses of 1-4.5 Gy per year depending on location in the detector and on the performance of any additional radiation shielding placed before the ECL [9]. This is much higher than the accumulated doses experienced after 10 years operation in Belle that was about 1-4.5 Gy total [2].

The radiation hardness of a scintillator describes how well that scintillator can maintain its scintillation properties after absorbing a given dose. There have been past studies of the radiation hardness of CsI(Tl) [17, 19–22]. Large doses of ionizing radiation have been found to decrease the scintillation light yield leaving the crystal. The magnitude of the drop in light yield however has been found to vary crystal-to-crystal depending on crystal size and purity. By analysing the transmission spectrum of irradiated crystals many studies have attributed the decrease in light yield to increased self-absorption in the CsI(Tl) originating from the creation of F-centers [17, 20–23].

An F-centre arises from an electron getting trapped in a positively charged vacancy in the CsI crystal lattice. This vacancy can arise from a variety of sources such as lattice defects or impurities. The trapping of the electron will alter the band gap structure near the capture site allowing more allowed energy states in the forbidden region. The new allowed energy states will be able to absorb the scintillation light produced from the thallium sites and thus increase self-absorption of the crystal [20, 23]. In addition to absorption centres, a study of a small $1 \times 1 \times 1 \text{ cm}^3$ CsI(Tl) crystal, has shown the scintillation mechanism of CsI(Tl) is also affected at very high doses of 5×10^5 Gy [24].

3.3 Scintillation Light Detection

Once the scintillation light leaves the crystal, the final step in determining the magnitude of the original energy deposit is to measure the intensity of the scintillation light. There are numerous methods of scintillation light detection that are used depending on the scintillator and application. For this work, both photomultiplier tubes and PIN diodes were used. These two methods are described below.

3.3.1 Photomultiplier Tubes (PMT)

A PMT consists of two sections, the photocathode and the electron multiplier structure [12]. This is illustrated with the schematic shown in Figure 3.8 [25]. The photocathode is located at the front end of the PMT and is the first element that interacts with scintillation light leaving the crystal. Photocathodes operate using the photoelectric effect. Incoming scintillation light is absorbed by the photocathode atomic electrons. If the electrons absorb enough energy to overcome the work function of the material then they will escape the photocathode. These outgoing electrons are referred to as photo-electrons. The efficiency of a photocathode to convert scintillation photons to photo-electrons is characterized by the quantum efficiency (QE). The QE can vary greatly as a function of material type and wavelength of scintillation light [12].

After the photo-electrons are released from the photocathode they enter the electron multiplication structure. This structure consists of a number of dynodes in vacuum held at high voltages creating a strong electric field. The electric field accelerates the photo-electrons to collide with the dynodes. The dynodes are designed to create electron multiplication from electron collisions. A cascading process occurs as electrons are accelerated dynode to dynode while accumulating charge. Finally the accumulated charge is sent out through a wire as a current. The output current is proportional to the number of scintillation photons that hit the photocathode [12].

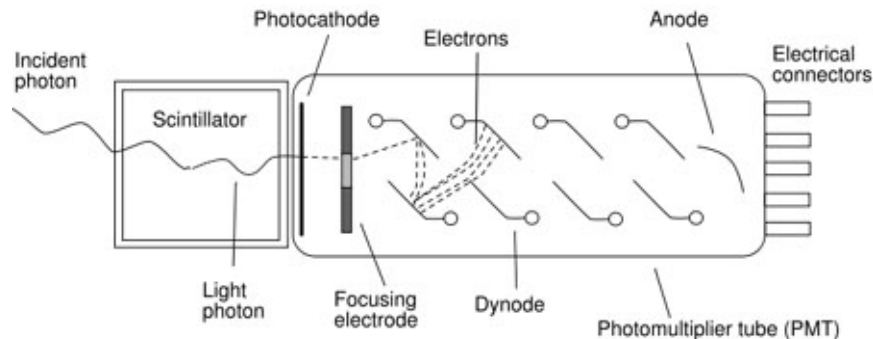


Figure 3.8: PMT schematic [25].

3.3.2 Photodiodes

Photodiodes are another method of scintillation photon readout. In general photodiodes have higher QE's than PMTs and do not require high voltage. PIN diodes

however have no internal gain unlike a PMT that can have several $\times 1000$ gain. The structure of a PIN diode is shown schematically in Figure 3.9 and consists of a P-type, intrinsic type and n-type semiconductor arranged in series and placed under a voltage bias on the order of 50-100 V [12].

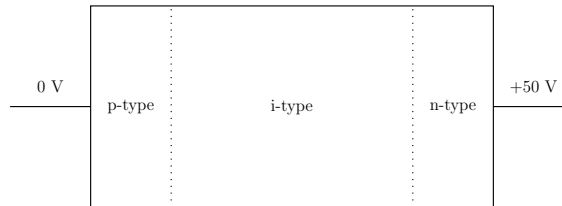


Figure 3.9: PIN diode schematic.

When scintillation photons enter the i-type region of the diode their energy is absorbed and electron hole pairs are created. As the diode is under a voltage bias the electrons will drift towards the p-type end creating a current out of the n-type end. The magnitude of the resulting current is proportional to the the number of scintillation photons that hit the PIN diode [12].

Chapter 4

Experimental Apparatus

4.1 Crystal Samples Studied

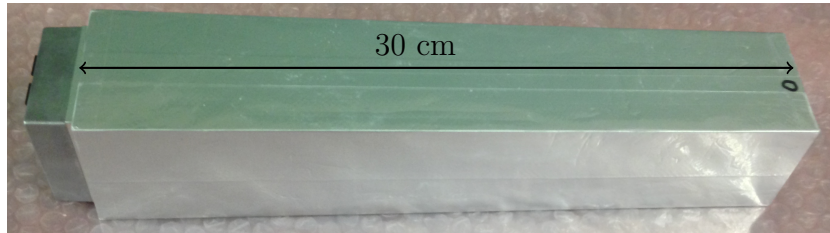
Table 4.1 identifies the crystals studied for this thesis and their manufacturer¹. All CsI(Tl) crystals studied were spare crystals from the *BABAR* or Belle experiments. These crystals were previously undosed and are representative of the quality of crystals that are used in large particles detectors such as Belle II. The Belle II spare crystals used for the radiation hardness studies are spares from the forward end-cap of the ECL. It is critical to test the crystals in this region of the ECL as they are the crystals that would be replaced by pure CsI if the collaboration proceeds with the pure CsI upgrade [2].

¹SIC = Shanghai Institute of Ceramics

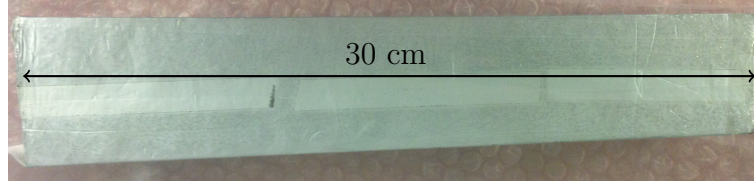
Table 4.1: Crystal samples studied indicating detector origin and manufacture.

Crystal Type	Detector Origin	Crystal ID	Manufacturer
Pure CsI	-	-	AM Crystals
CsI(Tl)	Belle	320017	SIC
		334017	SIC
		315065	SIC
	<i>BABAR</i>	BCAL02410	SIC
		BCAL02922	SIC
		BCAL02676	SIC
		BCAL03348	Chrismatec
		BCAL02234	Chrismatec
		BCAL03334	Chrismatec
		BCAL05881	Kharkov
		BCAL05883	Kharkov

Figure 4.1 shows pictures of the typical Belle and *BABAR* crystals used. All crystals were wrapped in a layer of $200\mu\text{m}$ thick teflon and $40\mu\text{m}$ thick aluminized mylar as they would be in Belle II [2]. The purpose of the wrapping is to increase the light yield at the detector end by reducing light leakage. All crystals were shaped as a rectangular trapezoid with a slight taper such that the readout face of the crystal was larger than the front face of the crystal. The majority of crystals were 30 cm in length except BCAL5881 and BCAL5883 which were 31.5 cm long. The readout and front face of each crystal varied with the typical size being $5 \times 5 \text{ cm}^2$.



(a) Typical Belle crystal with teflon and aluminized mylar wrapping.



(b) Typical *BABAR* crystal with teflon and aluminized mylar wrapping.

Figure 4.1: Photographs of typical CsI(Tl) crystals studied showing taper geometry and outer wrapping.

Two experimental apparatuses were used to evaluate the characteristics of the scintillation crystals. Each apparatus was designed to facilitate the different scintillation light readout methods used.

4.2 Pure CsI and *BABAR* CsI(Tl) Crystal Measurements

4.2.1 Light Yield Measurements

The *BABAR* CsI(Tl) crystals and the pure CsI crystal were read out using a R5113-02 PMT made by Hamamatsu [26]. The R5113-02 is a R329-02 model PMT with a UV glass window allowing it to be used with pure CsI that scintillates at 315 nm [11, 26]. The high gain provided by the PMT allowed for light yield measurements to be made with a ^{207}Bi gamma source (the photodiodes on the Belle Crystals were not sensitive enough to detect the source). The apparatus used to conduct these measurements is shown in Figure 4.2.

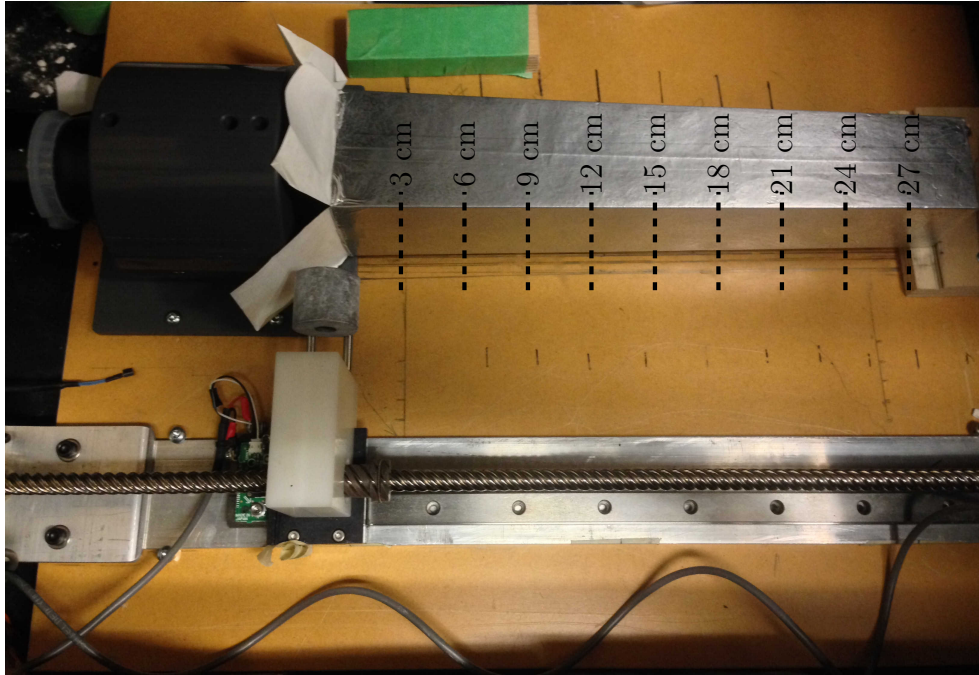


Figure 4.2: Uniformity Apparatus for measurements of *BABAR* CsI(Tl) and pure CsI crystals (CsI(Tl) crystal shown in image)

The Uniformity Apparatus consisted of a mount for the PMT and crystal as well as a stepper-motor controlled automated track for carrying the source and lead collimator. The mounts and the track were secured in place in order to have consistent relative positioning. The entire apparatus was enclosed in a dark box to prevent damage to the PMT and eliminate background light from the room. During operation, dry nitrogen gas was flushed into the dark box in order to reduce the humidity. Although CsI(Tl) and pure CsI crystals are only slightly hygroscopic, they should not be exposed to high humidity for extended periods of time [10,11]. During measurements, the typical relative humidity (RH) was 20 - 40 %. In storage the crystals were sealed in plastic with desiccant where the RH was $< 10\%$. Temperature measurements were recorded during each measurements and fluctuated less than $\pm 2^\circ\text{C}$. An air coupling was used between the PMT and the crystals. Although this did not optimize the light collection efficiency, it provided a reproducible day to day optical coupling between the PMT and crystal.

The signal chain used to acquire gamma spectra is shown in Figure 4.3. Pulses from the PMT were integrated by a Tennelec shaping amplifier. After integration and amplification, uni-polar pulses were sent to a Tracor Northern multichannel analyser (MCA) where the pulse heights were recorded in a histogram. Gamma spectra

recorded on the MCA were saved to a computer for analysis. Table 4.2 outlines the shaping amplifier settings used for pure CsI and CsI(Tl). The linearity of this signal chain was confirmed using a pulser.

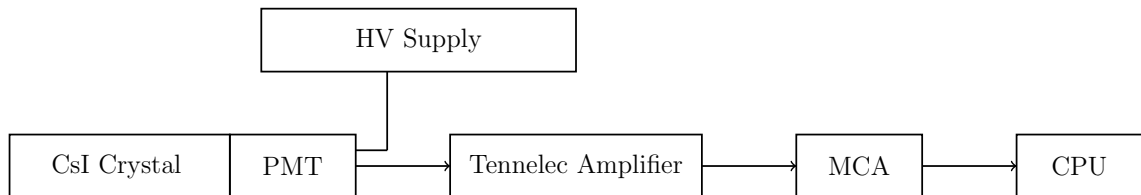


Figure 4.3: Readout signal chain used for source measurements with pure CsI and *BABAR* CsI(Tl) crystals.

Table 4.2: Readout electronics settings for pure CsI and *BABAR* CsI(Tl) crystals.

Type	Amplifier	Shaping Time	Gain	HV on PMT
Pure CsI	Tennelec	0.5 us	100	1850 V
CsI(Tl)	Tennelec	6 us	300	1700 V

Each uniformity measurement consisted of recording nine ^{207}Bi gamma spectra at 3 cm spacings along the crystal, beginning 3 cm from the PMT face. These positions are labelled in Figure 4.2. ^{207}Bi was used as it has three main gamma peaks at 0.569 MeV, 1.064 MeV and 1.77 MeV thus allowing for various depths² of the crystal to be tested as well as providing enough points for a reliable calibration of channel number to energy to be calculated [27]. Figure 4.4 shows typical ^{207}Bi spectra recorded by pure CsI and CsI(Tl).

²See Figure 5.3

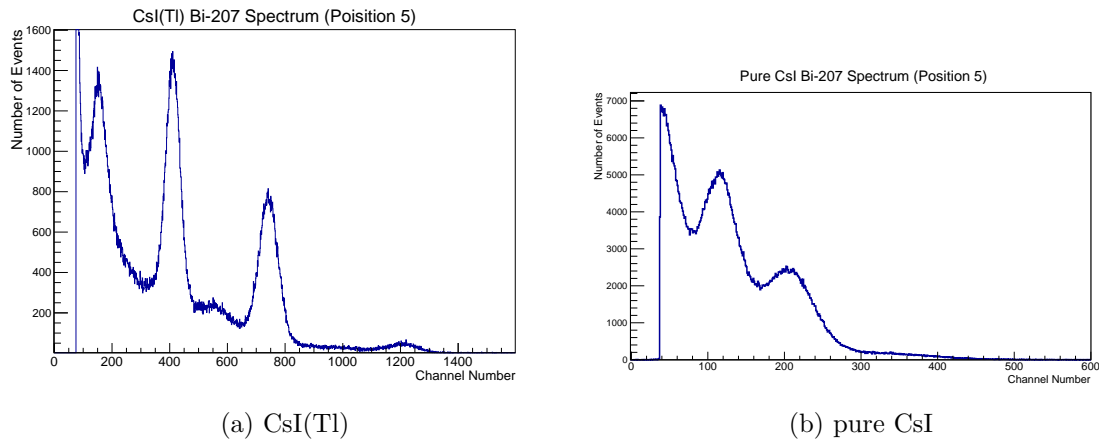


Figure 4.4: Typical ^{207}Bi energy spectra measured with CsI(Tl) and pure CsI at 0 Gy dose.

4.2.2 Scintillation Decay Time Measurements

In order to measure the scintillation decay times of the pure CsI and *BABAR* CsI(Tl) crystals, cosmic rays were used. These measurements used the same PMT and dark box as the uniformity measurements described above, however the signal chain was modified. The modified signal chain is shown in Figure 4.5 where pulses from the PMT are sent to an Tektronix oscilloscope where they were digitized and then saved to a computer. No triggering was used to filter the direction of the accepted cosmic rays for CsI(Tl) that had pulse heights of ~ 1 V and a discriminator was set at about 175 mV to filter out noise. Figure 4.6 shows typical scintillation pulses from pure CsI and CsI(Tl);

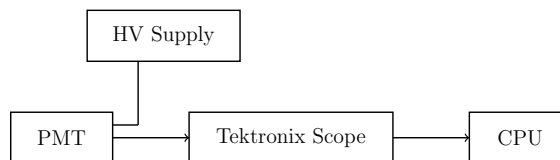


Figure 4.5: Signal chain for recording cosmic pulses using *BABAR* CsI(Tl) and pure CsI.

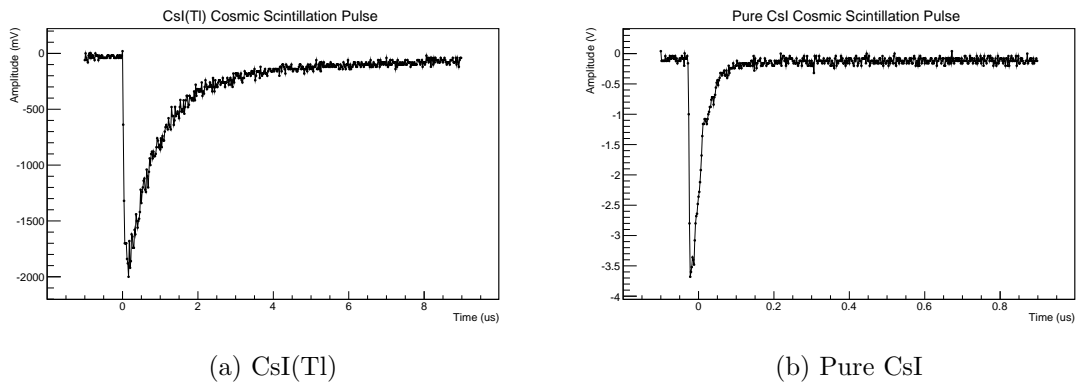


Figure 4.6: Typical Cosmic Pulses from *BABAR* CsI(Tl) and pure CsI.

4.3 Belle Crystal Measurements

4.3.1 Belle Crystal Readout

Each Belle CsI(Tl) crystal had two PIN photodiodes glued to the back of the crystal. Signals from the diodes were immediately shaped by a preamp also attached to the back of the crystal. Figure 4.7 shows the preamp assembly attached to each Belle crystal. During operation at Belle II, the shaped diode signals are summed by a shaper circuit where further pulse analysis would occur. As the shaper circuit was not available for this study, a readout board was designed at UVic to readout the signals from the Belle pre-amp. Appendix A.2 shows circuit diagrams for the UVic readout board.



Figure 4.7: Preamp assembly at back of Belle crystals.

Each diode on the Belle crystals has two outputs, a collector output (OUT-C) and emitter output (OUT-E). In Belle and Belle II the OUT-C signals are summed and analysed while OUT-E is connected to ground. This is because the OUT-E signal is unstable for very large scintillation pulses (1 GeV events) [28]. It was suggested that the OUT-E output however would give superior performance over the OUT-C output. The first version of the UVic Readout Board consisted of independent summing configurations for both OUT-E and OUT-C. This was done to compare the two signals and see if OUT-E would be sensitive enough for ^{207}Bi source measurements. The results of the comparison are summarized in Figure 4.8 and Table 4.3.

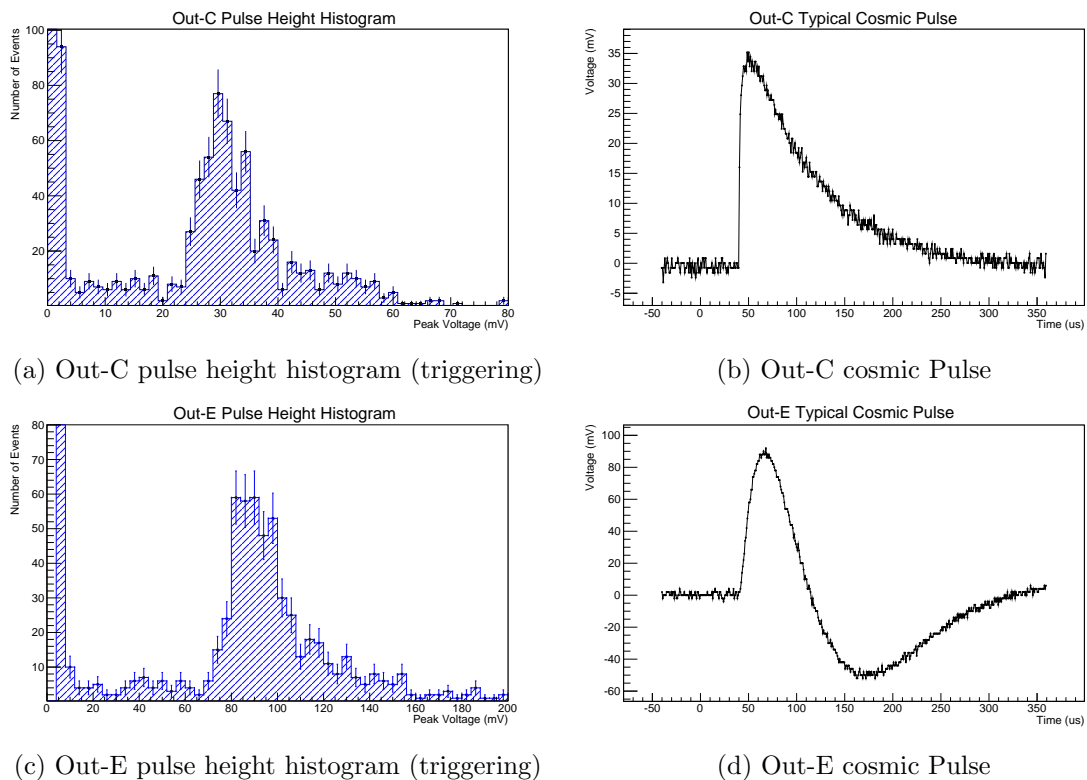


Figure 4.8: Comparison of Out-E and Out-C readout using UVic Readout Board 1.

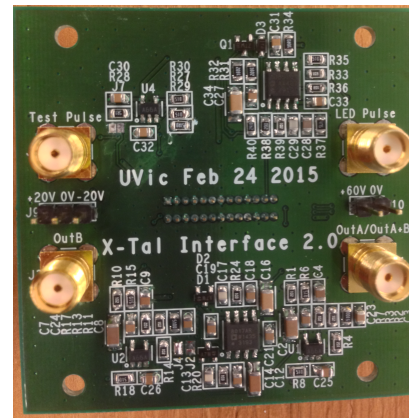
Table 4.3: Comparison of Out-E and Out-C light yield parameters.

Configuration	AVG Pulse Height	RMS noise / pulse height
OUT - C (Belle Circuit)	30 mV	2.3 %
OUT - E	90 mV	1.6 %

OUT-E was found to have a superior signal to noise ratio. However, the OUT-E configuration was still unsuccessful in acquiring a ^{207}Bi source spectrum. As a result, a second board was design with only the Out-C method, as this is what will be used at Belle II. The second board had options for Summed Diode Output, Individual Diode Output, LED Pulsing and a Test Pulse. Pictures of both readout boards are shown below Figure 4.9.



(a) First UVic Readout board with Out-E and Out-C configurations.



(b) Final UVic Readout board with only Out-C and options for individual diode readout, LED pulsing and test pulse.

Figure 4.9: Both UVic readout boards. See Appendix A.2 for circuit schematics.

The final signal chain for the Belle crystal pulse readout is shown in Figure 4.10.

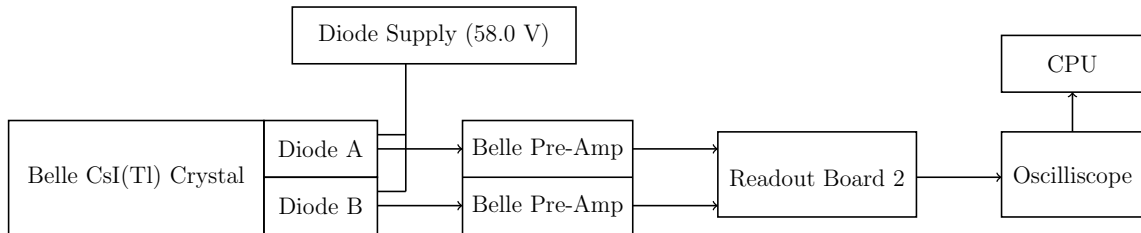
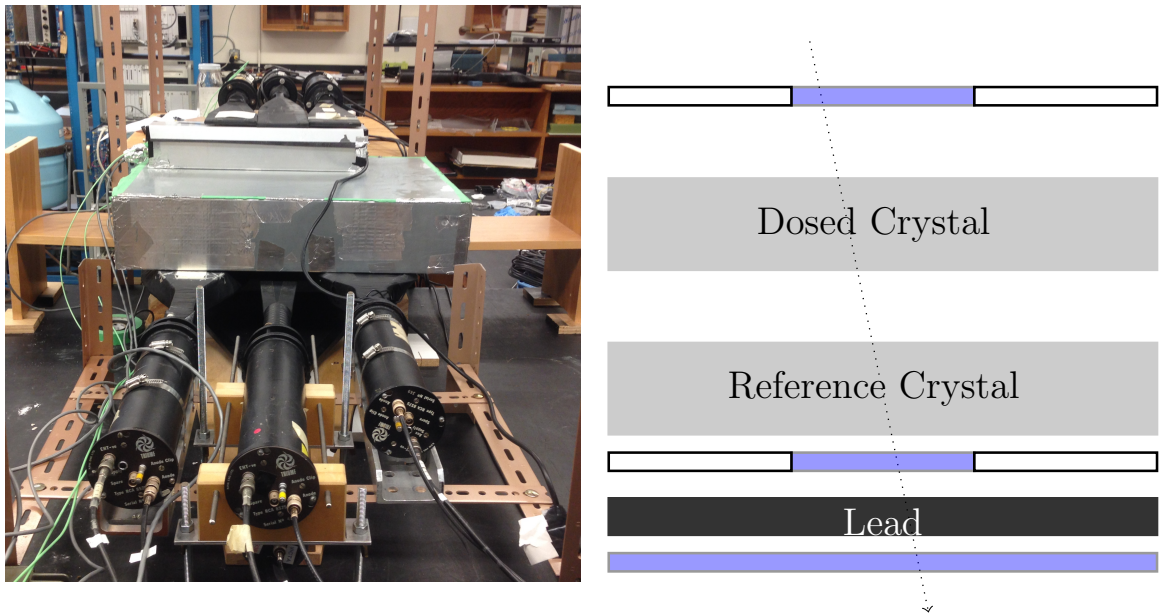


Figure 4.10: Readout signal chain for Belle CsI(Tl) summed configuration.

4.4 Belle CsI(Tl) Light Yield Measurements

A cosmic ray test stand was assembled in order to do uniformity measurements on the Belle crystals. Figure 4.11 shows a picture and schematic of the cosmic test stand.



(a) Cosmic Ray Test Stand for measurements on Belle CsI(Tl) crystals.

(b) Schematic showing example trigger condition.

Figure 4.11: Cosmic Test Stand.

Seven plastic scintillators were assembled dividing the crystal longitudinally into three 10 cm long sections (Near Diode, Middle, Far from Diode). A 2.54 cm thick lead plate was placed before the last scintillation paddle trigger to further filter out non-MIPs. Pulses from the plastic scintillator paddles were sent to a gate generator and then to coincidence units. The external trigger of the oscilloscope was connected to a global trigger that signalled when three vertically aligned paddles recorded a

coincidence event. Figure 4.11 shows an example trigger condition for the middle section. For each global trigger, the output from the Test and Reference Crystal was saved as well as the signal from the Local Position Trigger. Logic diagrams for the coincidence signal chains can be found in Appendix A.1.

4.4.1 Time Resolution

The second version of the readout board had the ability to monitor each diode individually. This allowed for the light yields of each individual diode to be measured and well as for time resolution measurements of the diodes to be calculated. Figure 4.12 shows the signal chain when recording individual diode events.

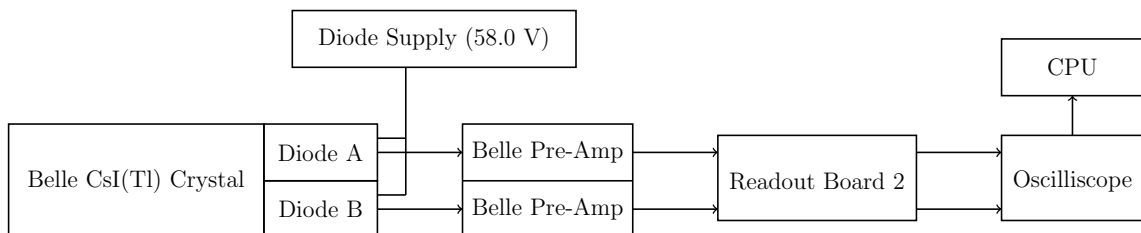


Figure 4.12: Readout signal chain for Belle CsI(Tl) individual diode configuration.

4.4.2 LED Measurements

A third option on the Belle Readout board allowed for pulsing of a green LED located on the Belle crystal electronics. Pulsed LED measurements were taken to measure the change in transmission of the crystals. It was found that the LED output was unstable however and transmission measurements could not be made using the LED.

4.5 CsI(Tl) Dosing Methods

The CsI(Tl) crystals were dosed at the National Research Council (NRC) Irradiation Facility in Ottawa, Canada using 1.17 MeV and 1.33 MeV gamma rays from a ^{60}Co source. All dose calculations and measurements were completed by the NRC [29]. The crystals were dosed at a dose rate of about 0.2 Gy/min in stages of 2, 10 and 35 Gy accumulated dose allowing the scintillation properties of the crystal to be studied as a function of accumulated dose.

The CsI(Tl) samples were divided into two dosing groups, Group A and Group B. Group A consisted of crystals 320017, 3348, 2922 and 2676 and Group B consisted

of crystals 334017, 2234, 3334, 5881 and 5883. Figure 4.13 show the irradiation apparatuses used to dose Group A and Group B.



Figure 4.13: Dosing Setups at NRC Irridation Facility [29].

The brown plastic shown in Figure 4.13 is virtual water. The purpose of the virtual water is to serve as a homogeneous control material where the dose rate to the virtual water, $\frac{dD_w}{dt}$, can be measured prior to irradiating the crystals. The clear plastic surrounding the crystals is used to create additional scattering which increases the uniformity of the dose at the crystal edges [29].

The absorbed dose in the CsI(Tl) crystals was calculated using equation 4.1.

$$D_{\text{CsI}} = \frac{dD_w}{dt} t_{\text{irr}} f_{\text{CsI}} \quad (4.1)$$

where f_{CsI} is a conversion factor to convert the dose deposited in virtual water to dose deposited in CsI and t_{irr} is the irradiation time [29].

Prior to dosing the crystals, the apparatus was constructed without the crystals and $\frac{dD_w}{dt}$ was measured by placing an ionization chamber in the virtual water block.

The entire apparatus was then simulated in MC and the conversion factor f_{CsI} was calculated for each crystal. Using this information an irradiation time was calculated in order to determine how long the apparatus must be irradiated to achieve the desired dose in the CsI. The error on each dose was determined to be 2 % from the components outlined in Table 4.4 [29, 30].

Table 4.4: Contributions to dose errors calculated by NRC [29, 30].

Error Component	Error (%)
Conversion Factor, f	1.8
Dose measurement in water	0.5
Ionization chamber repeatability	0.1
Irradiation time	Negligible ($\ll 0.1$)
Total	2

All of the crystals in Group A were given uniform dosing profiles throughout the crystal. This was achieved by rotating the crystals 180 degrees halfway between doses in order to overcome the attenuation of the ^{60}Co gammas in the CsI. In Group B, crystal BCAL3334 was given a longitudinally non-uniform dosing profile and was not rotated when dosed. The remaining crystals in Group B followed the same procedure as Group A in order to acquire a uniform dose. Figure 4.14 shows the dose non-uniformities calculated by the NRC across the width of the crystals using the uniformity method [29]. The longitudinal dose non-uniformity is shown in Figure 4.15.

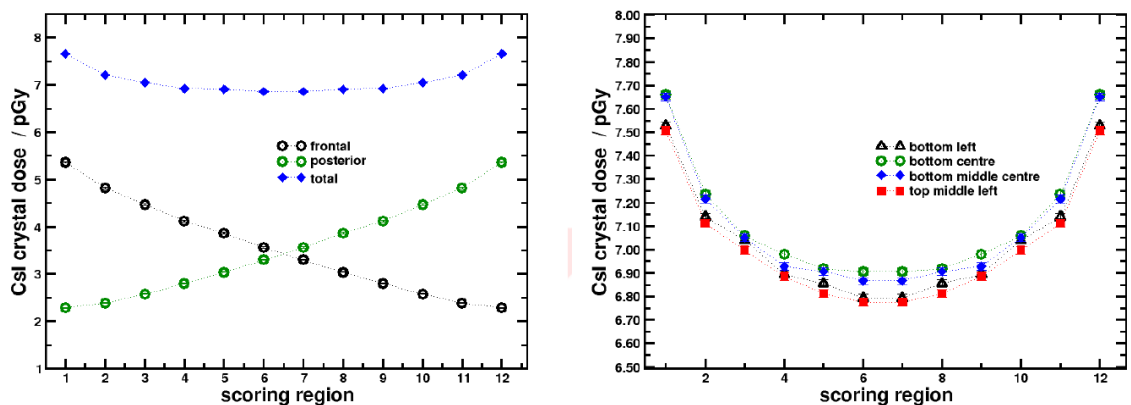


Figure 4.14: Dose non-uniformity across width of crystals calculated from NRC MC simulation. 1 scoring region is equal to 0.5 cm along width of Crystal [29].

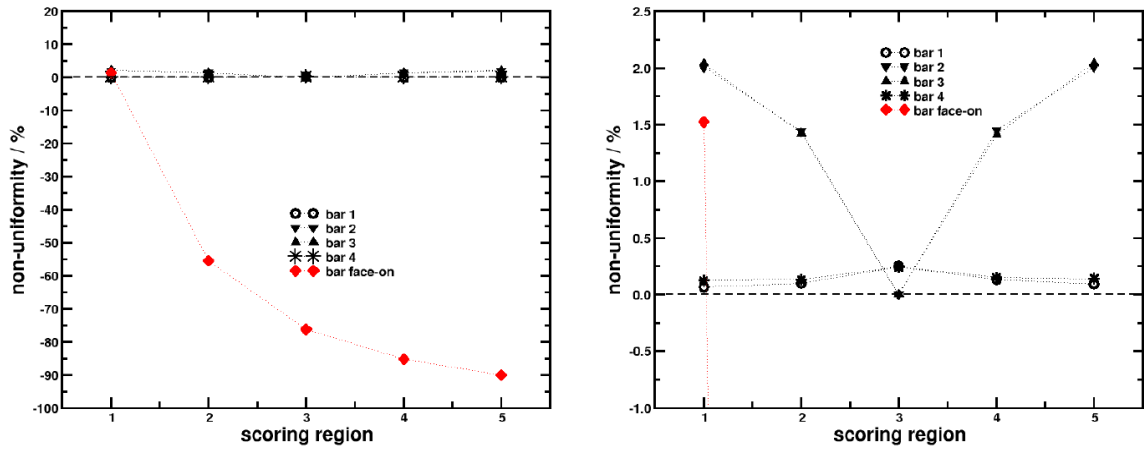


Figure 4.15: Dose non-uniformity across length of crystals in Group B calculated from NRC MC simulation. 1 scoring region is equal to 6 cm in length along crystal [29]. Note bar face-on corresponds to crystal BCAL3334.

Chapter 5

Simulations

Monte Carlo simulations were written using the GEANT4 software package to simulate the experimental apparatuses described in Chapter 4. In doing so, the performance of ideal pure CsI and CsI(Tl) crystals was studied. In addition, a simulation was written to calculate the sensitivity of crystal non-uniformities on the energy resolution for photons in the energy range of 20 MeV to 10 GeV.

5.1 Simulation of Pure CsI and CsI(Tl) Scintillation

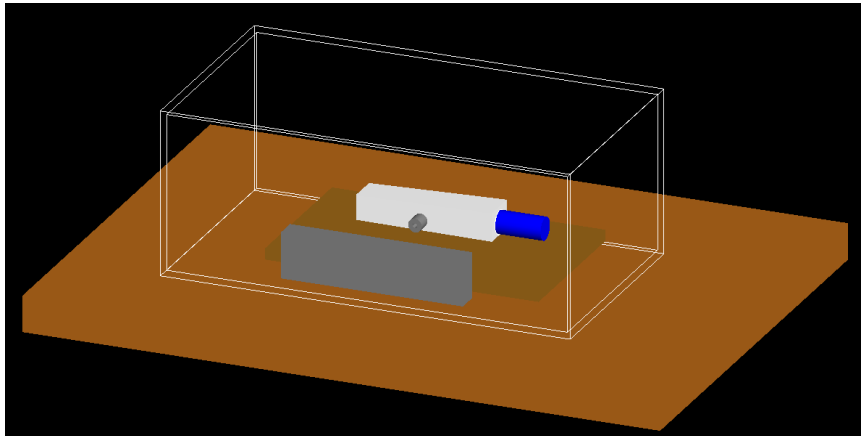
The Uniformity Apparatus described in Chapter 4 was simulated and is shown in Figure 5.1. All features surrounding the crystal such as the wooden platform, lead shielding and the aluminium dark box were modelled in order to accurately simulate backscattering events. This was found to be necessary in order to reproduce the spectra measured in the lab.

In order to compare pure CsI and CsI(Tl), scintillation processes were included in the GEANT4 Physics List. An example scintillation event from pure CsI is displayed in Figure 5.1b showing a 500 keV gamma ray (green) depositing energy in the CsI crystal and generating scintillation light (yellow).

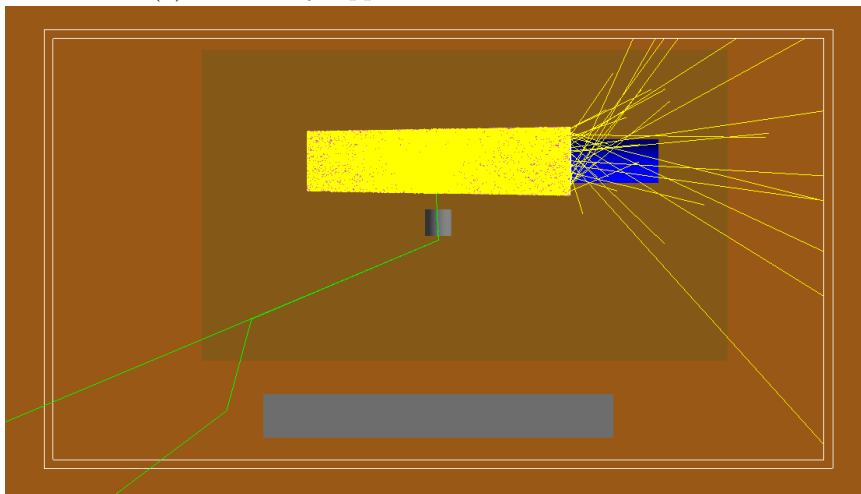
The CsI and CsI(Tl) simulations differed only by their scintillation parameters. Table 5.1 lists the parameters used for the simulations:

Table 5.1: Pure CsI and CsI(Tl) scintillation parameters used for Uniformity Apparatus simulation.

Scintillator	Light Yield	Time Constant	Peak Emission
Pure CsI	$2 \gamma / \text{keV}$	16 ns	315 nm
CsI(Tl)	$54 \gamma / \text{keV}$	1000 ns	550 nm



(a) Uniformity Apparatus simulated in GEANT4



(b) Example pure CsI scintillation event.

Figure 5.1: GEANT4 simulation of uniformity apparatus.

To accurately model a ^{207}Bi source, 0.559, 1.063 and 1.770 MeV photon events were generated. The relative number of events generated for each energy was equal to the relative intensity emitted by ^{207}Bi and the direction of the photons was randomly distributed. Figure 5.2 shows a typical spectrum of the energy deposited in the crystal from the simulated ^{207}Bi source. High intensity peaks at the three ^{207}Bi energies are

present as well as Compton edges. A lower intensity peak near 1269 keV is also visible. This peak is caused by 511 keV gammas created from positron annihilation escaping the crystal. Observation of these features is a good validation of the physics list being used.

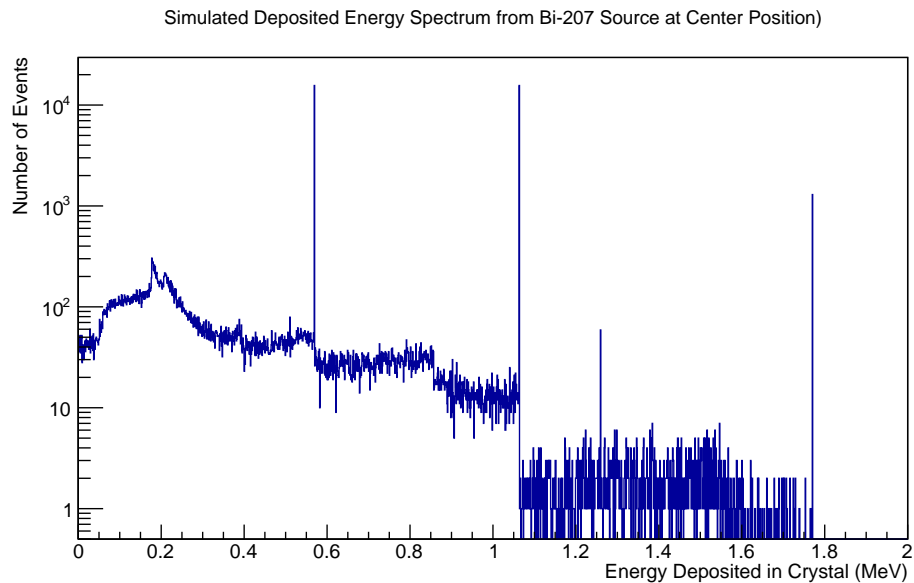


Figure 5.2: GEANT4 ^{207}Bi Spectrum

By simulating many events, the accumulated energy deposited at various depths across the crystal width is calculated and shown in Figure 5.3. The majority of the energy deposited from the ^{207}Bi source is deposited in the first 4 cm of the crystal. As the widths of the crystals studied varied from 3 cm to 7 cm this confirms that the scintillation mechanism across the crystal is being tested.

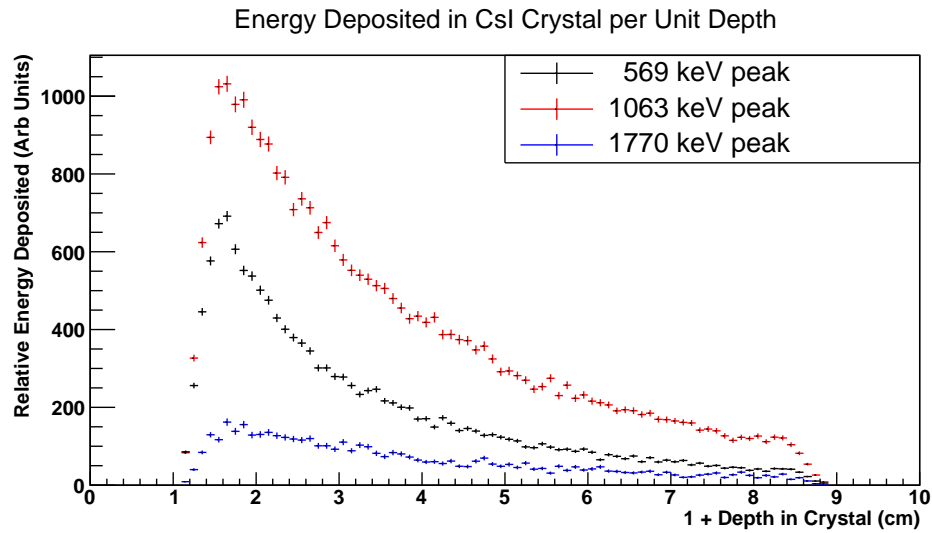


Figure 5.3: GEANT4 ^{207}Bi Energy deposition as a function of depth.

By counting the number of scintillation photons detected at the PMT, a realistic scintillation energy spectrum was produced for CsI(Tl) and pure CsI. Sample spectra of the number of scintillation photons detected by the PMT are shown in Figure 5.4a for pure CsI and 5.4b for CsI(Tl). A major goal of this simulation was to verify that the poor resolution of the pure CsI scintillator observed in the lab is the result of low photon statistics. This simulation was successful in confirming this hypothesis.

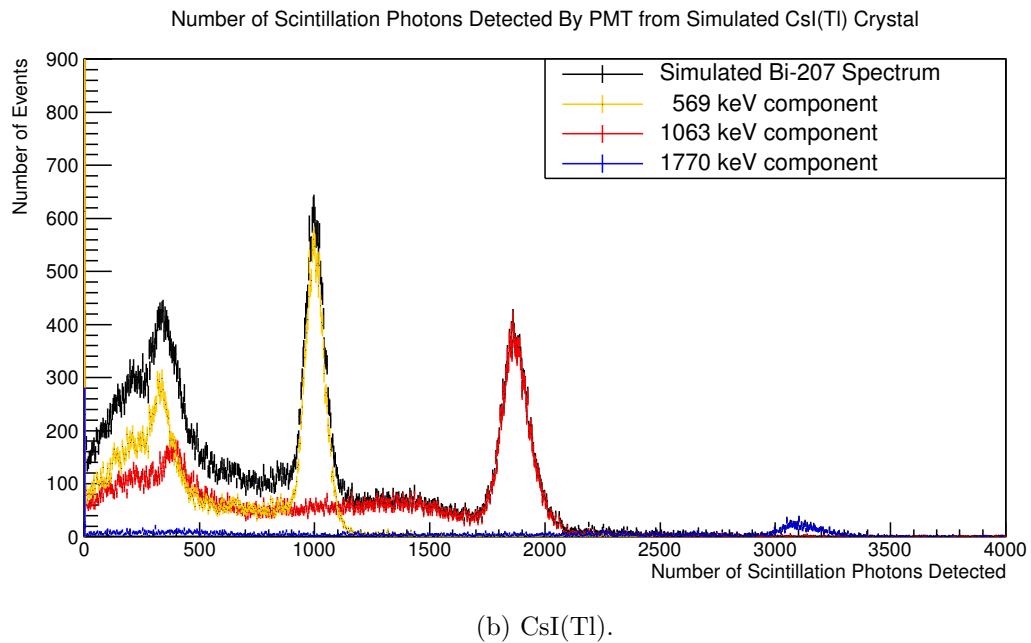
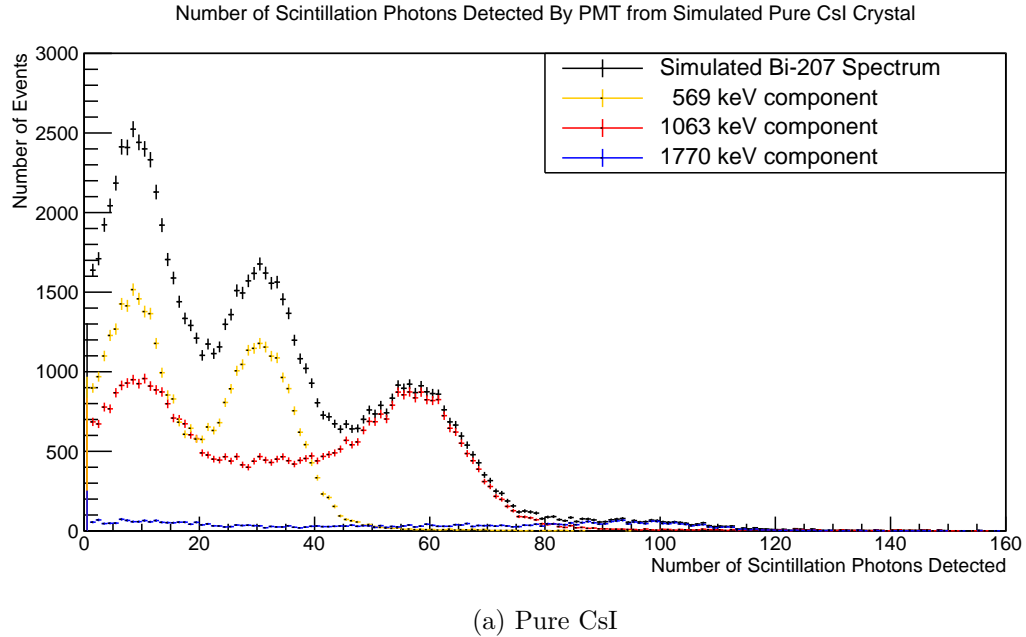


Figure 5.4: Simulated spectra of number of scintillation photons detected from a ^{207}Bi source for pure CsI and CsI(Tl) for absorption length of 40 cm.

5.1.1 Effect of Wrapping

All of the crystals studied in the lab were wrapped in reflective material to enhance their light collection efficiency. Using this simulation, the light yield for a wrapped and unwrapped pure CsI crystal was compared. A visual comparison of a scintillation

event for wrapped and unwrapped crystals is shown in Figure 5.5. The wrapping significantly reduces the amount of light that escapes the crystal.

Overlays of a ^{207}Bi spectrum for a wrapped and unwrapped crystal are shown in Figure 5.6a. The wrapping of the crystals increases the light detected at the PMT by about 30 %, improving the resolution of the detected spectrum. An overlay comparing calibrated energy spectra from measured and simulated data is shown in Figure 5.6b. The spectrum from the wrapped crystal is found to be in good agreement with measured data.

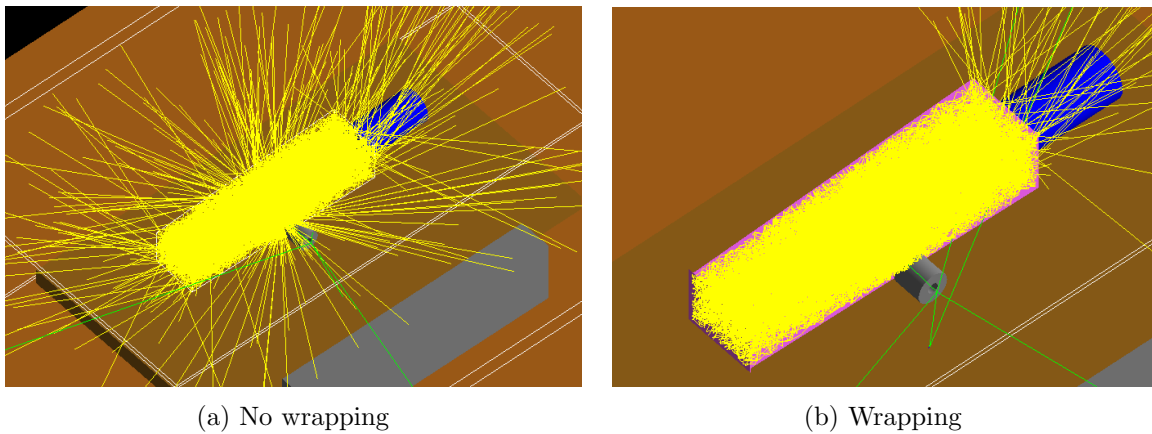


Figure 5.5: Visual comparison of unwrapped vs wrapped events.

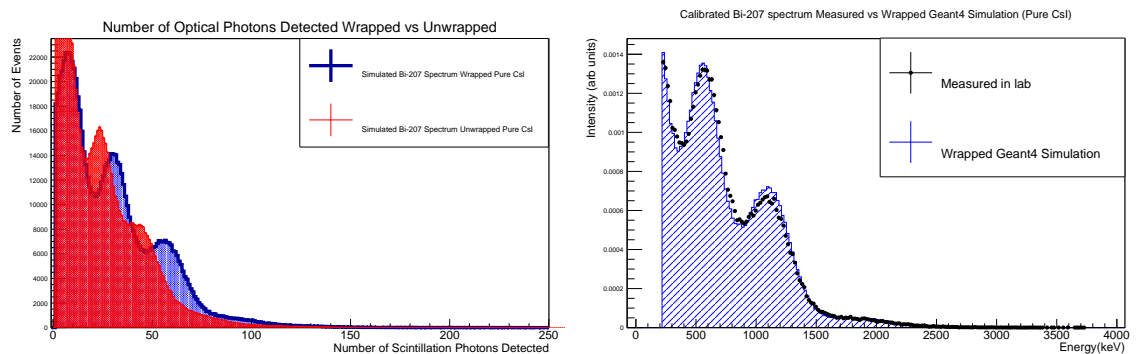


Figure 5.6: Simulated results comparing spectra from wrapped and unwrapped crystals.

5.1.2 Simulating Radiation Damage

As discussed in Chapter 3, radiation damage in CsI(Tl) originates through the creation of absorption centres in the crystal. By varying the absorption length of the scintillator in GEANT4, the dependence of scintillator performance on absorption length was studied. Uniformity plots for multiple absorption lengths for a pure CsI crystal are shown in Figure 5.7. The overall light yield and non-uniformity of the crystal was observed to change with absorption length.

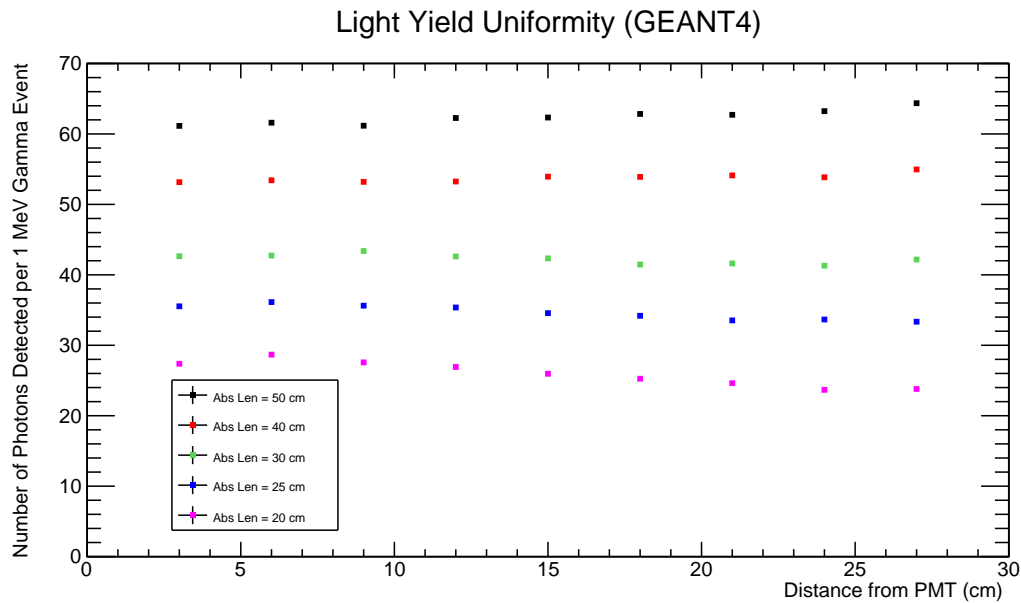


Figure 5.7: Geant4 simulated response longitudinally along crystal for different absorption lengths.

A plot of the average light yield as a function of the absorption length is shown in Figure 5.8. A smooth trend of decreasing light yield is found with decreasing absorption length, as expected. The light yield of the detector approaches two limits. As the absorption length increases, the light yield approaches an upper limit determined by the focusing geometry of the detector and as the absorption length decreases, the light yield decreases at an accelerated rate toward 0.

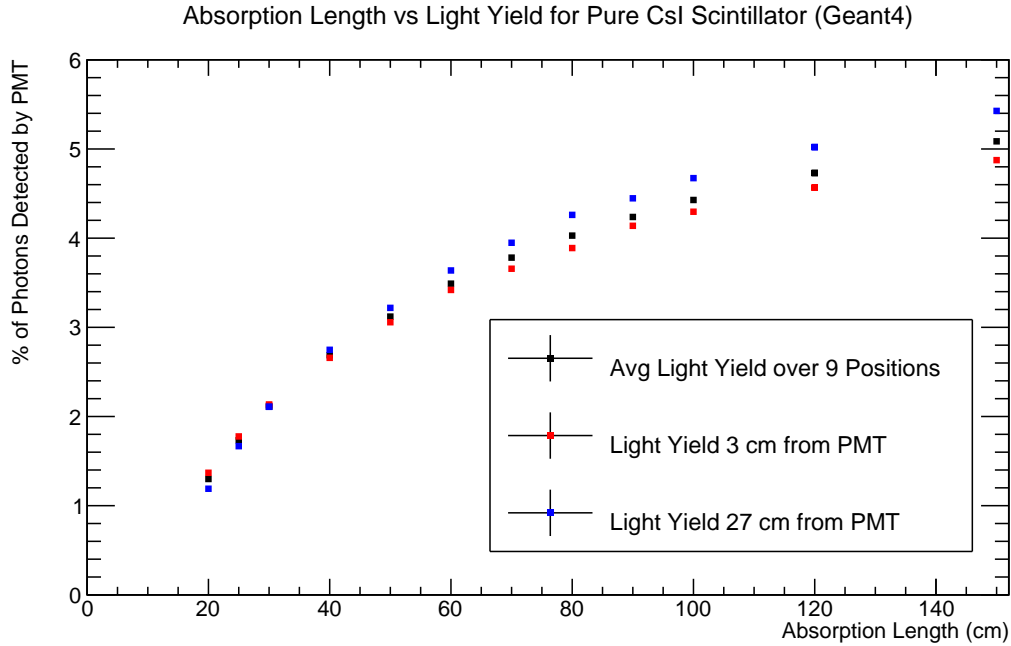


Figure 5.8: Simulated results of change in average light yield as a function of absorption length of crystal (pure CsI).

The uniformity of the crystal as a function of absorption length is shown in Figure 5.9. At very long absorption lengths, the non-uniformity of the crystal plateaus around 10%. At absorption lengths less than the length of the crystal, the non-uniformity rapidly begins to increase in the negative direction due to the response of the crystal far from the PMT rapidly degrading. This relationship between absorption length and non-uniformity has been studied for other crystals such as lead tungstate where a similar relationship was found [31].

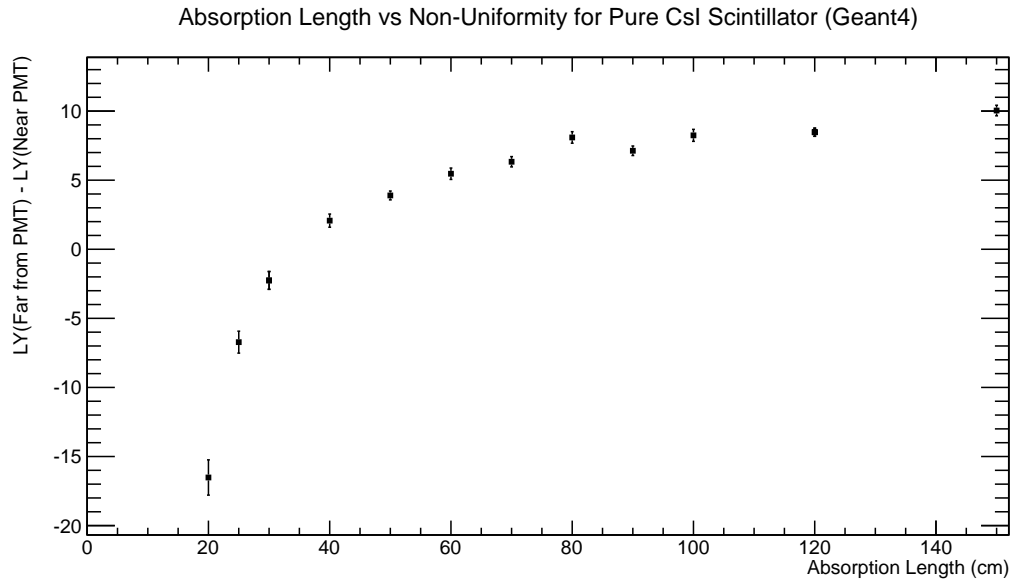


Figure 5.9: Simulated results of change in light yield uniformity as a function of absorption length of crystal.

5.2 Cosmic Apparatus Simulation

The cosmic ray test stand was simulated using GEANT4 and is shown in Figure 5.10 with many sample events.

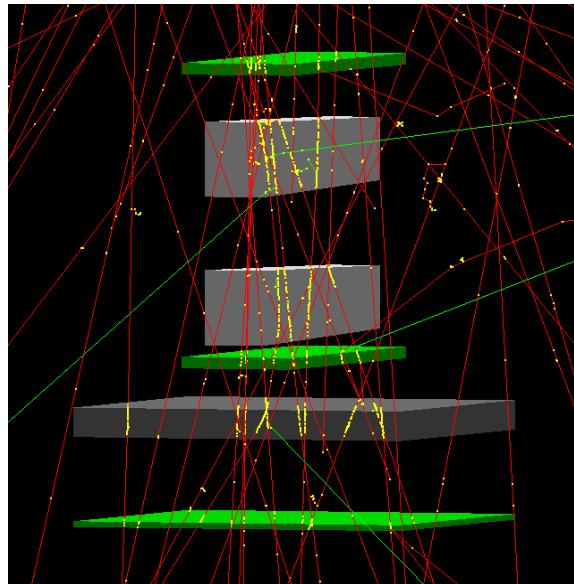
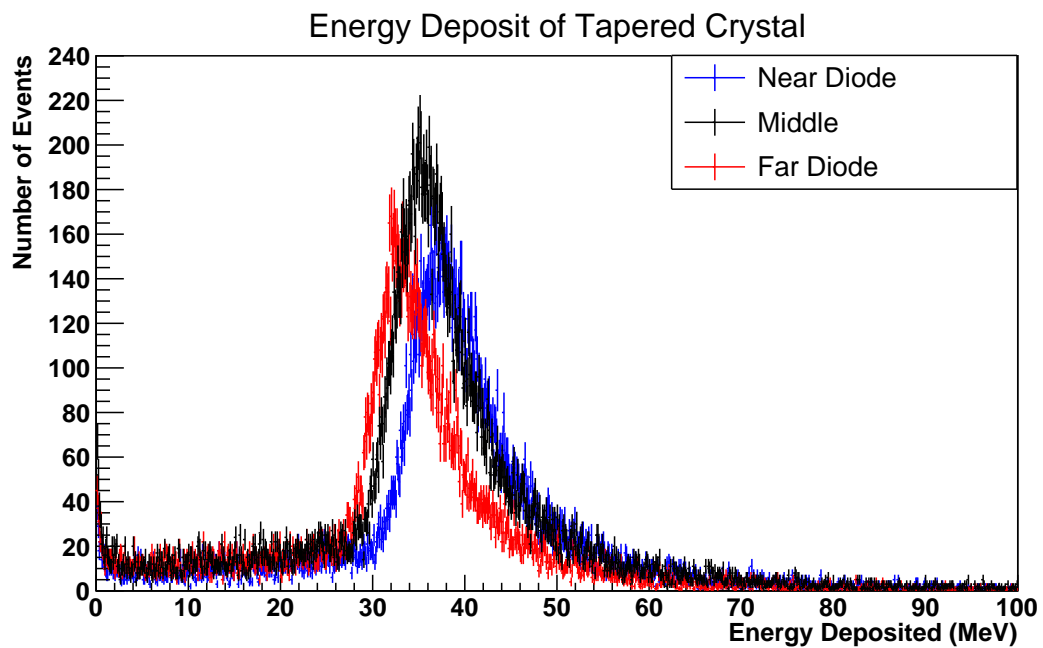


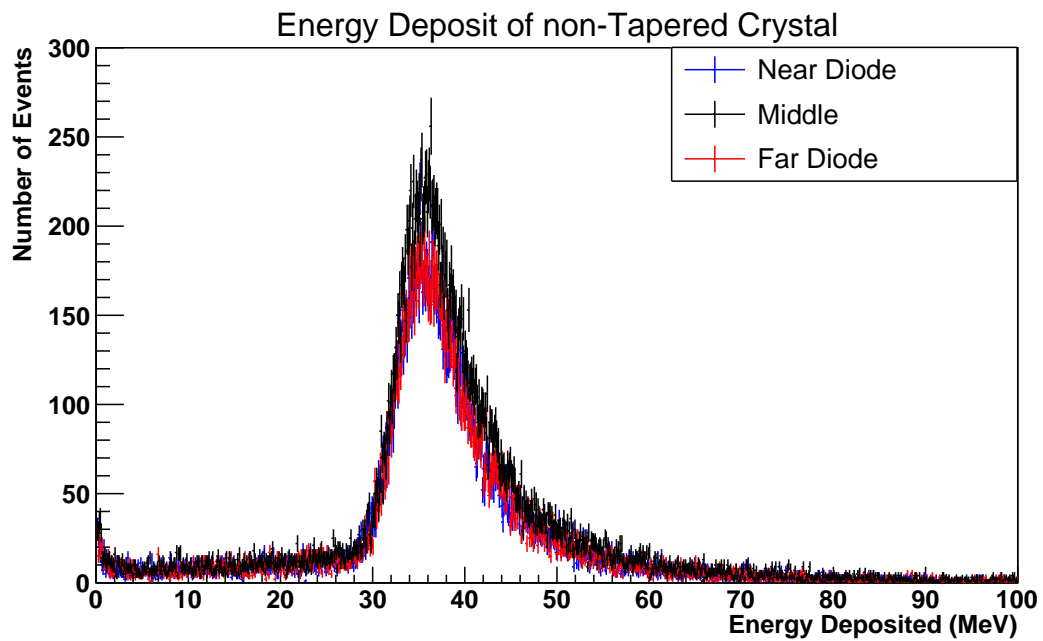
Figure 5.10: GEANT4 simulation of cosmic apparatus with many sample muon events (red tracks) passing through paddles and crystals.

Muons were used to simulate cosmic ray events. This approximation is valid as the cosmic apparatus global trigger requires coincidence from three vertically aligned trigger paddles. As the majority of other particles created from cosmic rays will lose energy much more quickly in a given material than muons, they will likely be filtered out by barriers such as the physics building, the CsI crystals and the lead plate prior to the last trigger. The energy spectrum of the muons was taken to be a uniform distribution between m_u and 10 GeV. According to the PDG, at sea level the mean energy of muons at ground level is ≈ 4 GeV with an approximately flat distribution below 1 GeV and a slow rise above 1 GeV [4]. The PDG also states that the angular distribution of cosmic rays at sea level is approximately proportional to $\cos^2 \theta$ thus this was the angular distribution used [4].

The Belle CsI(Tl) crystals tested using the cosmic test stand had a tapered geometry such that the readout face of the crystals (diode end) had a larger area than the front face of the crystal. As a result of this geometry, muons travelling through the diode end of the crystal traverse a greater path length and deposit a greater amount of energy compared to the same event at the front of the crystal. This effect is shown in Figure 5.11 where the simulated spectrum of energy deposited at the three longitudinal positions along the crystal are shown for a tapered and non-taper geometry.



(a) Tapered crystal.



(b) Non-tapered crystal.

Figure 5.11: GEANT4 simulation comparing longitudinal energy deposits for tapered and non-tapered crystals.

5.3 Resolution as a Function of Uniformity

In the case of large scintillation crystals, having a longitudinal non-uniform response can degrade the energy resolution of the crystal. As shown in Figure 5.9, increased absorption of scintillation light in the scintillator is expected to increase the non-uniformity of the crystal. The following simulation investigated how a non-uniform response along the length of the crystal degrades the energy resolution for photons in the energy range of 20 MeV to 10 GeV. To simulate these events, mono-energetic photons were sent into the front face of a CsI crystal and the energy deposited in the crystal was recorded. Figure 5.12 shows a sample event demonstrating the set-up.

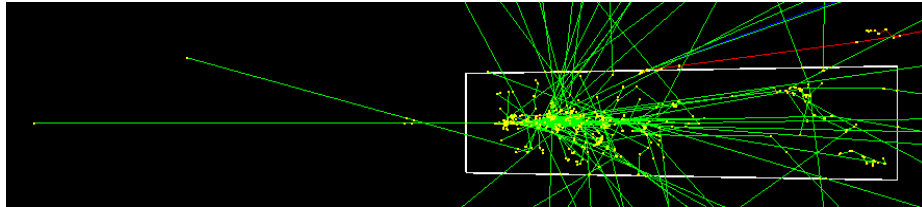


Figure 5.12: Simulated 500 MeV photon event in CsI.

To simulate non-uniformity in the crystal scintillation response, weights were applied to the recorded energy absorbed depending on the longitudinal location where the energy was deposited. This weighting method has been used before to study this effect on lead-tungstate crystals [32]. Figure 5.13 shows the weighting functions used. The weighting factor closest to the readout end was kept at 1.

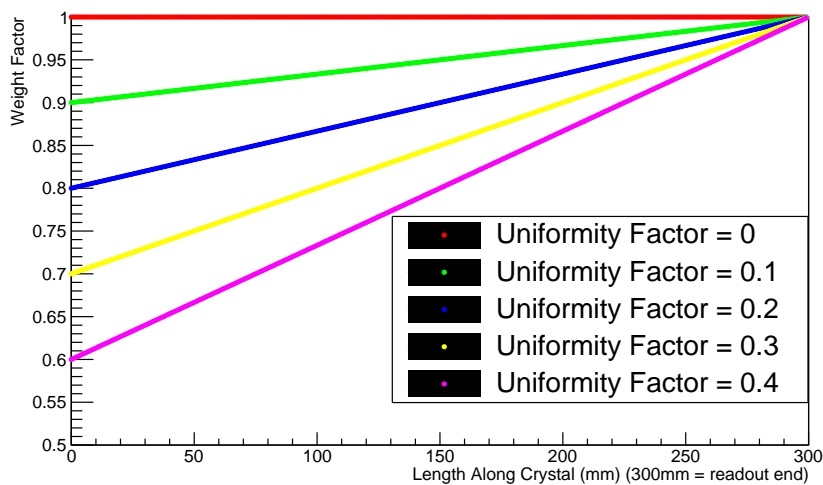
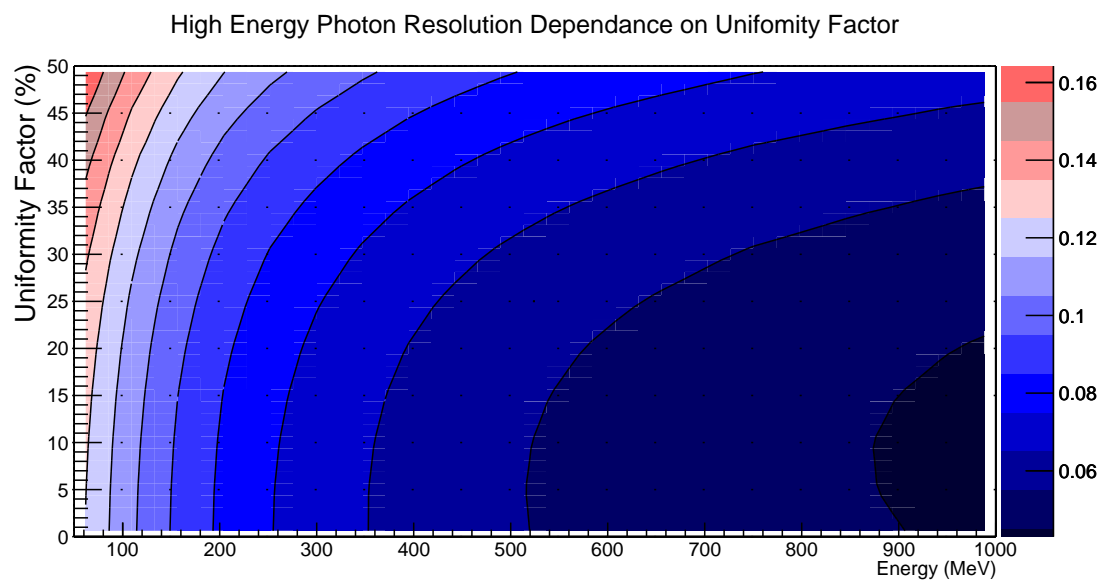


Figure 5.13: Weighting functions simulating non-uniform crystal response.

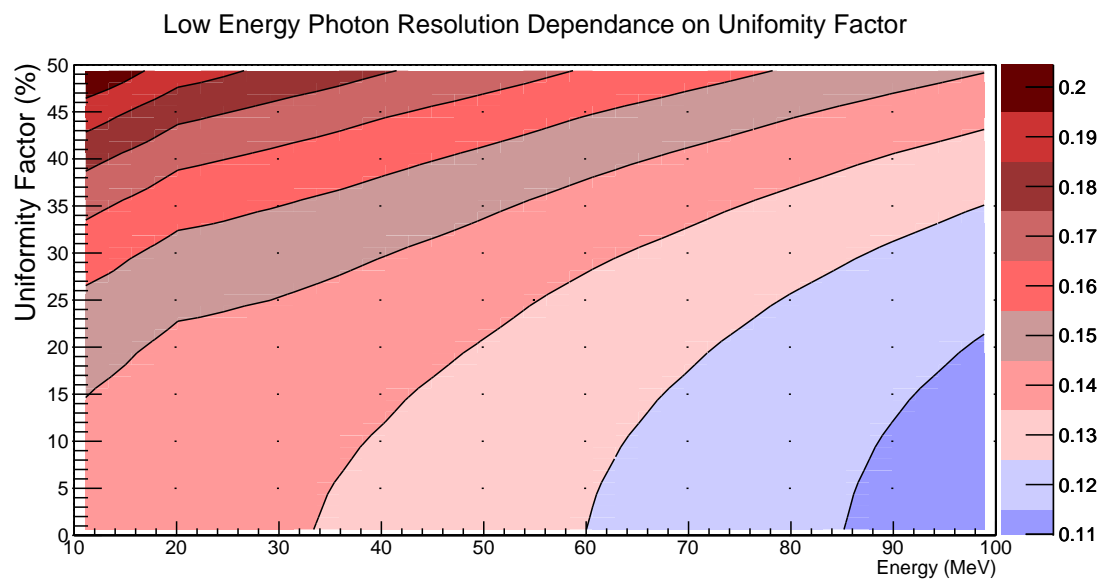
After recording an energy spectrum for many events the resolution of the spectrum was calculated using equation 5.1.

$$R = \frac{\sigma_{\text{spectrum}}}{E_{\text{spectrum}}^{\text{mean}}} \quad (5.1)$$

The results of the simulation are shown in Figure 5.14. The energy of the photons is shown on the horizontal axis and the uniformity factor is on the vertical axis. The resolution is given by the colour scale.



(a) High Energy



(b) Low Energy

Figure 5.14: Energy resolution (R plotted with color scale) dependence on crystal non-uniformity.

Chapter 6

Analysis Techniques

The techniques and procedures used to analyze the measured experimental data are described in this chapter. All errors presented are statistical errors. Note the sample-to-sample variations were much larger than any statistical and systematic errors present. Systematic errors were suppressed using ratios.

6.1 Light Yield Analysis

6.1.1 *BABAR* CsI(Tl) and pure CsI Light Yields

^{207}Bi Spectrum Analysis

For each uniformity measurement with the Uniformity Apparatus, ^{207}Bi spectra were acquired from nine positions spaced longitudinally along the crystal. The light yield of the crystal at each position is related to the channel number of the gamma peaks in the ^{207}Bi spectra.

In order to determine the peak channel numbers, fits were applied to the saved spectra. For CsI(Tl), the three ^{207}Bi gamma peaks were well defined and fit with Gaussian distributions. An sample spectrum fit is shown in Figure 6.1. Using the Gaussian fits, the mean and σ of each peak was obtained.

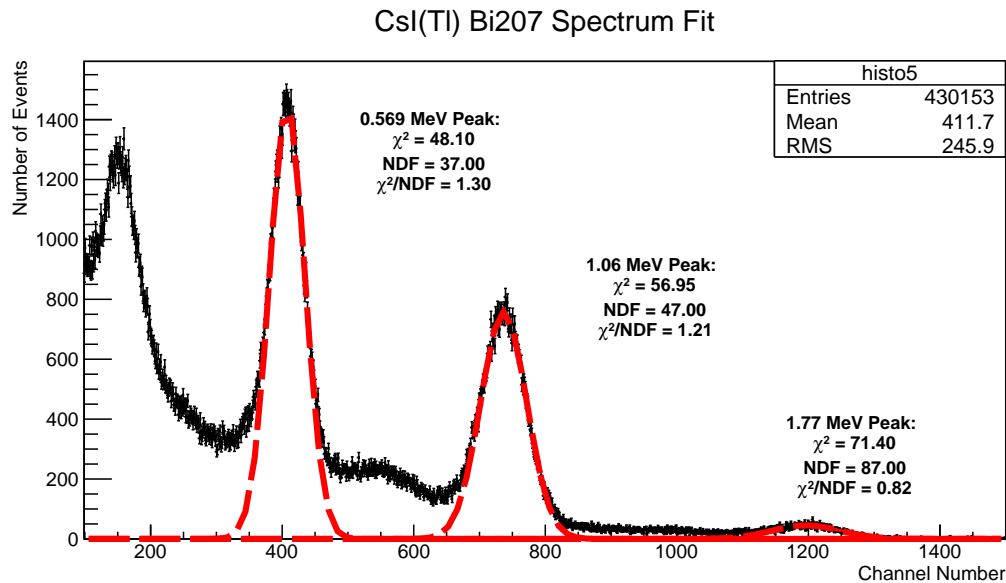


Figure 6.1: Fits used to calculate ^{207}Bi peak parameters for CsI(Tl) measurements.

For the pure CsI crystal, the poor light yield of the crystal resulted in the ^{207}Bi gamma peaks to not be well separated and a more complicated fit had to be implemented. Motivated by the results of the GEANT4 simulation shown in Figure 5.4a, the 1.066 MeV peak was fit using a Crystal Ball Function¹. The tail of the Crystal Ball Function was used to model the Compton continuum of this peak. This continuum slightly offsets the channel number of the 0.569 MeV peak and as a result, this fitting method was required to accurately determine the relative location of the 0.569 MeV peak. The 0.569 MeV peak, 1.77 MeV peak and the backscatter rise were fit with Gaussian distributions. Using this combination of functions the entire ^{207}Bi spectrum was fit. Figure 6.2 shows a sample fit for pure CsI.

¹The Crystal Ball Function consists of a Gaussian distribution with a polynomial tail.

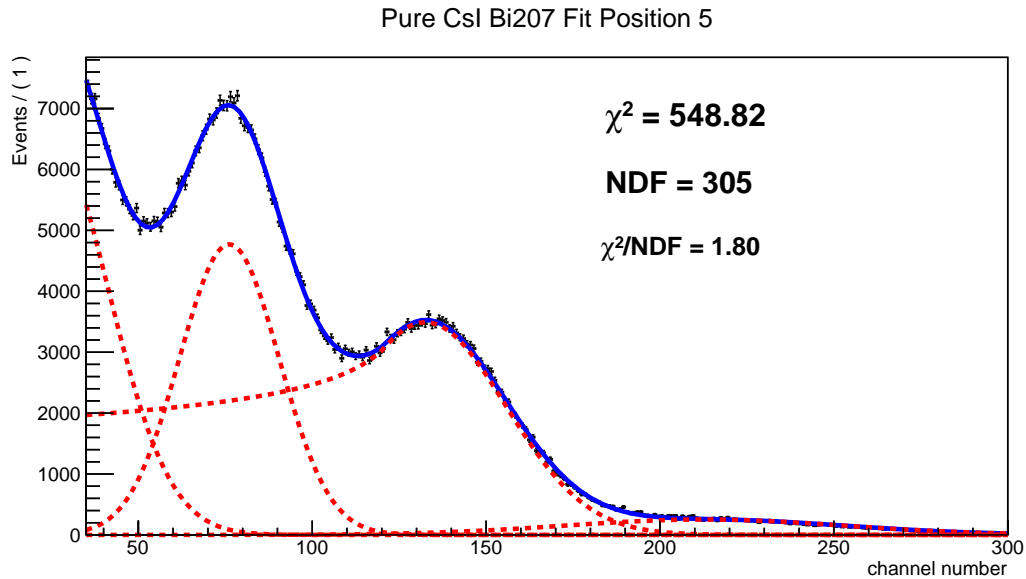


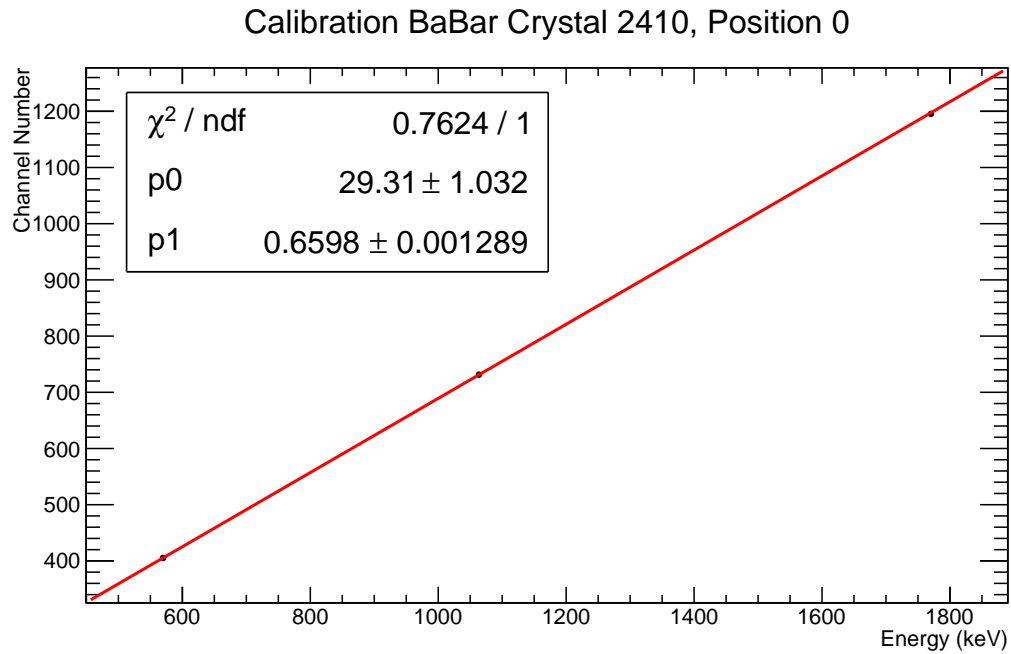
Figure 6.2: Fits used to calculate ^{207}Bi peak parameters for pure CsI measurements.

Pedestal Calculation

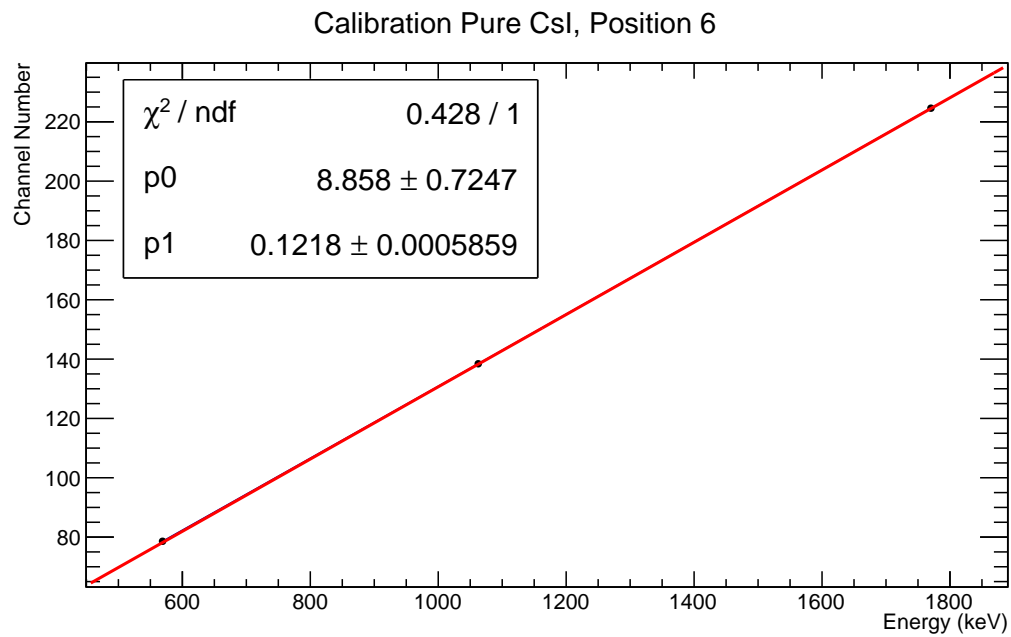
The peak channel numbers calculated from the above fits are related to the scintillation light yield, L_0 , by equation 6.1.

$$\text{Peak Ch \#} = E_\gamma L_0 + P \quad (6.1)$$

E_γ is the energy of the incoming gamma ray and P is the noise pedestal that shifts the spectrum. The pedestal was calculated by generating a Calibration Plot of Peak Channel Number vs Energy for each spectra. Using a first order polynomial, the Calibration Plot was fit and the pedestal was determined by the channel number corresponding to 0 keV. The pedestals of all positions in a uniformity measurement were consistently found to be similar and an average was taken to determine the pedestal of the uniformity measurement. Figure 6.3a and 6.3b shows typical Calibration Plot's for pure CsI and CsI(Tl) respectively. The linear calibration fits are also shown.



(a) CsI(Tl)



(b) Pure CsI

Figure 6.3: Sample calibrations plots for CsI(Tl) and pure CsI

The light yield of each peak, LY_{peak} , was defined by equation 6.2. Using this definition, LY_{peak} is directly proportional to the scintillation response of the crystal.

$$\text{LY}_{\text{peak}} = \text{Peak Ch \#} - P_{\text{avg}} \quad (6.2)$$

In order to characterize the overall light yield of the crystal, the average of the nine position light yield measurements, $\text{LY}_{\text{peak}}^{\text{avg}}$, was used.

Energy Resolution

The energy resolution, R_E , of each peak in the ^{207}Bi spectrum was calculated by equation 6.3

$$R_E = \frac{\sigma_{\text{peak}}}{\text{LY}_{\text{peak}}} \quad (6.3)$$

where σ_{peak} is standard deviation of the Gaussian function used to fit the peak.

Light Yield Non-Uniformity

The light yield non-uniformity, Δ_{LY} , describes the front-to-back change in scintillation response longitudinally along the crystal. In order to calculate Δ_{LY} , first the normalized response of the crystal as a function of distance from the PMT, $\text{LY}_{\text{norm}}(x)$, was calculated using equation 6.4.

$$\text{LY}_{\text{norm}}(x) = \frac{1}{2} \left(\frac{\text{LY}_{569}(x)}{\text{LY}_{569}^{\text{avg}}} + \frac{\text{LY}_{1066}(x)}{\text{LY}_{1066}^{\text{avg}}} \right) \quad (6.4)$$

Figure 6.4 shows a sample plot of $\text{LY}_{\text{norm}}(x)$.

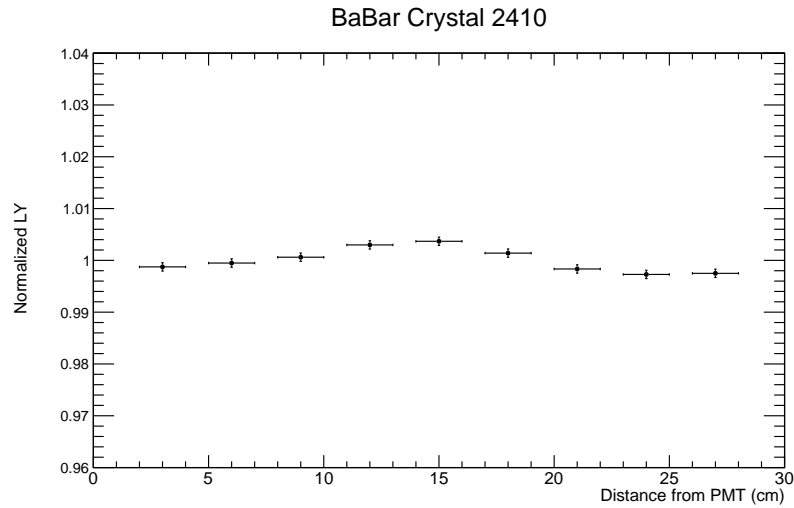


Figure 6.4: Sample uniformity plot.

The front-to-back non-uniformity of the crystal was calculated using equation 6.5.

$$\Delta_{LY} = LY_{\text{norm}}(27 \text{ cm}) - LY_{\text{norm}}(3 \text{ cm}) \quad (6.5)$$

Radiation Dose Stage Light Yield

The stability of the PMT and electronics, during the radiation hardness studies, was monitored with the undosed reference crystal, BCAL2410. Each day where light yield measurements were done, the reference crystal was first measured to ensure day to day consistency. Figure 6.5 shows $LY_{\text{peak}}^{\text{avg}}$ of the three ^{207}Bi peaks for the reference crystal for the duration of the study.

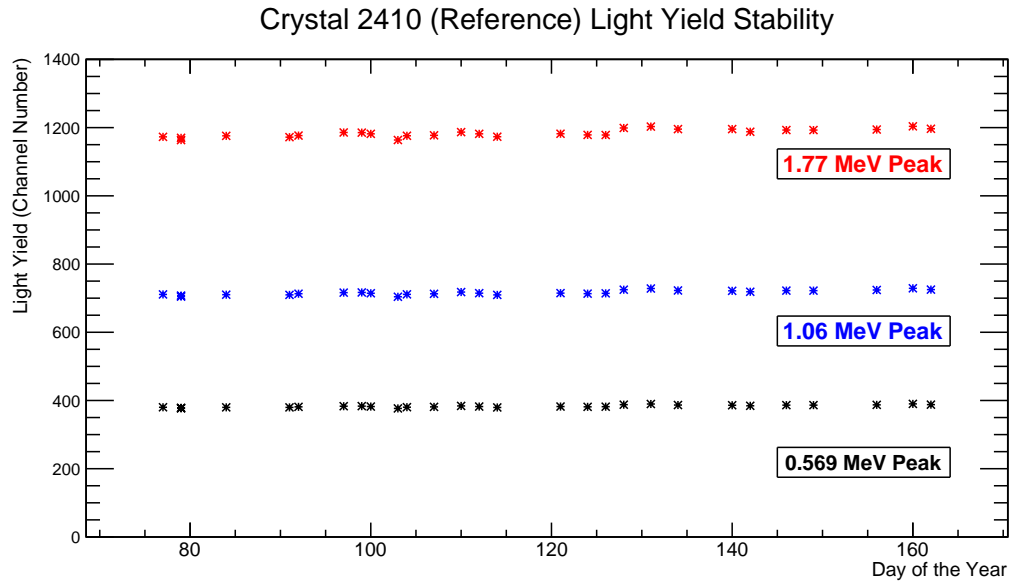


Figure 6.5: Stability of reference crystal throughout study. Statistical error bars are smaller than the points.

At each dosing stage, multiple uniformity measurements were done on different days in order to monitor for any recovery in the light yield. Short term recovery lasting up to 48 hours after irradiation has been observed in previous studies of CsI(Tl) radiation hardness and has been attributed to the decreasing intensity of phosphorescence which becomes present after irradiation [17, 33]. No recovery was observed in this study. However, measurements began a minimum 2 days after irradiation thus any short term recovery within 48 hrs of irradiation was not monitored. Figures 6.6 - 6.8 show plots of $LY_{\text{peak}}^{\text{avg}}$ as a function of day of the year for several irradiated *BABAR* crystals. The vertically dashed line in each plot indicates the day the crystal was dosed.

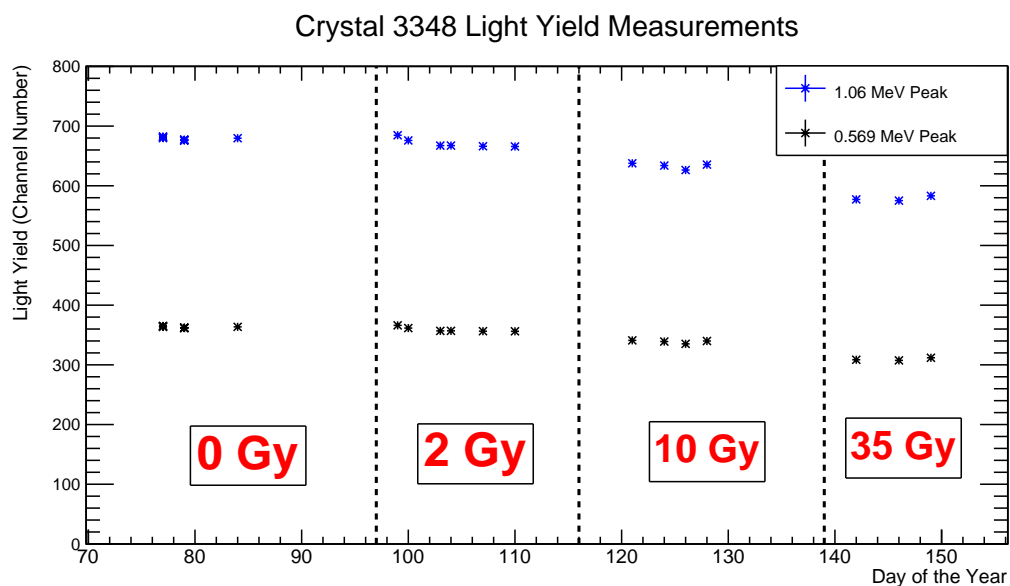


Figure 6.6: Crystal 3348 $LY_{\text{peak}}^{\text{avg}}$ measurements

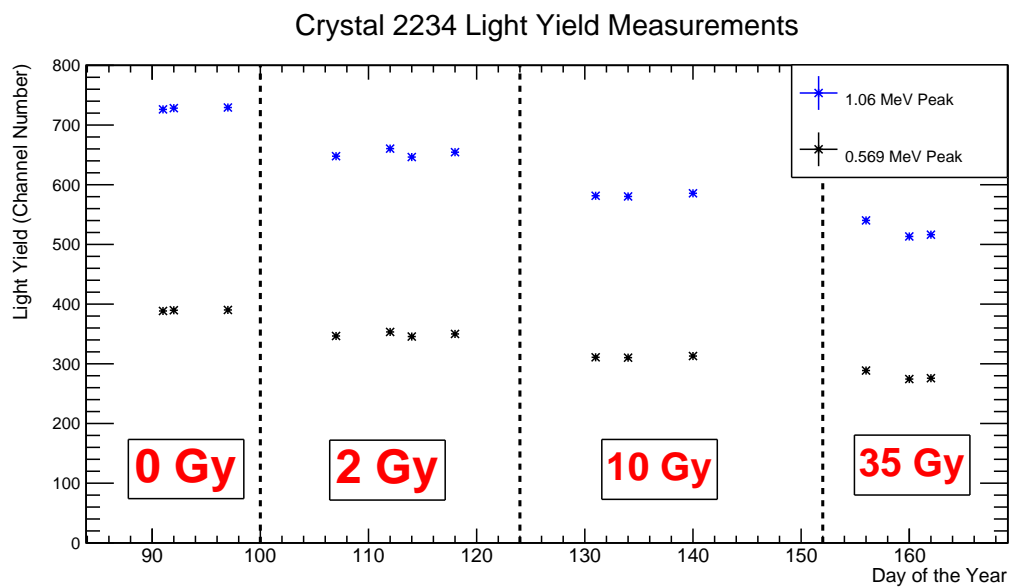


Figure 6.7: Crystal 2234 $LY_{\text{peak}}^{\text{avg}}$ measurements.

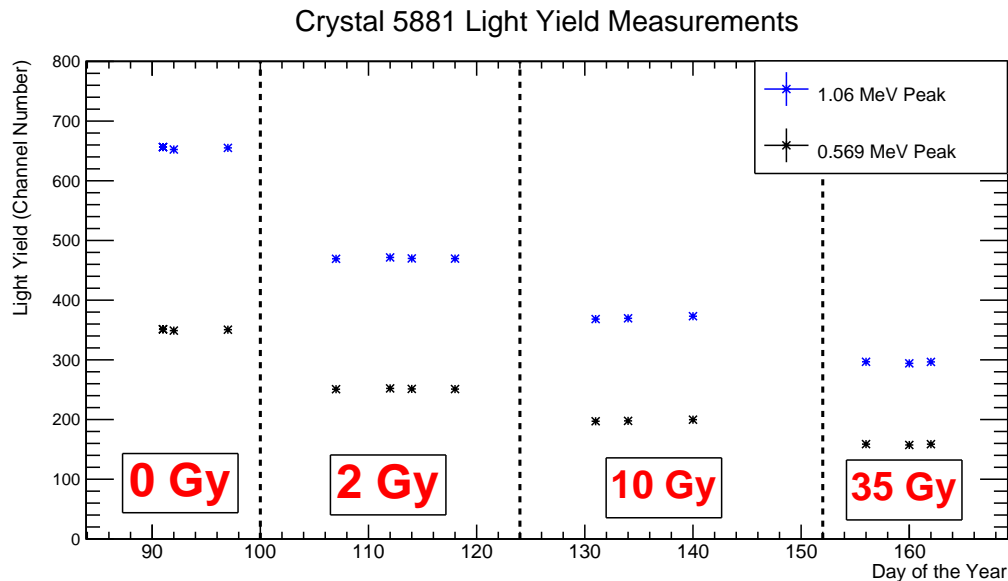


Figure 6.8: Crystal 5881 $LY_{\text{peak}}^{\text{avg}}$ measurements.

The light yield of the crystals at each dosing stage, LY_{Dose} was calculated from the average of all measurements done during that dosing stage. Using LY_{Dose} , the percent light yield of each dosing stage, $LY_{\%}$, was calculated from equation 6.6. Due to the low intensity of the 1.77 MeV gamma peak, only the 0.569 Mev and 1.06 Mev gamma peaks of the ^{207}Bi spectra were used.

$$LY_{\%}(D) = \frac{1}{2} \left[\frac{LY_{\text{Dose}}^{569}(D)}{LY_{\text{Dose}}^{569}(0 \text{ Gy})} + \frac{LY_{\text{Dose}}^{1066}(D)}{LY_{\text{Dose}}^{1066}(0 \text{ Gy})} \right] \quad (6.6)$$

6.1.2 Belle Crystal Light Yields

Summed Diode Analysis

As described in Chapter 4, the light yield of the Belle crystals was measured using the Cosmic Ray Apparatus. For each coincidence event, the shaped diode pulses were summed then digitized and saved along with the trigger location information. As the pre-amp integrated the charge signal from the diodes, the pulse height for each pre-amp pulse is related to the light yield of that event and was calculated using equation 6.7.

$$V_{\text{Pulse}} = V_{\text{max}} - V_{\text{pretrigger avg}} \quad (6.7)$$

A Pulse Height Histogram (PHH) was made for each of the three trigger positions along the crystal from each cosmic run. Figure 6.9, shows a sample PHH from a signal cosmic run where cosmic were continuously acquired for several days. The simulated version of this histogram for a crystal of similar size is shown in Figure 6.10 displaying the corresponding scale of the energy deposits.

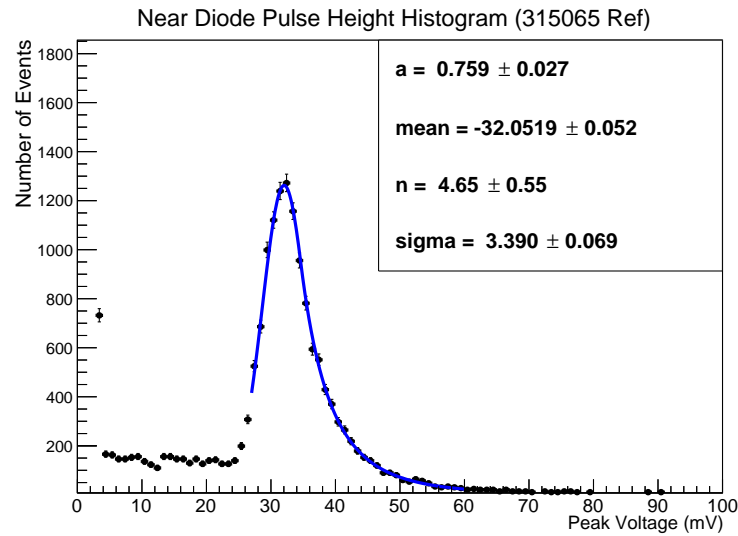


Figure 6.9: Measured Pulse Height Histogram with Belle Crystal. Crystal Ball Function fit is also shown.

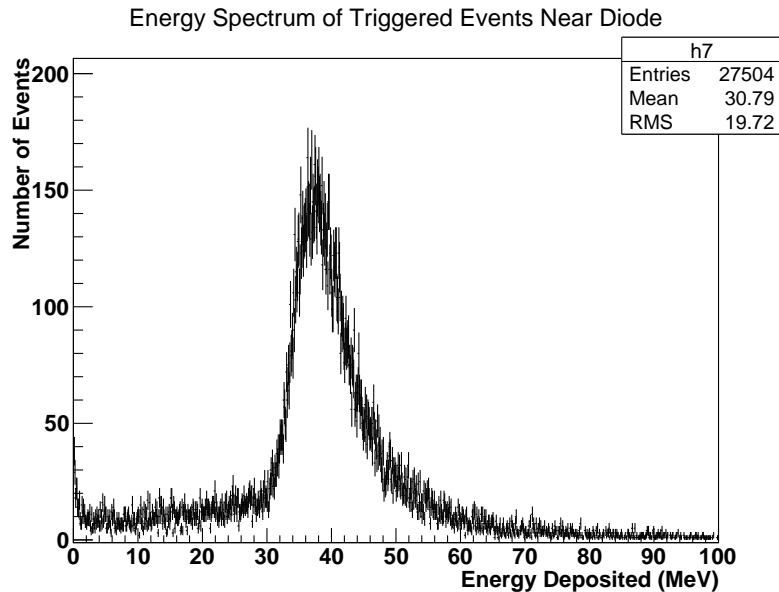


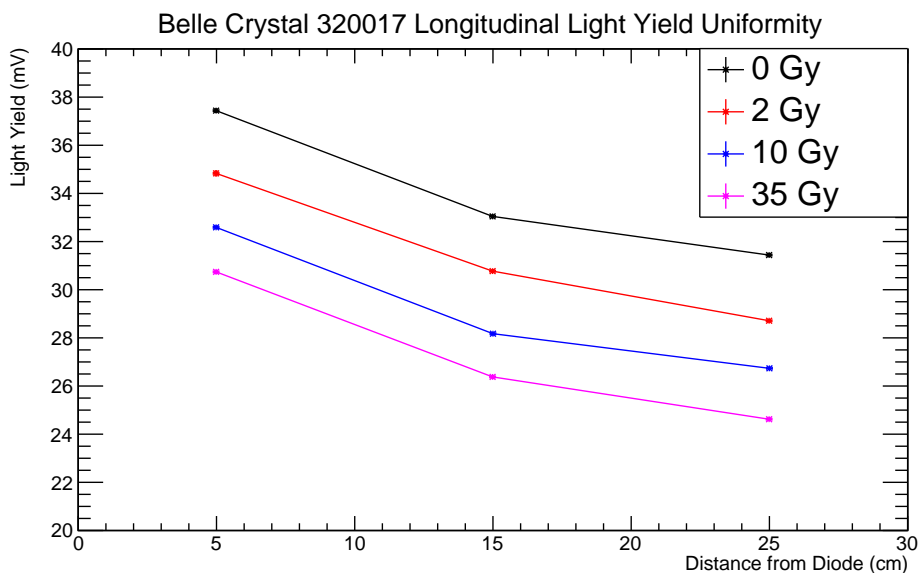
Figure 6.10: GEANT4 simulation of muon energy deposits using Cosmic Ray Apparatus.

The pulse height distributions were fit using a Crystal Ball Function shown in Figure 6.9. The mean of the Crystal Ball Function was used to quantify the light yield of the crystal. Note this mean corresponds to the mean of the Gaussian component of the Crystal Ball Function not the mean of the distribution. The overall light yield, LY, was calculated from the average of the Near Diode, Middle and Far Diode light yields. Multiple measurements each lasting 1-4 days were made at each dosing stage to monitor for recovery. As with the *BABAR* crystals, no recovery was observed. The light yield of each dosing stage was calculated from the average of all measurements at each dosing stage.

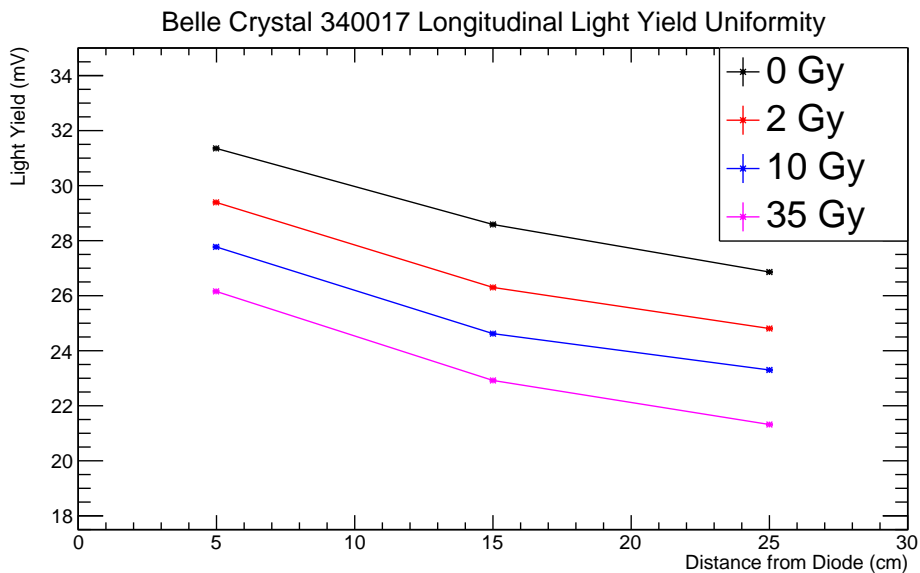
Belle Crystal Non-Uniformity

As described in Chapter 4 and in the Appendix, the trigger logic of the Cosmic Ray Apparatus allows for the longitudinal location of the muon deposited to be determined. Plots of the the light yield as a function of longitudinal position are shown in Figure 6.11a and 6.11b for both Belle crystals at all dosing stages. As demonstrated in Chapter 5, a large component of the non-uniformity in the above plots is due to the taper of the crystals. The change in light yield at each dosing stage was calculated using equation 6.8.

$$LY(x, D) = \frac{LY(x, D)}{LY(x, 0 \text{ Gy})} \quad (6.8)$$



(a) Belle Crystal 320017



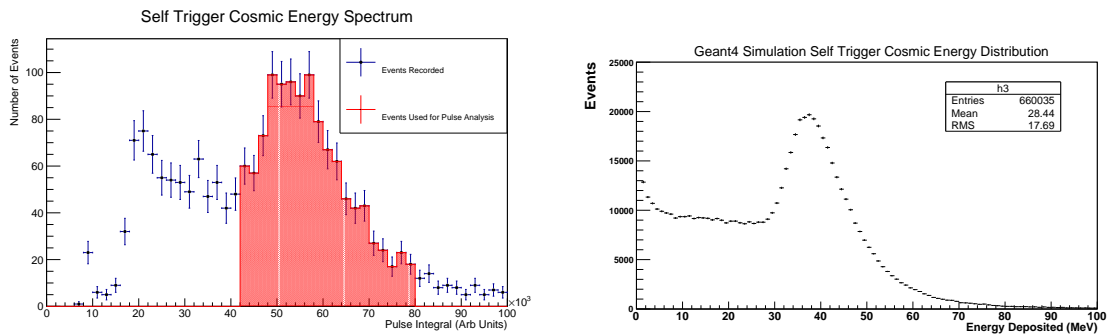
(b) Belle Crystal 334017

Figure 6.11: Belle Crystal non-uniformities at all dosing stages.

6.2 Scintillation Decay Time and Time Resolution

Scintillation Decay Time

Using cosmic rays, the scintillation decay times of the *BABAR* CsI(Tl) crystals and pure CsI crystal was measured. For the *BABAR* crystals, the pulses were recorded using self-triggering. This resulted in the recorded energy distribution shown in Figure 6.12a. The simulated version of this distribution is shown in Figure 6.12b. In order to restrict the pulse analysis to events where a muon had likely passed through the full thickness of the crystal, an energy cut was made and is highlighted in Figure 6.12a.



(a) Energy cut made for cosmic analysis corresponds to 35-45 MeV energy deposits. (b) GEANT4 simulation results of self-triggered energy distribution.

Figure 6.12: Comparison of measured and simulated energy spectrum for self-triggered cosmics.

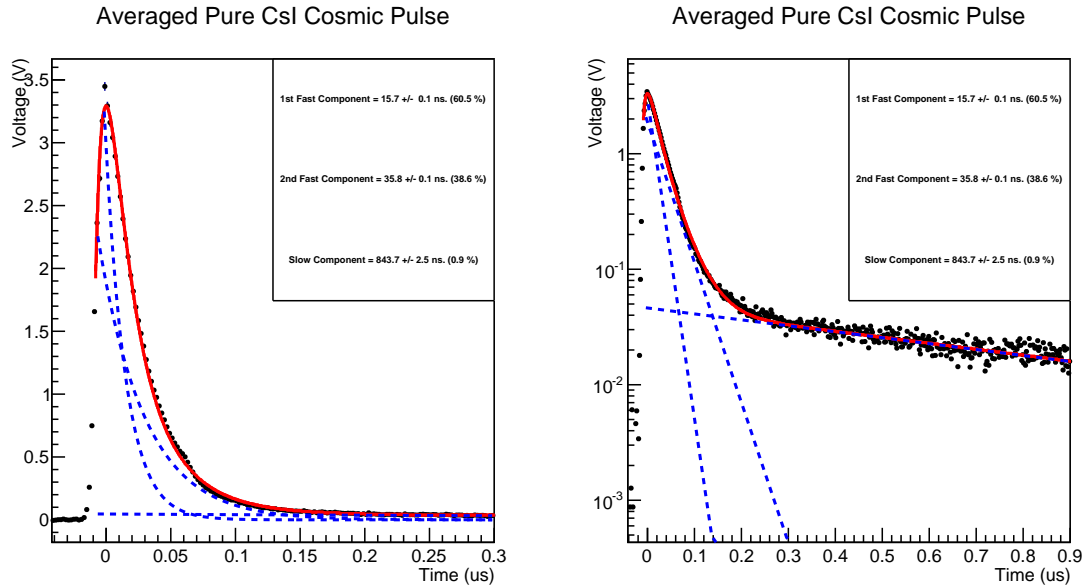
Each individual scintillation pulse was subject to statistical fluctuations from photo-electron statistics and electronic noise as shown in Figure 4.6. To reduce the statistical error, pulses in the energy cut range were first normalized then averaged to make an averaged pulse. The averaged pulse was inverted and used for scintillation time analysis.

In order to determine the decay time of the scintillation components, a fit was performed using equation 6.9 for the pure CsI and equation 6.10 for CsI(Tl). These fits were motivated from previous studies of these crystals where multiple scintillation components were found [14, 17, 34].

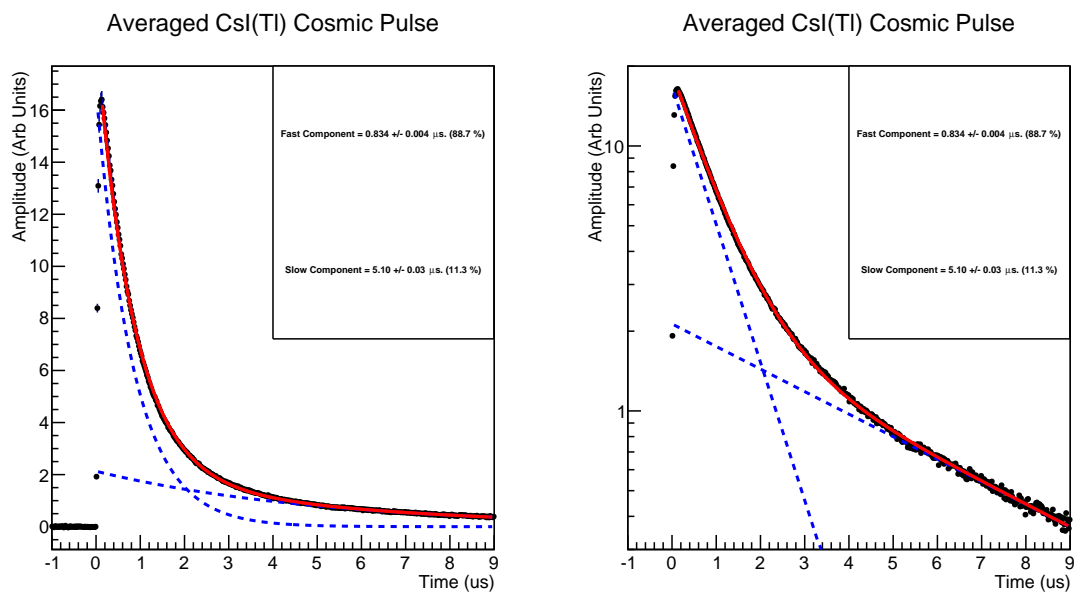
$$V_{\text{CsI}}(t) = -A_0 e^{-\frac{t}{\tau_{\text{pmt}}}} + A_1 e^{-\frac{t}{\tau_{\text{fast 1}}}} + A_2 e^{-\frac{t}{\tau_{\text{fast 2}}}} + A_3 e^{-\frac{t}{\tau_{\text{slow}}}} \quad (6.9)$$

$$V_{\text{CsI(Tl)}}(t) = -A_0 e^{-\frac{t}{\tau_{\text{pmt}}}} + A_1 e^{-\frac{t}{\tau_{\text{fast}}}} + A_2 e^{-\frac{t}{\tau_{\text{slow}}}} \quad (6.10)$$

The first term in the equations 6.9 and 6.10 represents the rise time of the PMT and any parasitic capacitance in the signal chain [35]. The remaining exponential terms are for various decay times present in each crystal. Figure 6.13 shows the fit results for pure CsI and CsI(Tl) with the scintillation components also shown. The left plot is normal scale and the right plot shows the fit on a vertical log scale where the slow component is more visible. The typical time constants found in CsI(Tl) pulse were $0.834 \pm 0.004 \mu\text{s}$ and $5.10 \pm 0.03 \mu\text{s}$ and for the pure CsI the typical fits were $15.7 \pm 0.1 \text{ ns}$, $35.8 \pm 0.1 \text{ ns}$ and $843.7 \pm 2.5 \text{ ns}$.



(a) pure CsI



(b) CsI(Tl)

Figure 6.13: Fits to scintillation pulses used to measured scintillation decay time components. Note the time scales are different for the two pulses.

Time Resolution

The time resolution for the Belle crystals was measured by operating the UVic readout board in individual diode readout mode such that both shaped diode pulses were

digitized and saved. The time resolution of the diodes was calculated using the following procedure. For each pulse, any DC offset was removed by subtracting an average of the pre trigger noise. Then t_{25} , defined in equation 6.11, was calculated. As the rising edge of the pre-amp pulse is calculated from an integral of the scintillation pulse, t_{25} gives the time when 25 % of the charge from the PMT was integrated.

$$\frac{V_{\text{preamp}}(t_{25})}{V_{\text{preamp}}^{\text{max}}} = 0.25 \quad (6.11)$$

A histogram of $t_{25}^{\text{Diode 1}} - t_{25}^{\text{Diode 2}}$ for all events was made giving the distribution for time fluctuations between the two diodes. Figure 6.14 shows one of these histograms.

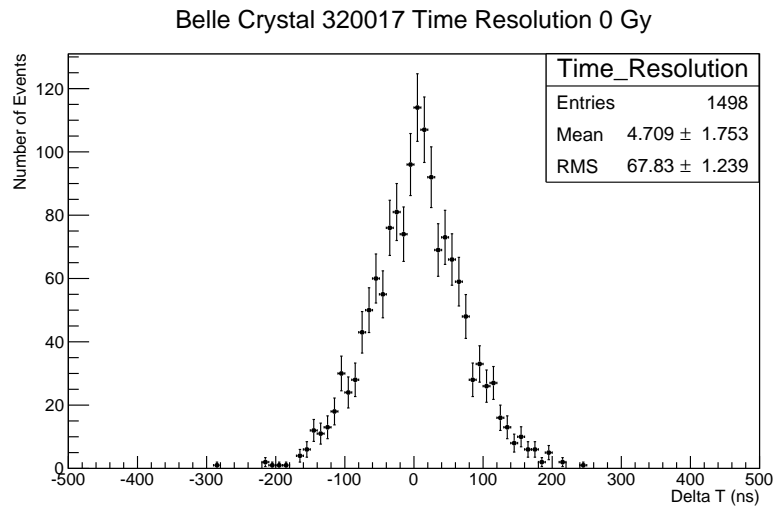


Figure 6.14: Belle Crystal 320017 time resolution histogram at 0 Gy. Note ΔT was calculated at 25 % of the pulse rise time.

The time resolution, σ_{Diode} , is related to the width of this histogram. Although the distribution is symmetric, it was found to not be Gaussian and thus the standard deviation (labelled RMS) of the distribution was used to characterize the width of the distribution. The final step in calculating the time resolution is to account for the fact that both diodes were used independently to measure this time resolution. That is,

$$\sigma_{\text{RMS}}^2 = \sigma_{\text{D1}}^2 + \sigma_{\text{D2}}^2 \quad (6.12)$$

Assuming $\sigma_{\text{D1}} = \sigma_{\text{D2}} = \sigma_{\text{Diode}}$ then the time resolution is given equation 6.13.

$$\sigma_{\text{Diode}} = \frac{\sigma_{\text{RMS}}}{\sqrt{2}} \quad (6.13)$$

For the pure CsI crystal, PMT readout was used and thus the calculation of the time resolution followed a different procedure. When recording cosmics with the pure CsI crystal an external trigger was used to trigger on comics passing through the crystal. The external triggering system used was composed of plastic scintillators with extremely short scintillation times and any time variations from the trigger could be ignored. As a result, a histogram of t_{25} would show the time fluctuations from the detector. For the pure CsI crystal, t_{25} was defined by equation 6.14.

$$\frac{\int_0^{t_{25}} V_{\text{PMT}}(t) dt}{\int_0^{900\text{ns}} V_{\text{PMT}}(t) dt} = 0.25 \quad (6.14)$$

This definition of t_{25} gives the time when the scintillation pulse, $V(t)$, reaches 25% charge. A histogram of t_{25} for pure CsI is shown in Figure 6.15.

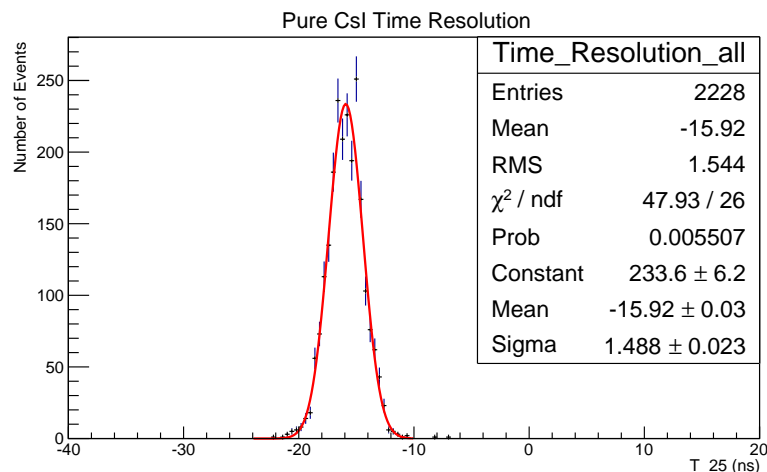


Figure 6.15: Pure CsI time resolution histogram.

A Gaussian fit was used to calculate the width of the distribution. In this case the width of the Gaussian is equal to the time resolution for the 40 MeV deposit.

Chapter 7

Results and Discussion

7.1 Comparison of Pure CsI and CsI(Tl)

The measured values for the scintillation properties of the CsI(Tl) and pure CsI crystals studied are summarized in Table 7.1.

Table 7.1: Measured scintillation properties of CsI(Tl) and pure CsI at 0 Gy.

Scintillator	R_E @ 1 MeV	τ_{fast}	τ_{slow}	σ_τ
CsI(Tl)	5%	834 ± 4 ns (88.7%)	5100 ± 30 ns (11.3%)	47.9 ± 0.9 ns (20 MeV)
Pure CsI	18%	15.7 ± 0.1 ns (60.5%) 35.8 ± 0.1 ns (38.6%)	843.7 ± 2.5 ns (0.9%)	1.49 ± 0.02 ns (40 MeV)

Energy Resolution

Using a PMT and air as the optical coupling, the energy resolution at 1 MeV was measured to be 5% for CsI(Tl) and 18% for pure CsI. This measurement demonstrates the high light yield of CsI(Tl) compared to pure CsI and was confirmed by the simulations shown in Chapter 5. The energy resolution of pure CsI with PMT readout however was found to be better than the CsI(Tl) with PIN diode readout at 1 MeV. This is expected as the diodes have a much smaller area compared to the PMT and have no internal gain. The diodes are used in the Belle ECL as they have a practical advantages over the PMT as they are much smaller and unaffected by

magnetic fields [2, 12]. The Belle ECL is also concerned with energy measurements much greater than 1 MeV where there is sufficient scintillation light and high gain is not required. If an upgrade to pure CsI is done however, the measurements of R_E above show that a high gain light detector such as a PMT would have to be used with the pure CsI in order to achieve the same or better energy resolution performance of the CsI(Tl) with PIN diode readout.

Timing Resolution

The scintillation times for CsI(Tl) were confirmed to be significantly larger than pure CsI. The fast scintillation time of pure CsI results in a superior time resolution compared to the current Belle ECL detectors. The measured values of the time resolution can be compared to studies presented in the Belle II Technical Design Report (TDR). The TDR states that for a 15-20 MeV energies, the time resolution in Belle was measured to be approximately 35-40 ns [2]. This is slightly better than the measurements shown above likely do to the additional pulse shaping and crystal clustering used in the Belle ECL. For the pure CsI, photon beam studies have measured the time resolution at 40 MeV to be about 0.8 ns [2]. The time resolution measured in this study is close to this value and the discrepancy likely a result of the poor optical coupling used between the PMT and crystal.

7.2 Radiation Hardness Results

The radiation hardness of the scintillation properties of CsI(Tl) were studied at the accumulated doses outlined in Table 7.2. Each dosing stage was designed to give the most useful information for Belle II. Table 7.2 states the nominal value of each dose stage. The exact doses for each crystal at each stage are listed in Appendix A.3.

Table 7.2: Nominal values for the accumulated doses where scintillation properties of CsI(Tl) were measured. 1 Gy = 100 rad.

Dose (Gy)	Comment
2	Belle 10 Year Dose
10	Belle II 10 year dose for crystals in ECL barrel [9]
35	Belle II 10 year dose for crystals in ECL endcaps [9]

Light Yield

The light yield for all crystals as a function of absorbed dose is shown in Figure 7.1. Appendix A.3 lists the percent light yield values for all crystals at each dosing stage.

All crystals at 0 Gy began with similar light yields however the magnitude of the overall light loss varied across the entire sample set of crystals with the maximum light loss being over 50% at 35 Gy. At 2 Gy, the two Belle crystals had dropped to about 92% of their original light yield. This result is in agreement with the light drop observed in the Belle ECL after 10 years of operation corresponding to accumulated doses of 2 Gy [2]. This comparison is important as it suggests the doses from ^{60}Co used for this study are equivalent to the doses received during operation. At 10 Gy, several crystals maintained over 90 % of their original light yield with one *BABAR* crystal showing very good radiation hardness with no change from 2 Gy to 10 Gy. At an absorbed dose of 35 Gy, all crystals were observed to have some degradation in light yield.

Crystals from the same manufacturer demonstrated similar radiation hardness. This observation suggests that the radiation hardness of the crystals is a result of their growth process and is useful for Belle II calorimeter as it suggests that the results can be extrapolated to other Belle crystals. The light loss as a function of dose was found to follow a non-linear trend. For the majority of the crystals, the largest relative light drop was at a dose of 2 Gy. At higher doses, the light loss began to plateau. This trend was found to be independent of the readout method.

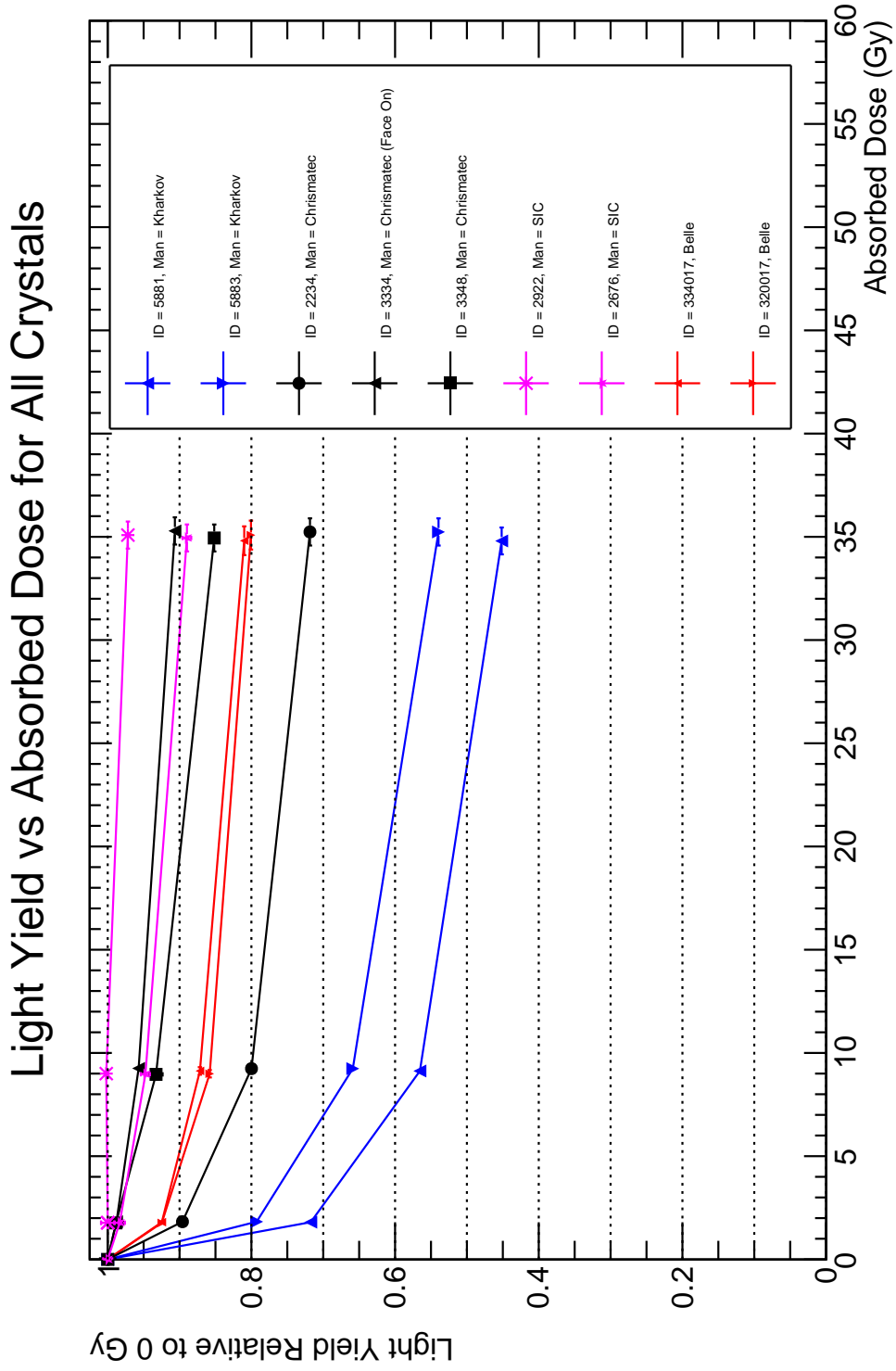


Figure 7.1: Light yields at each dosing stage for all CsI(Tl) crystals studied. Points are connected to help guide the eye.

Energy Resolution

The raw ^{207}Bi spectra measured with crystal 5881 at each dosing stage is shown in Figure 7.2. Crystal 5881 was observed to be the least radiation hard crystal and had the largest change in energy resolution. The resolution of the 1 MeV peak degraded from $4.84 \pm 0.02\%$ at 0 Gy to $9.81 \pm 0.07\%$ at 35 Gy. This degraded resolution is still superior to that measured for undosed pure CsI that was 18 %.

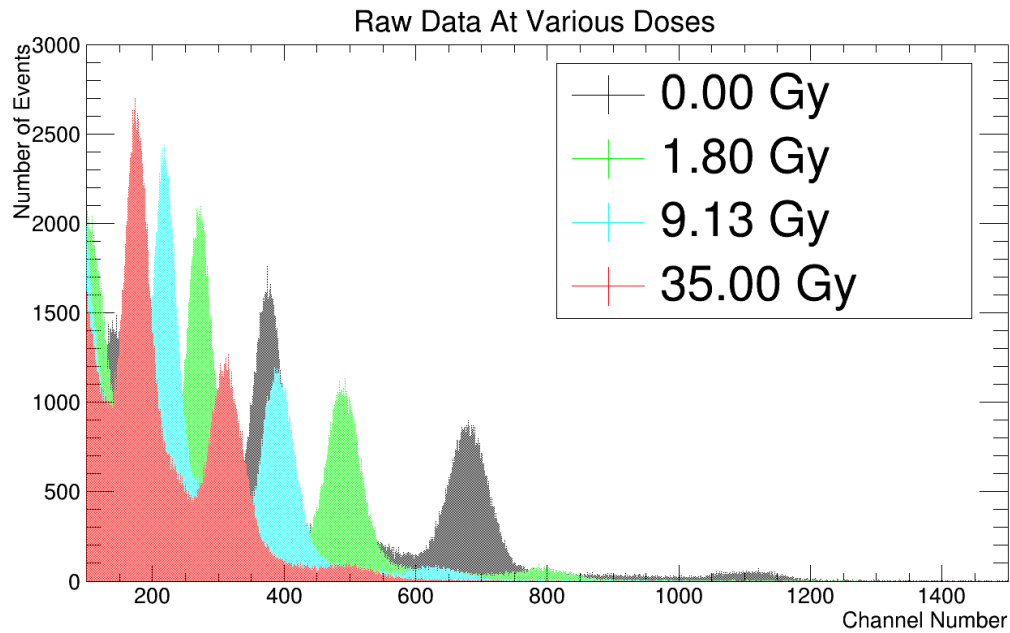


Figure 7.2: ^{207}Bi spectra measured with crystal 5881 at each dosing stage. Degradation in energy resolution is observed.

For the remaining *BABAR* crystals, R_E was also found to degrade as a function of absorbed dose. Figure 7.3 shows the energy resolution for all crystals as a function of dose. The majority of crystals were found to maintain an energy resolution better than 6 % after 35 Gy dose.

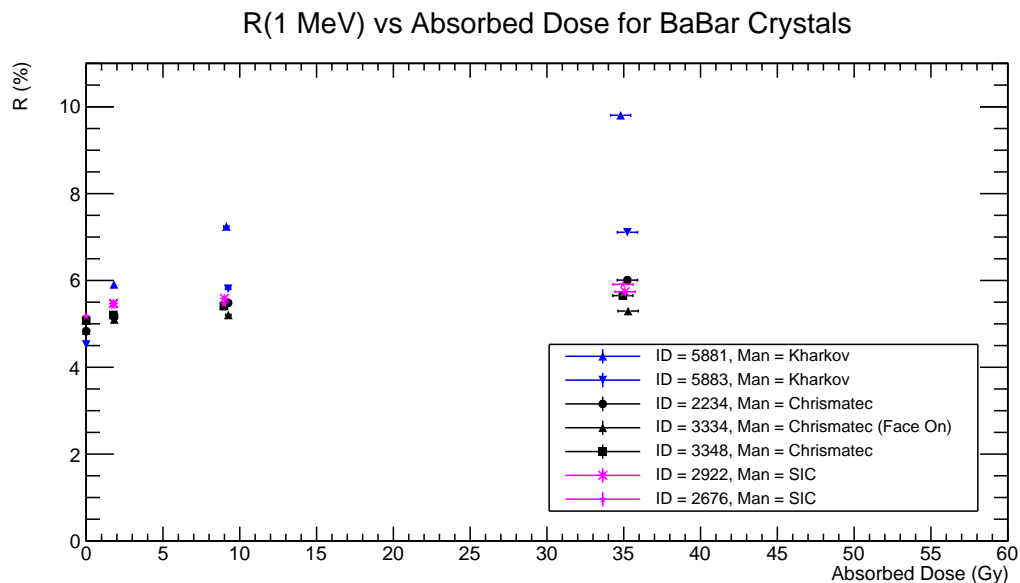


Figure 7.3: *BABAR* Crystal energy resolution degradation as function of dose.

The correlation between light yield and energy resolution is shown in Figure 7.4 for all *BABAR* crystals. As expected, a higher light yield results in a better energy resolution.

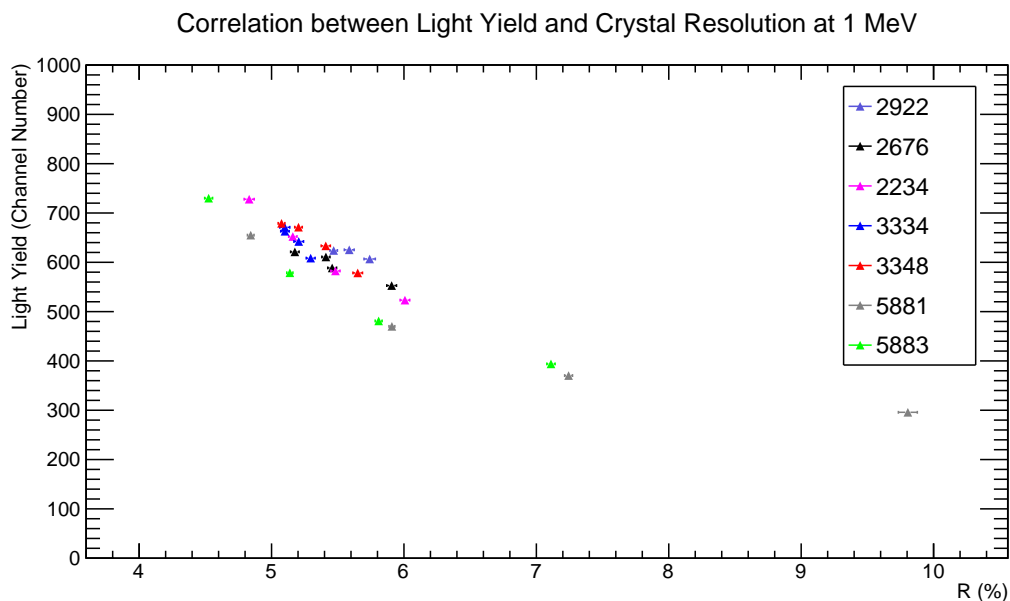


Figure 7.4: Correlation between *BABAR* Crystal resolution at 1 MeV and light yield.

Crystal Discolouration

Evidence for increased absorption of optical light was visually present in the *BABAR* crystals (the Belle crystals could not be directly observed as they were completely wrapped). Figure 7.5 shows photographs of several *BABAR* crystals at various dosing stages. All crystals began clear in color as shown in Figure 7.5a. After dosing, crystals with large light losses were observed to turn pink and less transparent. The discolouration is evidence that components of white light entering from the room are being absorbed in the crystal resulting in the light escaping to be pink.



(a) 2410 Reference (Undosed)



(b) 3334 (10 Gy, 95 % LY)



(c) 5883 (10 Gy, 66 % LY)



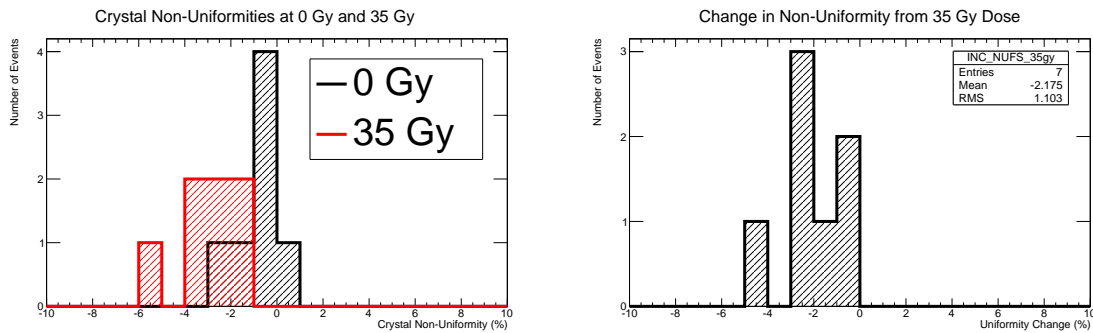
(d) 5881 (35 Gy, 45 % LY)

Figure 7.5: Pink discolouration observed in *BABAR* CsI(Tl) crystals.

Light Yield Non-uniformity Changes

Figure 7.8 on the following page, shows uniformity plots for several *BABAR* crystals at 0 Gy and 35 Gy. As the absorbed dose in the crystals increased, it was observed that the light yield degraded faster at the end farthest from the PMT compared to

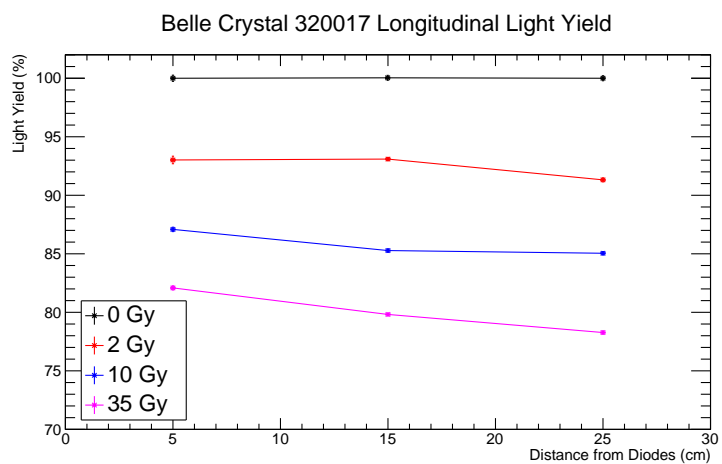
the near end for all crystals. The increases in crystal non-uniformity observed are summarized in Figures 7.6a and 7.6b showing the overall non-uniformity of all *BABAR* crystals at 0 Gy and at 35 Gy and the changes in non-uniformity from radiation damage, respectively.



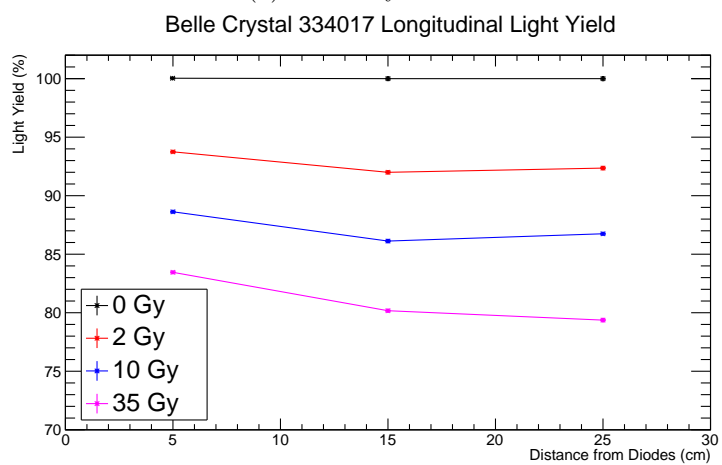
(a) Histogram overall uniformities of *BABAR* crystals at 0 and 35 Gy. (b) Histogram of change in uniformity from radiation damage at 35 Gy.

Figure 7.6: Summary of changes in non-uniformity for *BABAR* crystals.

The same trend was also observed in the Belle crystals and is shown in Figure 7.7 where the change in light yield for each trigger position plotted.



(a) Belle Crystal 320017



(b) Belle Crystal 334017

Figure 7.7: Change in Belle crystals light yield from radiation damage.

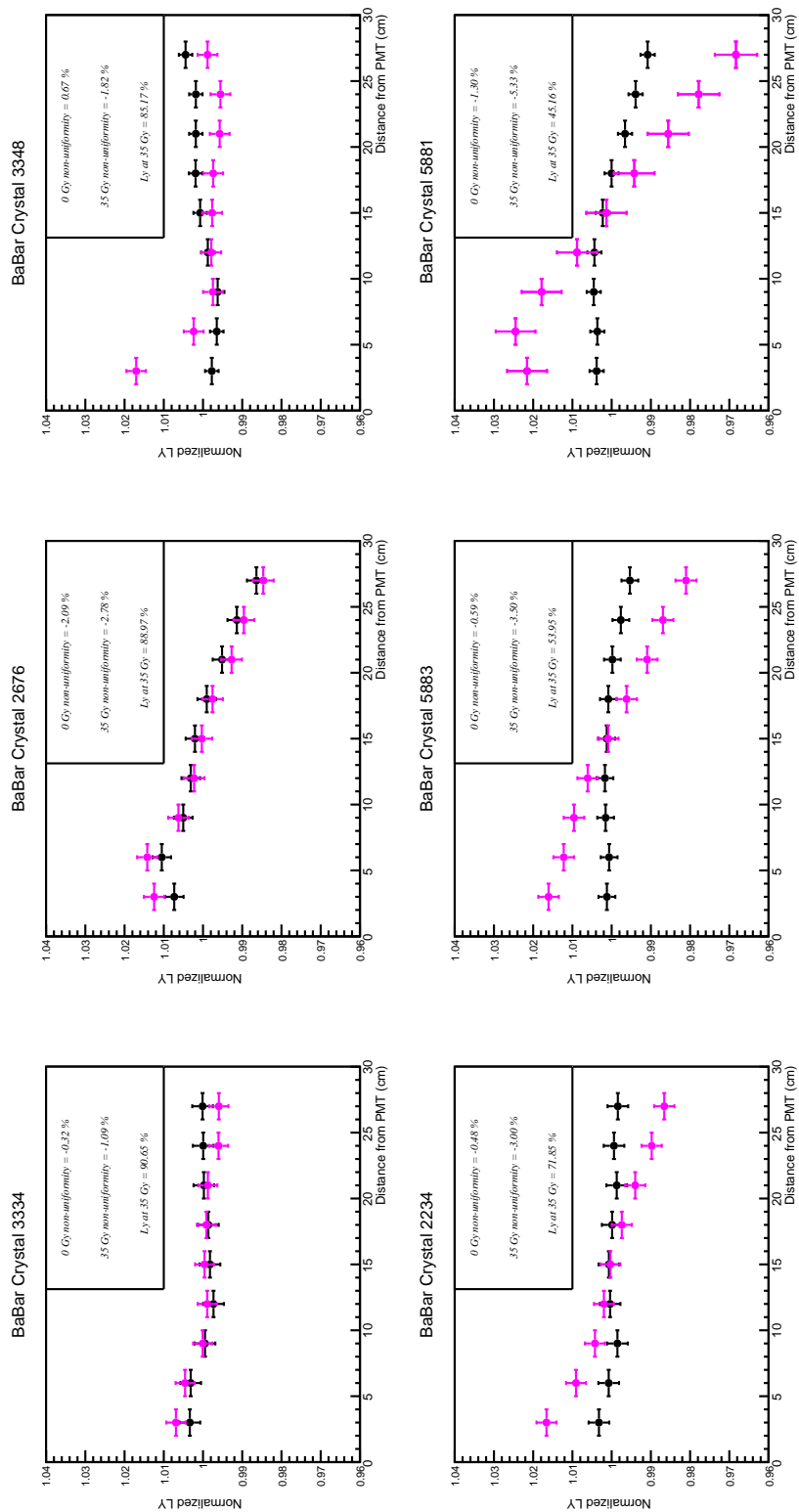


Figure 7.8: Uniformity plots for BABAR crystals at 0 Gy and 35 Gy.

The changes in non-uniformity observed can be compared to the results of the GEANT4 simulation described in Chapter 5 Section 5.1. Figure 7.9 shows the measured correlations between crystal light yield and non-uniformity for the *BABAR* crystals. Using the simulation described in Section 5.1 where the absorption length of the crystal was varied, the same correlation plot for three crystal geometries is shown in Figure 7.10. The three simulated crystals are each tapered and 30 cm long but differ in end face area size as shown in the legend. The dependence of the correlation between non-uniformity and light yield is observed in this plot and explains the variations in the measured non-uniformity vs light yield curves. This comparison also further evidence that the drop in light yield is a result of increased absorption in the crystal.

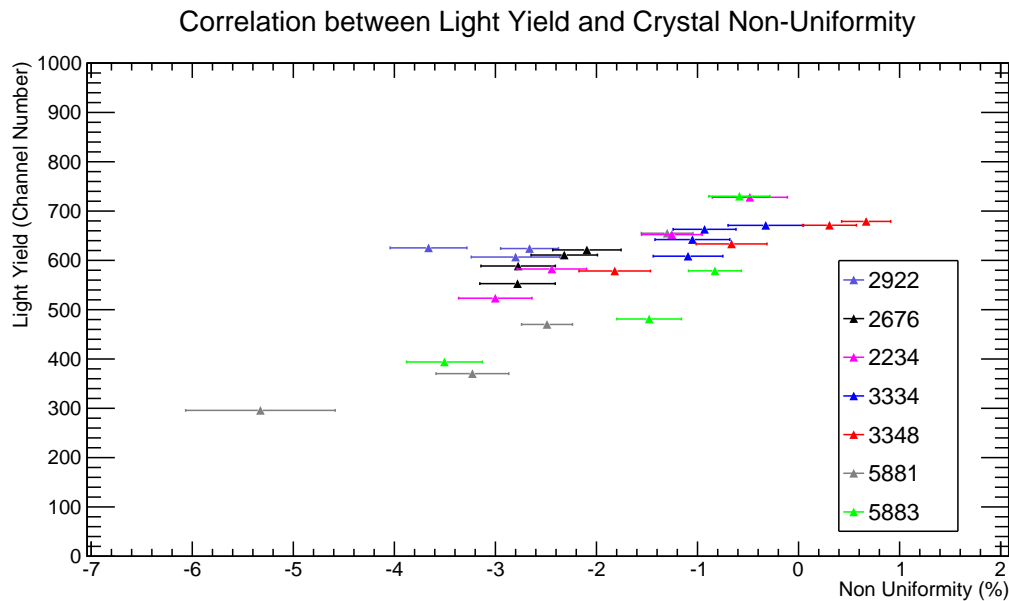


Figure 7.9: Correlation plot for *BABAR* crystals.

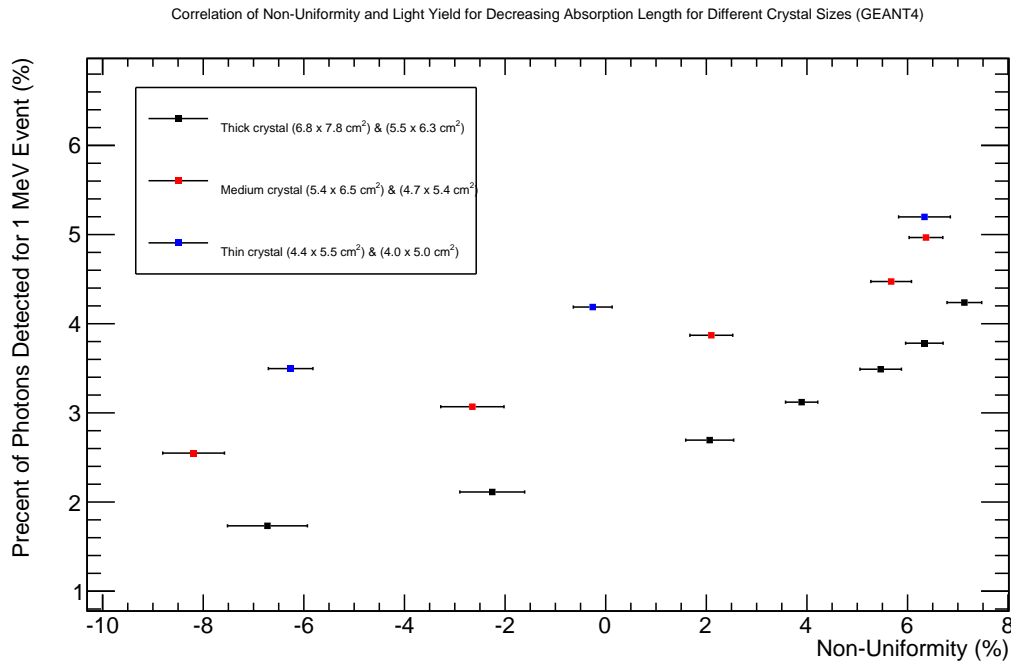


Figure 7.10: GEANT4 correlation plot for different crystal sizes.

After installation in the Belle II ECL, any changes to the overall light yield of the crystal can be corrected by recalibration. Changes to the non-uniformity however cannot be corrected and increase the constant term of the energy resolution of the ECL. As the constant term is energy independent, an increase in the constant term will degrade the resolution for all energies. The GEANT4 study presented in Chapter 5 examined the sensitivity of the energy resolution to change in crystal non-uniformity. It was found that below 15 % non-uniformity the energy resolution is not highly sensitive to small changes in non-uniformity. For large non-uniformities however, the resolution will rapidly degrade. After 35 Gy, all crystal non-uniformities remained less than 10 % and changes to non-uniformity were only about 2-4%. Thus the changes in non-uniformity are not large enough to significantly degrade the energy resolution of the ECL.

Scintillation Decay Time Changes

No changes in the scintillation decay times for the *BABAR* crystals was observed. A plot of the fast time constant for all *BABAR* crystals as a function of dose is shown in Figure 7.11. Table A.4 in the Appendix has the numerical values of each time constant for each dosing stage. Crystals BCAL5881 and BCAL5883, which were both from

the same manufacturer, had slightly longer fast time constants compare to the other *BABAR* crystals. These crystals also had very poor radiation hardness compared to the other crystals. This suggests that these two observations could be related and this measurement could potentially be used as a radiation hardness acceptance test for CsI(Tl) crystals.

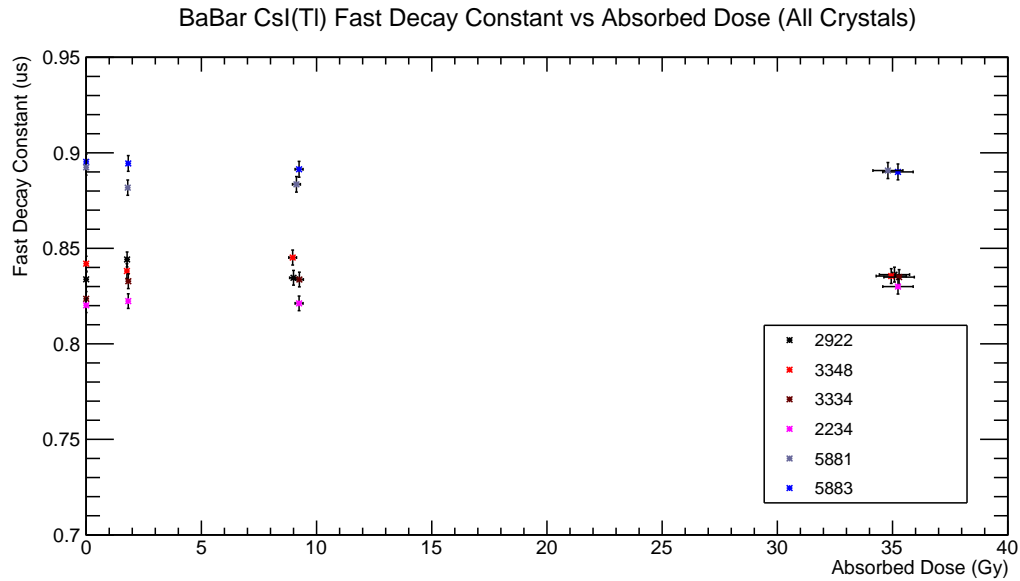


Figure 7.11: Fast time constants of *BABAR* CsI(Tl) crystals as function of dose.

Belle Time Resolution Changes

The time resolution for both Belle crystals as a function of absorbed dose is shown in Figure 7.12.

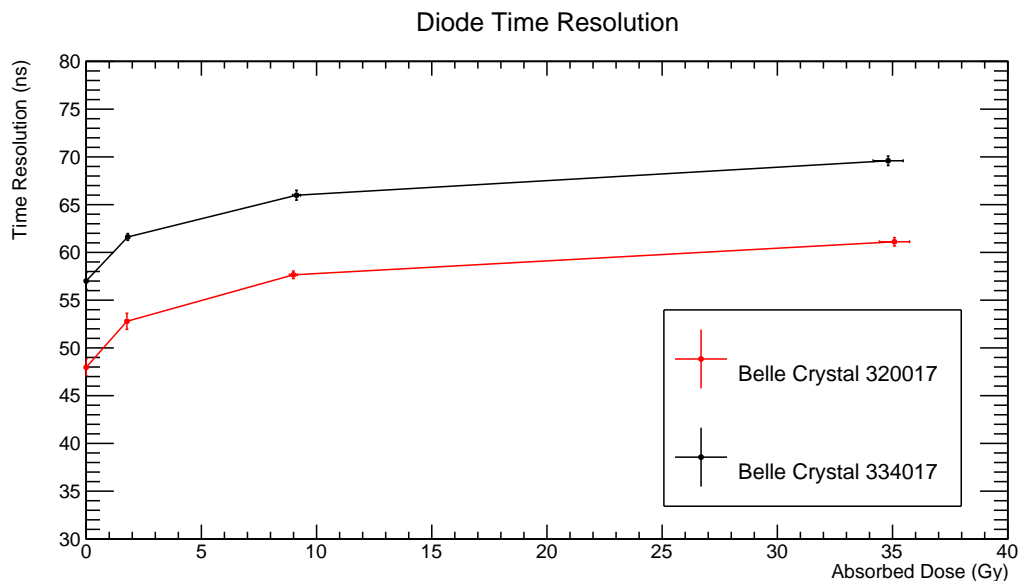


Figure 7.12: Time resolution of Belle crystals as function of radiation dose.

As the time resolution is a function of light yield, the degradation observed is a result of the light loss of the crystal. Using data recorded when performing time resolution measurements, the light yield of the individual diodes was measured as a function of the dose. The light yield of the individual diodes is observed to follow the same trend of the summed light yield analysis and is shown in Figure 7.13. The difference in light yield between crystal 320017 and 334017 also can account for the difference in the time resolutions observed for the Belle crystals.

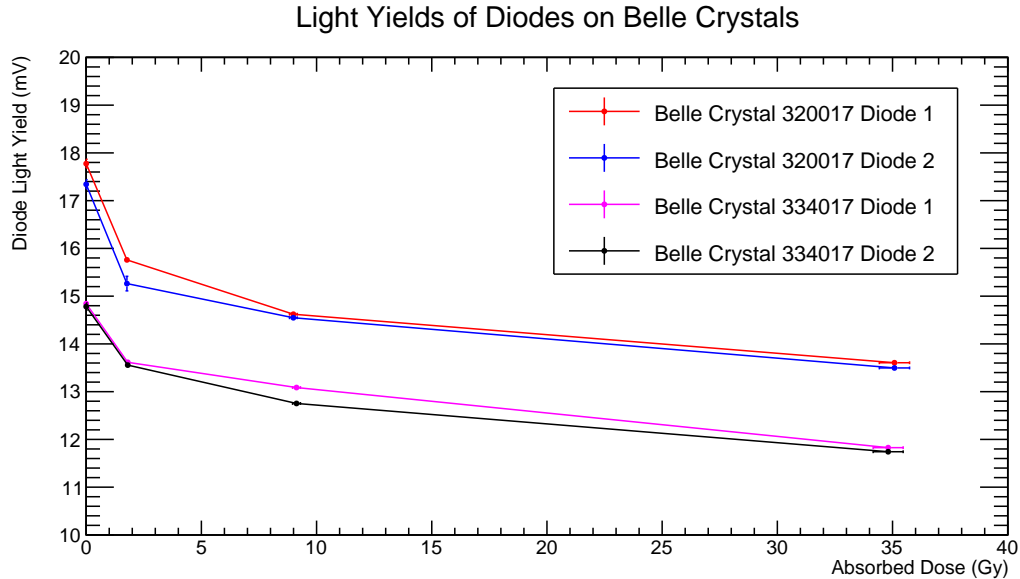


Figure 7.13: Light yield of diodes on Belle crystals as function of radiation dose.

7.2.1 Discussion of Mechanism for Radiation Damage in CsI(Tl) and Comparisons

As discussed in Chapter 3, previous studies of irradiated CsI(Tl) crystals have shown that radiation damage occurs through the creation of absorption centres. The crystals studied in this work were wrapped and thus transmission spectra of the crystals could not be measured. Strong evidence for increased self-absorption is observed with the crystal discolourations and changes in light yield non-uniformity. As the scintillation decay times of the *BABAR* CsI(Tl) crystals remained unchanged, this suggests that the scintillation mechanism was unaffected by the 1 MeV gamma doses.

The large variations in radiation hardness observed from different manufactures suggests that the radiation hardness of a crystal is dependent on the growth procedure. This has been proposed by previous CsI(Tl) radiation hardness studies where it was found that oxygen contamination during growth lead to poor radiation hardness [21].

Model to Describe Light Yield Plateau

The decrease in light yield as a function of radiation dose for all crystals was observed to follow a non-linear trend such that the light loss began to plateau at large dose. Derived in Appendix Section A.2.1, a model to describe the light loss of the crystals

was calculated. The model assumes that the light loss in the crystals is due to the creation of absorption centres that reduce the absorption length of scintillation light in the crystals. This assumption is well motivated by the experimental and simulated observations of this study. By assuming that each crystal has a maximum number of impurity locations where an absorption center can be made, it can be shown that the light loss in the the crystals as a function of dose, $LY_{\%}(D)$, will be given by equation 7.1.

$$LY_{\%}(D) = \exp \left(L \left[\frac{1}{A_0} - \frac{1}{A_0 - A_r^{\max} N_{\%}(D, D_i)} \right] \right) \quad (7.1)$$

where

L = Average path length of scintillation photon in crystal.

A_0 = Absorption length of scintillation photon at 0 Gy.

A_r^{\max} = Maximum decrease in absorption length when all impurity locations become absorption centres.

$N_{\%}(D, D_i) = 1 - e^{-D/D_i}$ = Percent of absorption centres created from total.

D_i = Radiation dose when $\frac{1}{e}$ of the impurity locations have been converted to absorption centres.

D = Radiation dose.

The two parameters that describe the radiation hardness of the crystals are A_r and D_i . As the concentration of impurities crystal-to-crystal will vary, A_r will also vary crystal-to-crystal. The parameter, D_i , should be the same for all crystals with the same impurity.

In order to fit this model to the experimental data the parameter L and A_0 were both assumed to be 30 cm and 35 cm, respectively. The parameters D_i and A_r^{\max} were fit to the data. For two crystals, 2676 and 3348 the model fit well as shown in Figures 7.14a and 7.14b.

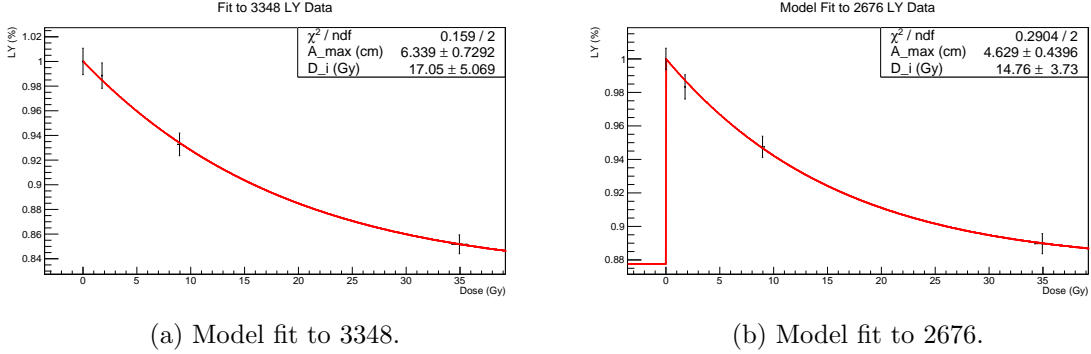
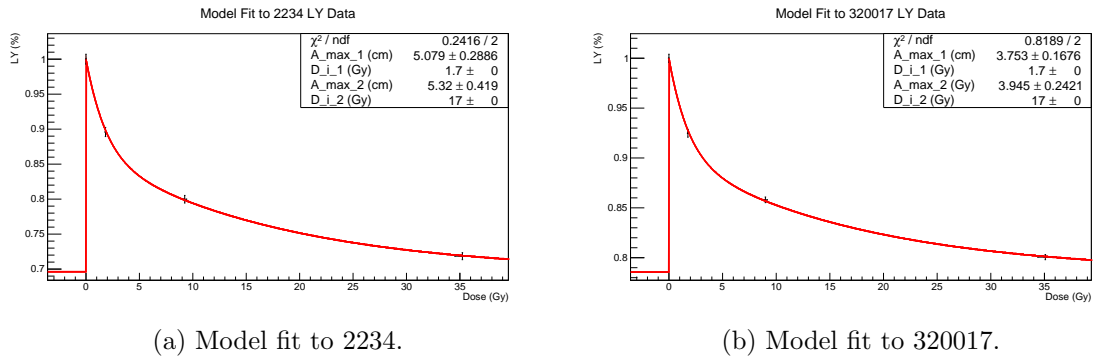


Figure 7.14: Sample model fits to data.

The D_i variable in both of these fits are consistent which is predicted if the absorption centres come from the same impurity. The A_r^{\max} parameters differ as expected since the concentration of impurities in each crystal will be different leading the difference in total light loss in both crystals.

For the remaining crystals it was found that the parameter $D_i = 17$ Gy could not account for the large initial drop in light yield from 0-2 Gy. From other studies of the absorption centers in CsI(Tl) multiple absorption components in the 550 nm region have been measured [20]. By adding another absorption center with $D_{i2} = 1.7$ Gy the remaining crystals could be fit using the equation 7.2. The absence of the $D_{i2} = 1.7$ Gy in some crystals can be explained by those crystals have a low concentration of the impurity or defect that causes this absorption centre. Some sample fits are shown in Figures 7.15a to 7.15b for crystals that required the 1.7 Gy component. Note in these fits the parameters D_{i1} and D_{i2} were fixed to 1.7 and 17 Gy.

$$LY_{\%}(D) = \exp \left(L \left[\frac{1}{A_0} - \frac{1}{A_0 - (A_{r1}^{\max} N_{\%}(D, D_{i1}) - A_{r2}^{\max} N_{\%}(D, D_{i2}))} \right] \right) \quad (7.2)$$



(a) Model fit to 2234.

(b) Model fit to 320017.

Figure 7.15: Sample modified model fits to data.

The model is shown to describe the plateauing trend of light loss with dose. By performing a chemical composition analysis of the crystals the model can be further tested to see if there is a correlation between a certain impurity and D_i and if that impurity concentration is related to A_r^{\max} .

Chapter 8

Conclusions

The primary objectives of this thesis were to measure the radiation hardness of large ($5 \times 5 \times 30 \text{ cm}^3$) CsI(Tl) scintillation crystals and to compare the scintillation properties of CsI(Tl) and pure CsI. In preparation for the backgrounds expected in the Belle II experiment, the results of this study will be used to help quantify whether an upgrade from CsI(Tl) to pure CsI is needed.

Apparatuses were designed and constructed to measure the scintillation properties of undosed CsI(Tl) and pure CsI crystals. The crystals were also compared in simulations using GEANT4. It was found that using the same light readout methods the energy resolution of CsI(Tl) is far superior to pure CsI. The energy resolution of the pure CsI with PMT readout, however surpassed that of CsI(Tl) with diode readout for 1 MeV photons. The scintillation decay times of the crystals were measured using cosmic ray muons and it was confirmed that the scintillation time for pure CsI is over an order of magnitude faster than CsI(Tl). This led to a far superior time resolution when compared to the current Belle CsI(Tl) crystals with diode readout.

The radiation hardness of CsI(Tl) was studied at doses of 2, 10 and 35 Gy where the light yield, energy resolution, non-uniformity, scintillation time and time resolution were measured. It was found that the light yield of the crystals decreased with increasing dose at different rates with the most radiation hard crystals maintaining over 90% of their original light yield after 35 Gy. Crystals from the same manufacturer were found to have similar radiation hardness properties allowing for the extrapolation of these results to other Belle II ECL crystals. The least radiation hard crystals were still found to have a higher energy resolution at 35 Gy for 1 MeV photons than an undosed pure CsI crystal. Evidence for increased absorption in the crystals was observed through visual discolouration and changes in the crystal

non-uniformity. Through simulations it was determined that the magnitude of the changes in non-uniformity from the 35 Gy dose will not significantly affect the overall energy resolution of the Belle II ECL. Although the scintillation decay time was unaffected by the radiation doses up to 35 Gy, the time resolution of the Belle crystals was degraded from the light loss, as expected.

Appendix A

Appendix

A.1 Cosmic Ray Apparatus Trigger Logic

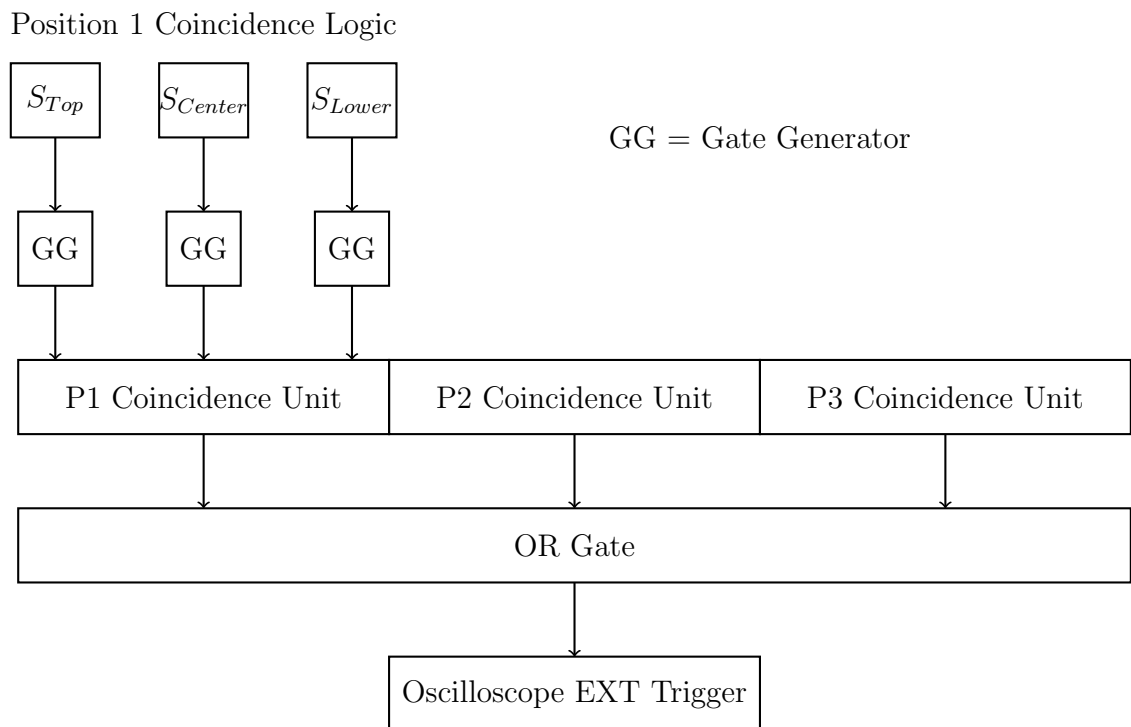


Figure A.1: Global Trigger logic for Cosmic Ray Apparatus.

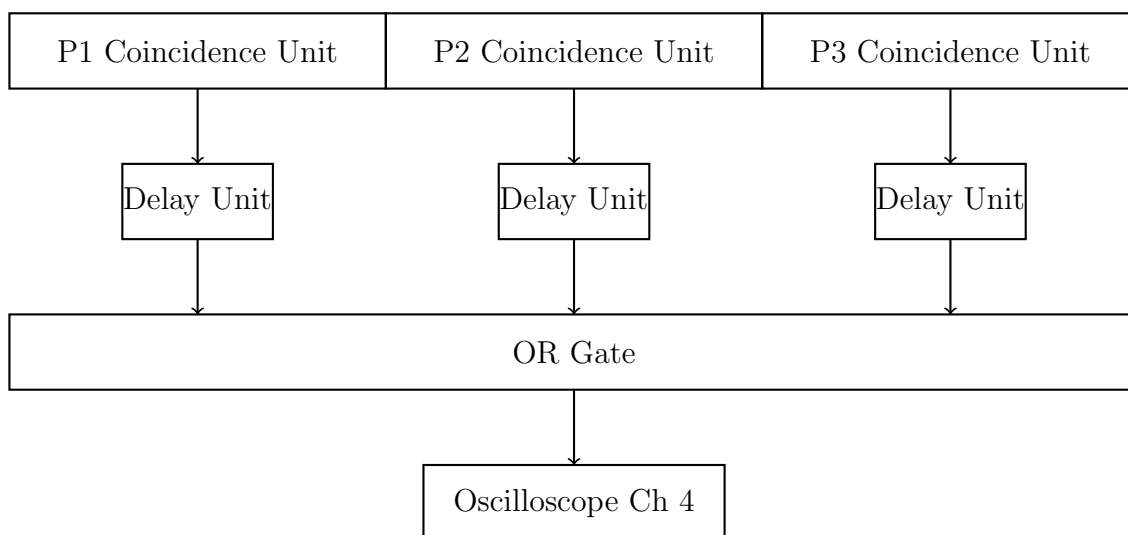


Figure A.2: Triggering delay logic to differentiate between position triggers.

A.2 Circuit Diagrams for Belle Crystal Readout

Schematics by Nicolas Braam, UVic Electronics Shop.

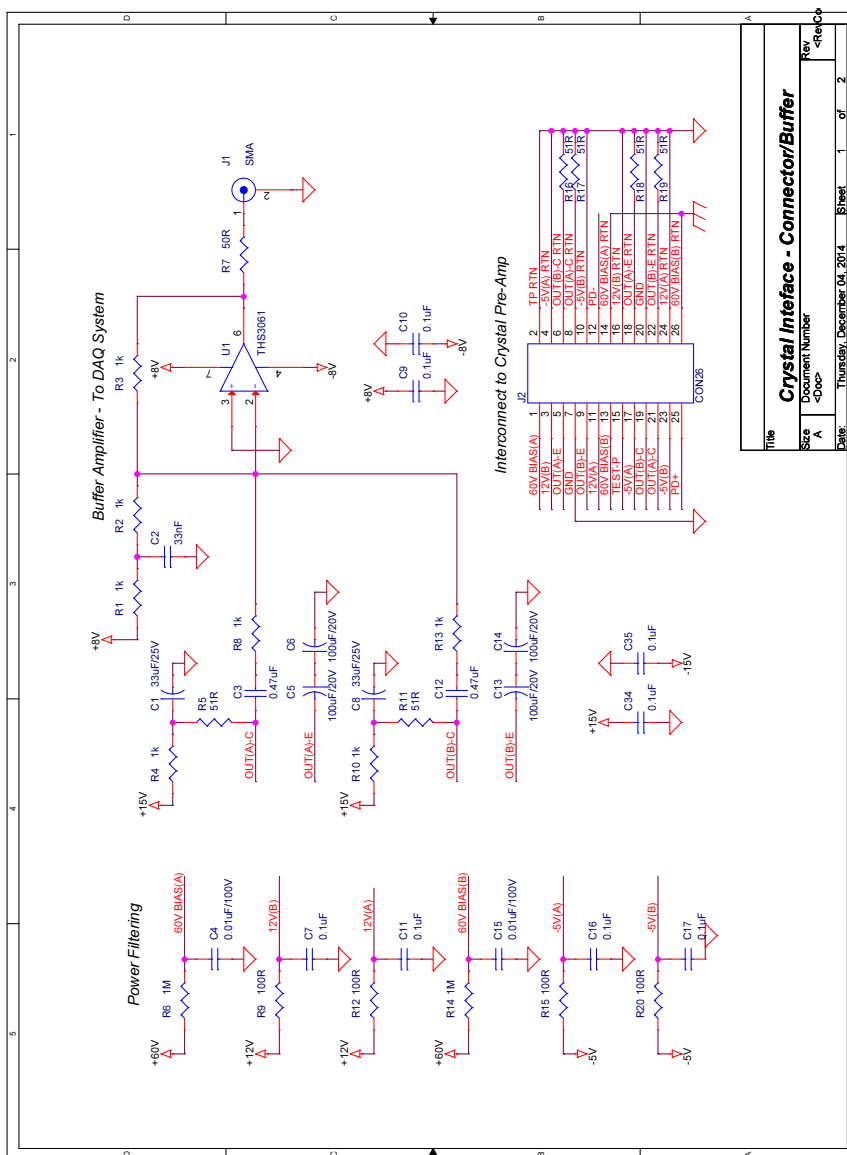


Figure A.3: UVic Readout Board Rev1 used for OUT-C and OUT-E comparison diagram 1/2.

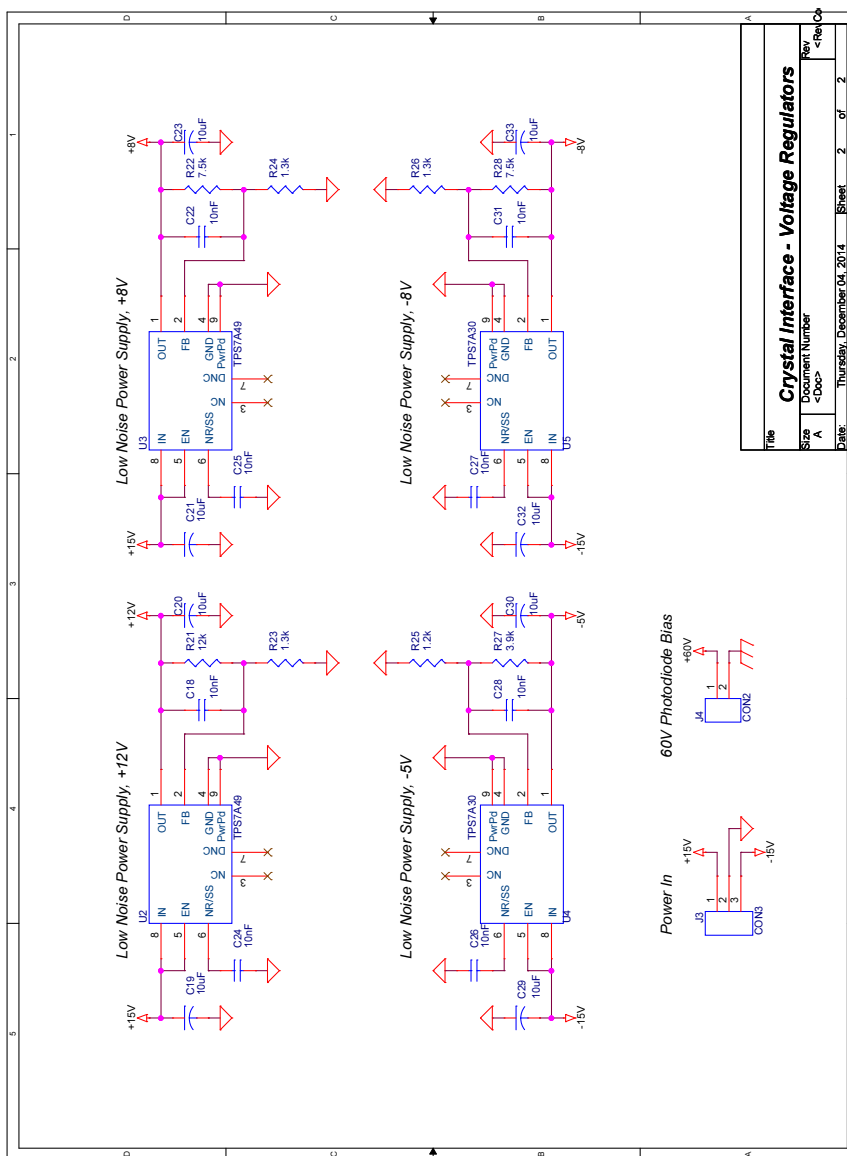


Figure A.4: UVic Readout Board Rev1 used for OUT-C and OUT-E comparison diagram 2/2.

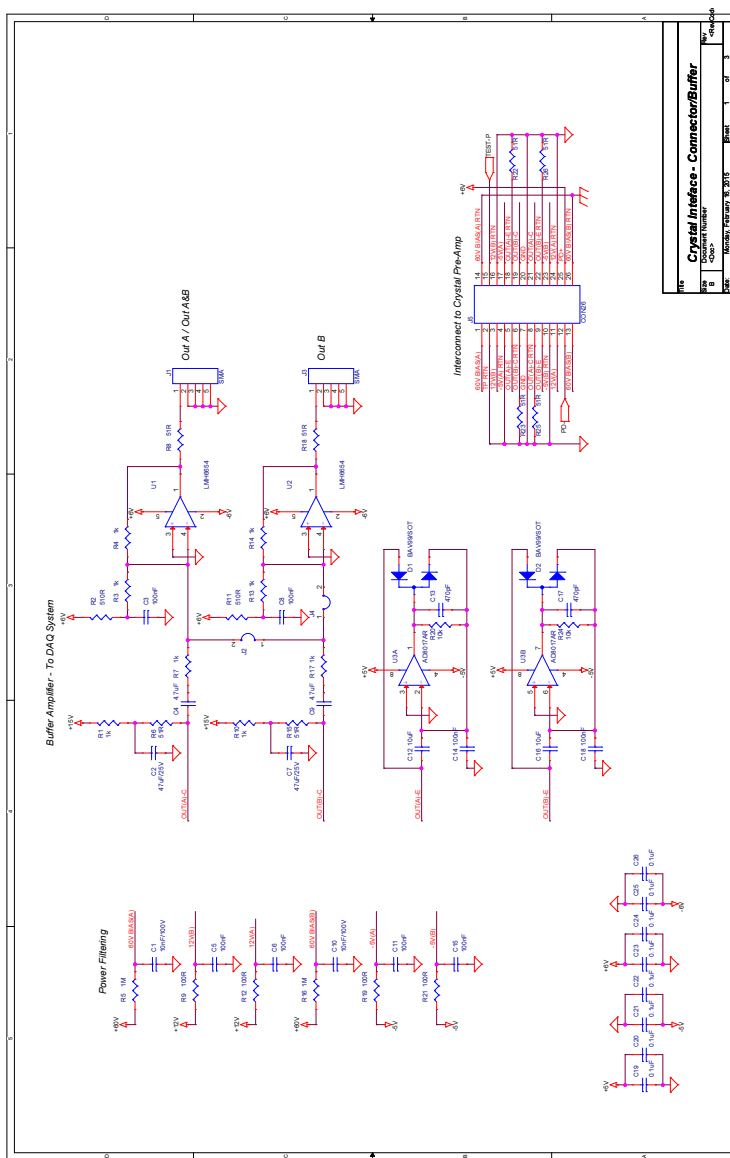


Figure A.5: UVic Readout Board Rev2 used Belle CsI(Tl) radiation hardness measurements diagram 1/3.

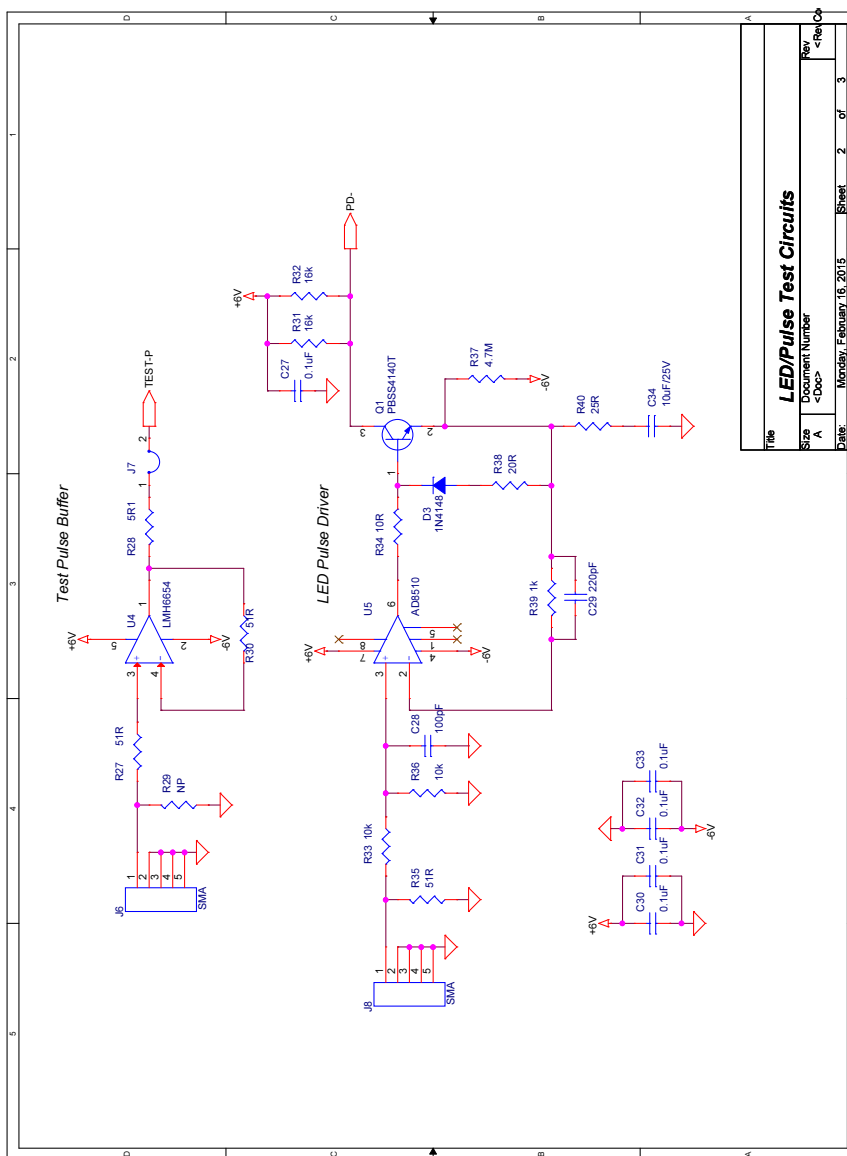


Figure A.6: UVic Readout Board Rev2 used Belle CsI(Tl) radiation hardness measurements diagram 2/3.

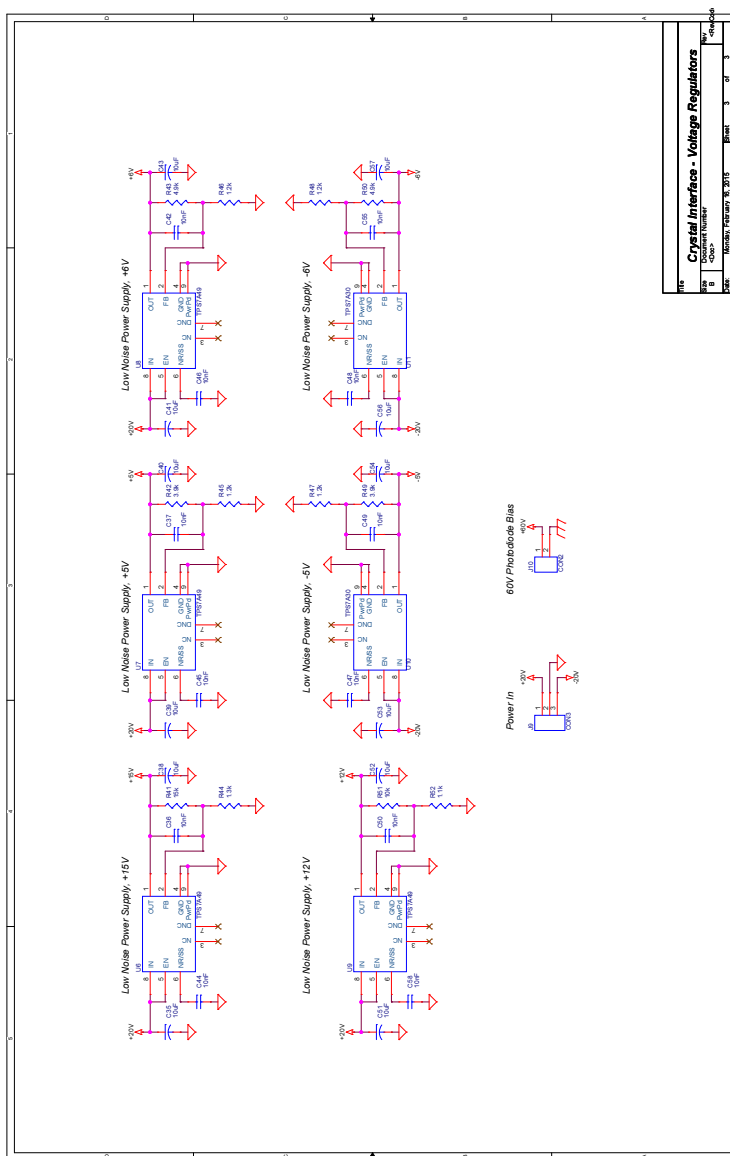


Figure A.7: UVic Readout Board Rev2 used Belle CsI(Tl) radiation hardness measurements diagram 3/3.

A.2.1 Derivation of Model to Describe Light Yield Plateau

The LY_{Det} at the detector is given by equation A.1.

$$LY_{\text{Det}} = LY_0 \times \mathcal{E}_f \times \mathcal{E}_T \quad (\text{A.1})$$

LY_0 = Scintillation Yield $\frac{\gamma}{\text{keV}}$

\mathcal{E}_f = Efficiency of crystal geometry to focus light.

\mathcal{E}_T = Transmission Efficiency

\mathcal{E}_T will decrease with absorbed radiation dose, D , thus the percent light yield at each dosing stage is given by equation A.2.

$$LY_{\%}(D) = \frac{\mathcal{E}_T(D)}{\mathcal{E}_T(0)} \quad (\text{A.2})$$

$\mathcal{E}_T(D)$ is given by the Beer-Lambert law used to describe the transmission of optical light in a material and is shown in equation A.3.

$$\mathcal{E}_T(D) = \exp\left(\frac{-L}{A_L}\right) \quad (\text{A.3})$$

L = path length of scintillation photon

$A_L = A_0 - A_r(D)$ = Absorption length (mean-free-path) of optical photon

For the radiation damaged crystals, the total absorption length, A_L , can be divided into two components. The first component, A_0 , gives absorption length in the the crystal at 0 Gy. The second component, $-A_r(D)$ represents the decrease in the absorption length due to radiation induced absorption centre formation.

$A_r(D)$ will be proportional to the number of absorption centres ($N_A(D)$) present in the crystal. Assuming that the absorption centres are the result of an impurity in the crystal, $A_r(D)$ will have a maximum value determined when all impurity locations have be turned into absorption centres. As there is a finite number of impurity locations, the rate of creation of absorption centres with dose will be given by equation A.4 where N_{max} is the maximum number of absorption centres in the crystal.

$$\frac{dN_A}{dD} = -\frac{(N_{\text{max}} - N_A(D))}{D_I} \quad (\text{A.4})$$

The parameter D_I has units of radiation dose and gives a scale for how much dose

is required to turn the impurity into an absorption centre. The solution to equation A.4 can be written as in equation A.5

$$N_{\%}(D) = \frac{N_A(D)}{N_{max}} = 1 - e^{-D/D_I} \quad (\text{A.5})$$

Using this solution, $A_r(D)$ can be parametrized as in equation A.6 where the parameter A_r^{\max} gives the maximum decrease in the absorption length due to absorption centre creation.

$$A_r(D) = A_r^{\max} \times N_{\%}(D) \quad (\text{A.6})$$

Putting this into equation A.2 and simplifying gives,

$$\text{LY}_{\%}(D) = \exp \left(L \left[\frac{1}{A_0} - \frac{1}{A_0 - A_r^{\max} N_{\%}(D, D_I)} \right] \right) \quad (\text{A.7})$$

A.3 Radiation Hardness Light Yield Results

Table A.1: Dose values and percent light yields (LY) for CsI(Tl) crystals at all dose stages.

Crystal ID	0 Gy		2 Gy		10 Gy		35 Gy	
	LY (%)	Dose (Gy) *	LY (%)	Dose (Gy)	LY (%)	Dose (Gy)	LY (%)	Dose (Gy)
320017	100.00 ± 0.40	1.77 ± 0.03	92.48 ± 0.39	8.99 ± 0.17	85.80 ± 0.28	35.08 ± 0.66	80.06 ± 0.26	
334017	100.00 ± 0.25	1.80 ± 0.03	92.47 ± 0.22	9.13 ± 0.17	87.16 ± 0.20	34.81 ± 0.65	81.00 ± 0.21	
2922*	–	1.78 ± 0.03	100.00 ± 0.93	9.00 ± 0.17	100.20 ± 0.85	35.08 ± 0.66	97.19 ± 0.75	
2676	100.00 ± 0.64	1.78 ± 0.03	98.33 ± 0.73	8.97 ± 0.17	94.75 ± 0.63	34.95 ± 0.65	88.97 ± 0.60	
3348	100.00 ± 1.07	1.77 ± 0.03	98.85 ± 1.03	8.96 ± 0.17	93.27 ± 0.92	34.94 ± 0.65	85.17 ± 0.76	
2234	100.00 ± 0.71	1.83 ± 0.03	89.60 ± 0.66	9.24 ± 0.17	79.99 ± 0.54	35.24 ± 0.66	71.85 ± 0.50	
3334**	100.00 ± 0.71	1.83 ± 0.03	98.78 ± 0.74	9.25 ± 0.17	95.70 ± 0.67	35.28 ± 0.66	90.65 ± 0.62	
5883	100.00 ± 0.57	1.83 ± 0.03	79.27 ± 0.49	9.24 ± 0.17	65.88 ± 0.39	35.24 ± 0.66	53.95 ± 0.35	
5881	100.00 ± 0.64	1.80 ± 0.03	71.74 ± 0.46	9.13 ± 0.17	56.54 ± 0.37	34.80 ± 0.65	45.16 ± 0.49	

*2922 results are normalized to 2 Gy LY due to change in crystal wrapping between 0 Gy and 2 Gy

**Crystal 3334 was dosed face-on giving a longitudinally non-uniform dose. The dose for crystal 3334 corresponds to the absorbed dose in the front 1/5 of the crystal.

A.4 Radiation Hardness Decay Time Results

Table A.2: Dose values and fitted scintillation times for CsI(Tl) crystals at all dose stages.

Crystal	Dose (Gy)	$\tau_{\text{fast}}(\mu\text{s})$	$\tau_{\text{slow}}(\mu\text{s})$
2922	0.000 \pm 0.000	0.834 \pm 0.004	5.10 \pm 0.03
	1.776 \pm 0.033	0.844 \pm 0.004	5.14 \pm 0.03
	8.999 \pm 0.168	0.835 \pm 0.004	5.11 \pm 0.03
	35.084 \pm 0.656	0.836 \pm 0.004	4.97 \pm 0.03
3348	0.000 \pm 0.000	0.842 \pm 0.004	5.10 \pm 0.03
	1.768 \pm 0.033	0.838 \pm 0.004	5.08 \pm 0.03
	8.962 \pm 0.168	0.845 \pm 0.004	5.15 \pm 0.03
	34.943 \pm 0.653	0.835 \pm 0.004	5.03 \pm 0.03
2234	0.000 \pm 0.000	0.820 \pm 0.004	5.11 \pm 0.03
	1.826 \pm 0.034	0.822 \pm 0.004	5.11 \pm 0.03
	9.241 \pm 0.173	0.821 \pm 0.004	5.08 \pm 0.03
	35.236 \pm 0.659	0.830 \pm 0.004	5.19 \pm 0.03
3334	0.000 \pm 0.000	0.824 \pm 0.004	5.12 \pm 0.03
	1.828 \pm 0.034	0.833 \pm 0.004	5.24 \pm 0.03
	9.253 \pm 0.173	0.834 \pm 0.004	5.16 \pm 0.03
	35.285 \pm 0.660	0.835 \pm 0.004	5.19 \pm 0.03
5881	0.000 \pm 0.000	0.892 \pm 0.004	5.05 \pm 0.03
	1.803 \pm 0.034	0.882 \pm 0.004	4.96 \pm 0.03
	9.126 \pm 0.171	0.884 \pm 0.004	4.98 \pm 0.03
	34.800 \pm 0.651	0.891 \pm 0.004	5.01 \pm 0.03
5883	0.000 \pm 0.000	0.895 \pm 0.004	5.14 \pm 0.03
	1.826 \pm 0.034	0.894 \pm 0.004	5.09 \pm 0.03
	9.240 \pm 0.173	0.891 \pm 0.004	4.98 \pm 0.03
	35.236 \pm 0.659	0.890 \pm 0.004	5.04 \pm 0.03

Bibliography

- [1] Christian Kiesling. CP Violation and the Future of Flavor Physics. *AIP Conf. Proc.*, 1182:317–326, 2009.
- [2] T. Abe, I. Adachi, K. Adamczyk, S. Ahn, H. Aihara, K. Akai, M. Aloï, L. Andricek, K. Aoki, Y. Arai, and et al. Belle II Technical Design Report. *ArXiv 1011.0352*, November 2010.
- [3] S. Agostinelli et al. GEANT4: A Simulation toolkit. *Nucl. Instrum. Meth.*, A506:250–303, 2003.
- [4] K.A. Olive et al. (Particle Data Group), *Chin. Phys. C*, 38, 090001 (2014).
- [5] D. Griffiths. *Introduction to Elementary Particles*. Wiley, 2008.
- [6] D. Green. *The Physics of Particle Detectors*. Cambridge Monographs on Particle Physics, Nuclear Physics and Cosmology. Cambridge University Press, 2000.
- [7] Claus Grupen. *Particle Detectors*. Cambridge University Press, 1996.
- [8] H. Nakano et al. Beam Background Simulation for SuperKEKB / Belle-II. In *Proceedings of IPAC2012*.
- [9] A. Beaulieu and S. de Jong. 12th background campaign: Ecl for 21st b2gm, ecl parallel. June 2015.
- [10] Saint Gobain. CsI(Tl), CsI(Na) Cesium Iodide Scintillation Material, 2014. Datasheet.
- [11] Saint Gobain. CsI(pure) Cesium Iodide Scintillation Material, 2014. Datasheet.
- [12] G.F. Knoll. *Radiation Detection and Measurement*. Wiley, 2000.

- [13] R.M. Brown and D.J.A. Cockerill. Electromagnetic calorimetry. *Nuclear Instruments and Methods in Physics Research Section A: Accelerators, Spectrometers, Detectors and Associated Equipment*, 666(0):47 – 79, 2012.
- [14] J.B. Birks. *The Theory and Practice of Scintillation Counting*. International Series of Monographs on Electronics and Instrumentation. Pergamon Press, 1964.
- [15] P. Schotanus, R. Kamermans, and P. Dorenbos. Scintillation characteristics of pure and Tl doped CsI crystals. *IEEE Trans. Nucl. Sci.*, 37:177–182, 1990.
- [16] Masaaki Kobayashi, Masaharu Ieiri, Kenjiro Kondo, Taichi Miura, Hiroyuki Noumi, Masaharu Numajiri, Yuichi Oki, Takenori Suzuki, Minoru Takasaki, Kazuhiro Tanaka, Yutaka Yamanoi, Shojiro Sugimoto, and Mitsuru Ishii. Radiation hardness of undoped CsI crystals against high energy protons. *Nuclear Instruments and Methods in Physics Research Section A: Accelerators, Spectrometers, Detectors and Associated Equipment*, 328(3):501 – 505, 1993.
- [17] D.M. Beylin, A.I. Korchagin, A.S. Kuzmin, L.M. Kurdadze, S.B. Oreshkin, S.E. Petrov, and B.A. Shwartz. Study of the radiation hardness of CsI(Tl) scintillation crystals. *Nuclear Instruments and Methods in Physics Research Section A: Accelerators, Spectrometers, Detectors and Associated Equipment*, 541(3):501 – 515, 2005.
- [18] M.M. Hamadaa. Dependence of scintillation characteristics in the CsI(Tl) crystal on tl* concentrations under electron and alpha particles excitations. In *Nuclear Science Symposium Conference Record, 2000 IEEE (Volume:1)*, volume 1, pages 6/164 – 6/169. IEEE, Oct 2000.
- [19] Boxiang Yu, Cheng Yuan, Janguang Lu, Li Zhou, Gang Qin, et al. The radiation hardness test on CsI(Tl) crystals for BESIII. *Nuclear Science Symposium Conference Record (NSS/MIC), 2009 IEEE*, pages 2032–2035, 2009.
- [20] M.A.H. Chowdhury, S.J. Watts, D.C. Imrie, A.K. McKemey, and A.G. Holmes-Siedle. Studies of radiation tolerance and optical absorption bands of CsI(Tl) crystals. *Nuclear Instruments and Methods in Physics Research Section A: Accelerators, Spectrometers, Detectors and Associated Equipment*, 432(1):147 – 156, 1999.

- [21] Ren-Yuan Zhu. Radiation damage in scintillating crystals. *Nuclear Instruments and Methods in Physics Research Section A: Accelerators, Spectrometers, Detectors and Associated Equipment*, A413(23):297 – 311, Feb 1998.
- [22] M.A.H Chowdhury, A Holmes-Siedle, A.K McKemey, S.J Watts, and D.C Imrie. Radiation effects in CsI(Tl) crystals from a controlled growth process. *Nuclear Instruments and Methods in Physics Research Section A: Accelerators, Spectrometers, Detectors and Associated Equipment*, 413(23):471 – 474, 1998.
- [23] J.H. Schulman and W.D. Compton. *Color Centers in Solids*. International series of monographs on solid state physics. Macmillan, 1962.
- [24] Margarida M Hamada, Fabio E Costa, Shigenori Shimizu, and Shinzou Kubota. Radiation damage of CsI(Tl) scintillators: blocking of energy transfer process of vk centers to tl+ activators. *Nuclear Instruments and Methods in Physics Research Section A: Accelerators, Spectrometers, Detectors and Associated Equipment*, 486(12):330 – 335, 2002. Proceedings of the 6th International Conference on Inorganic Scintillators and their Use in Scientific and Industrial Applications.
- [25] Stanford Scintillator Material Group. Research Fundamentals. <http://web.stanford.edu/group/scintillators/scintillators.html>, Accessed on July 12, 2015.
- [26] HAMAMATSU. Photomultiplier tubes, 2003. catalog.
- [27] D. E. Alburger and A. W. Sunyar. Decay of Bi²⁰⁷. *Phys. Rev.*, 99:695–702, Aug 1955.
- [28] Alex Kuzmin. Private communication. January 2015.
- [29] Ernesto Mainegra-Hing. Dosimetry and irradiation uniformity of CsI crystals irradiated with a 60 Co beam. a monte carlo study. Report IRS-2098 DRAFT.
- [30] Ernesto Mainegra-Hing. Private communication. July 2015.
- [31] CMS ECAL Technical Design Report, CERN/LHCC 97-33, 1997.
- [32] Douglas Jonathon Graham and Christopher Seez. Simulation of Longitudinal Light Collection Uniformity in PbWO4 crystals. 1996. CMS-NOTE-1996-002, CERN-CMS-NOTE-1996-002.

- [33] C. L. Woody, J. A. Kierstead, P. W. Levy, and S. Stoll. Radiation damage in undoped CsI and CsI(Tl). *IEEE Trans. Nucl. Sci.*, 39:524–531, 1992.
- [34] M. Kobayashi et al. Radiation hardness of undoped CsI crystals against high-energy protons. In *International Workshop on Heavy Scintillators for Scientific and Industrial Applications: Crystal 2000 Chamonix, France, September 22-26, 1992*, 1992.
- [35] W.R. Leo. *Techniques for Nuclear and Particle Physics Experiments: A How-To Approach*. U.S. Government Printing Office, 1994.